UNIVERSITÉ DU QUÉBEC

THÈSE PRÉSENTÉE À
L'UNIVERSITÉ DU QUÉBEC À CHICOUTIMI
COMME EXIGENCE PARTIELLE
DU DOCTORAT EN INGÉNIERIE

PAR
TAMÁS KÁLMÁN

DYNAMIC BEHAVIOR OF ICED CABLES SUBJECTED TO MECHANICAL SHOCKS

COMPORTEMENT DYNAMIQUE DES CÂBLES RECOUVERTS DE GLACE ET SOUMIS À DES CHOCS MÉCANIQUES

MARS 2007

"Everything is possible to man. Time is young; give us some little centuries, and we shall control and remake all things."

Will Durant
Philosophy of Francis Bacon
The Story of Philosophy, 1926

RÉSUMÉ

Dans les régions froides, les conducteurs de lignes et leurs supports sont directement exposés au givrage atmosphérique. En outre, on s'attend à ce que les températures croissantes dues aux changements climatiques augmentent les risques liés aux événements météorologiques extrêmes qui peuvent augmenter la fréquence et la sévérité des tempêtes de verglas.

Plusieurs types de dépôt de glace atmosphérique peuvent charger les câbles aériens : la neige collante, le givre dur, le givre léger et le verglas. Les dépôts de glace sur des structures exposées peuvent être la source de plusieurs problèmes mécaniques. Sur les lignes aériennes à haute tension en particulier, les surcharges verticales dues à l'accumulation de glace lourde, couplées aux surcharges horizontales dues au vent sur les conducteurs et les structures glacés peuvent causer des dommages structuraux, conduisant même à l'effondrement des supports en cascade. Par conséquent, afin de protéger les lignes contre de telles surcharges et d'assurer la fiabilité des réseaux aériens de distribution et de transport d'électricité, diverses méthodes de déglaçage des lignes ont été employées. Une technique de dégivrage d'intérêt dans cette recherche emploie des chocs mécaniques pour dégivrer les câbles de garde profitant du comportement fragile de la glace dans un régime à taux de déformation élevé.

Cette recherche se concentre donc sur l'analyse dynamique des lignes aériennes de transport d'électricité recouvertes de glace et assujetties à des chocs mécaniques qui peuvent résulter de l'effet d'une charge externe prévue pour déglacer les conducteurs ou des déséquilibres de charge dus au délestage de glace soudain. En particulier, la réponse dynamique des câbles recouverts de glace soumis à des chocs mécaniques est étudiée par modélisation numérique utilisant la méthode des éléments finis non-linéaires. L'objectif est de comprendre le phénomène du délestage de glace induit mécaniquement sur des portées individuelles du câble aérien. Dans la plupart des études de délestage de glace précédentes, la réponse de la ligne au déchargement instantané a été modélisée, tandis que dans cette recherche, la propagation du délestage le long de la portée est étudiée.

L'auteur propose un modèle numérique qui considère la rupture du dépôt de glace explicitement en tenant compte des propriétés mécaniques de la glace. Ce modèle permet de calculer les effets dynamiques du délestage de glace induit par une excitation d'impulsion sur une section de ligne aérienne de portée simple qui simule l'effet d'une charge externe. Le modèle proposé peut servir de base pour étudier divers critères de rupture du dépôt de verglas en termes des relations de contraintes-déformations en tension et en flexion et tenant compte des effets du taux de déformation, en particulier. Diverses géométries de la section de ligne peuvent également être étudiées avec ce modèle. Plusieurs scénarios de délestage de glace pour des lignes à l'échelle réelle sont simulés afin d'étudier l'effet de variables comme l'épaisseur de glace, les paramètres de ligne tels que la longueur de portée, la tension du câble et sa rigidité axiale, et les caractéristiques d'impulsion.

Un modèle expérimental de portée simple à l'échelle réduite est également étudié afin de valider le modèle numérique.

ABSTRACT

In cold regions, overhead line cables and their supporting structures are usually fully exposed to atmospheric icing. In addition, rising temperatures due to climate changes are expected to increase the risks associated with extreme weather events which in turn could possibly increase the frequency and severity of storms such as winter blizzards and ice storms.

Several types of atmospheric icing deposits may load overhead cables including heavy adherent wet snow, hard rime, large but lightweight rime ice, and dense glaze ice. Ice deposits on exposed structures can be the source of several mechanical problems. On overhead power lines in particular, the gravity loads due to heavy ice accretion, coupled with wind-on-ice loads, may lead to structural damages, or failure and even cascading collapse of towers. Therefore, in order to protect the line against loads resulting as a consequence of accreted ice on the line and to ensure the reliability of electrical power delivery networks, various mitigation methods have been used. A de-icing technique of interest, in this study, uses mechanical shocks to de-ice ground wires by taking advantage of the brittle behavior of ice at high strain rates.

This study therefore focuses on the dynamic analysis of iced overhead transmission lines subjected to in-span shock loads. Such in-span loads may result from the effect of an external shock load intended to remove accreted ice from the cable or from load imbalances due to sudden ice shedding. In particular, the dynamic response of iced cables under shock loads is studied by numerical modeling using nonlinear finite element analysis. The objective is to understand the phenomenon of mechanically-induced ice shedding on overhead cable spans. In most previous studies of ice shedding on lines, the response of the line to instantaneous shedding was modeled, whereas in this research, the propagation of ice shedding along the span is studied.

A numerical model that explicitly considers the rupture of the ice deposit by including the mechanical properties of ice into the model is proposed. This model calculates the dynamic effects of ice shedding induced by a pulse-type excitation on a single-span overhead line section which simulates the effect of an external load to remove the accreted ice from the cable. The model can serve as a basis to study various failure criteria of atmospheric glaze ice in terms of axial and bending stress-strain relations and strain-rate effects, in particular. Various line section geometries can also be readily investigated using the model. Several ice-shedding scenarios of real-scale lines are simulated in order to investigate how variables including ice thickness, line parameters such as span length, cable tension and axial rigidity, and pulse-load characteristics affect the dynamic responses of iced cables subjected to mechanical shocks.

A level single-span reduced-scale experimental model is also studied in order to validate the numerical model.

ACKNOWLEDGMENTS

TABLE OF CONTENTS

LIST OF FIGURES

LIST OF TABLES

GLOSSARY OF NOTATIONS

A cross-sectional area (m^2)

c_L speed of a longitudinal (axial) wave (m/s)

c_T speed of a transverse wave (m/s)

C viscous damping constant (Ns/m)

d cable sag at the mid span (m)

d_c cable diameter (m)

E elastic modulus (Pa)

g acceleration of gravity (m/s^2)

H horizontal component of the cable tension (N)

I_t second moment of inertia (m^4)

l length of the span (m)

L unstressed length of the cable (m)

L_e effective cable length (m)

m mass per unit length (kg/m)

P instantaneous power conveyed by the wave (W)

R wave reflection coefficient

t time (s)

t_{ice} radial ice thickness (m)

T cable tension (N)

T_D natural period of the fundamental free vibration (s)

T_H horizontal component of the cable end-tension (N)

T_R resultant cable end-tension (N)

T_V	vertical component of the cable end-tension (N)
v	transverse velocity of the cable (m/s)
Z_L	impedance of the string to the longitudinal wave (kg/s)
Z_S	support impedance (kg/s)
Z_T	impedance of the string to the transverse wave (kg/s)
r, s, t	element local coordinate axes
X, Y, Z	global coordinate axes
DSD	droplet size distribution
MVD	median volume diameter
LWC	liquid water content of the air
α	Newmark integration operator parameter
δ	Newmark integration operator parameter
$\varepsilon_{initial}$	cable initial strain
ω_n	natural frequency (rad/s)
ω_L	natural frequency of the longitudinal wave (rad/s)
ω_T	natural frequency of the transverse wave (rad/s)
ρ	density (kg/m^3)

CHAPTER 1

INTRODUCTION

1.1 General

The scientific evidence is increasingly clear that the Earth's atmosphere is undergoing major changes. These changes raise two fundamental concerns regarding the gradual depletion of the protective ozone layer in the upper atmosphere and warming of the Earth's surface and lower atmosphere. Both of them are believed to lead to climate changes through complex processes and interactions [28, 29] that we are currently experiencing worldwide.

Rising temperatures are expected, among many things, to increase the risks associated with extreme weather events. Because such events often exceed the tolerance of our social and ecological system and are difficult to predict in advance, they can bring with them hardship, economic loss, severe social and ecological disruption, and even loss of life. From our perspective as engineers who study the effects of atmospheric icing on power lines, it is interesting to note that the impact of climate change and accompanying variations in weather patterns on the frequency and severity of storms such as winter blizzards and ice storms is still a topic requiring additional research. However, there are indications that the maximum potential intensity of such storms is likely to increase as the

surface temperatures of the Earth increase [28]. In a warming climate, milder winter temperatures could possibly cause an increase in freezing rain. Freezing rain is a common experience in most part of Canada [22]. However, the 1998 Ice Storm that struck much of eastern Canada and North Eastern United States was remarkable for its persistence, its extent and the magnitude of its destruction [22, 45]. It knocked down power lines leaving millions of people without electricity for days, and in some areas, for weeks [21, 45 and 51]. In cold regions, especially in Québec which relies heavily on electric power, electric outages lasting even a few days in harsh cold conditions have serious public safety and economical consequences (e.g. lack of heating, water supply, and paralysis of several industrial and public service activities).

1.2 Problem definition

In most countries relying on hydroelectricity, electricity power stations are often located far from consumer areas. Therefore, the reliability of the transmission and distribution of electricity depends on a well-established transmission grid.

Power transmission lines comprise four major components that are interconnected: towers, foundations, cables, and interfaces such as insulators and other items of line hardware. Two types of cables are generally present: the conductors and the overhead ground wires (OHGWs) which protect the line against lightning. Ground wires equipped with fiber optics may also serve as telecommunication lines, in which case they are called optical overhead ground wires (OPGWs). To attenuate the effects of corona discharges, multiple conductors are used in bundles at high line voltages.

A transmission line is composed of several line sections, which are defined as series of spans bounded by two straining structures with anchored insulator strings. As a result, each line section is considered structurally independent of adjacent sections. Most often, the use of straining structures is governed by the characteristics of the terrain or land usage, i.e. a change in the line direction is needed when the geographic profile is mountainous or when an obstacle needs to be crossed.

The main loads applied to transmission line structures come from the cables they support. The most frequent external loads to which a line section is subjected during its service life are wind, and in cold regions prone to atmospheric icing, ice loads. It is well known that ice deposits on cables, coupled with wind-on-ice load, can be the source of several mechanical problems [8].

From mechanical engineering aspects, loads acting on power lines can be considered as static, quasi-static, cyclic and dynamic. Static loads are derived mainly from the structure itself (dead loads) while the quasi-static classification comprises mainly the effects of steady wind, ice accumulation and maintenance. Several cyclic effects derive mainly from wind-induced vibrations (galloping and wake-induced vibration), while natural ice and snow shedding, and forces due to flashovers or mechanical de-icing processes, must be treated as transient dynamic loads. Exceptional events, such as conductor breakage or drop of conductor suspension assembly may also cause severe dynamic loads [36, 42, 49 and 52].

In order to avoid catastrophic events like the 1998 Ice Storm in Eastern North America and to reduce the impact of ice deposits on power lines, de-icing and anti-icing methods for overhead lines have been developed and studied worldwide. Several of these methods aimed at de-icing overhead lines have been developed and applied by Hydro-Québec [41, 43, 44 and 64]. A de-icing technique of interest, in this study, uses mechanical shocks to de-ice ground wires by taking advantage of the brittle behavior of ice at high strain rates [44]. This method uses a portable de-icing device, called DAC (De-icer Actuated by Cartridge) and is aimed at de-icing steel OHGWs and OPGWs one span at a time.

This study therefore focuses on the dynamic analysis of iced overhead transmission lines subjected to in-span shock loads such as those that may result from the effect of an external load intended to remove accreted ice from the cable or from load imbalances due to sudden ice shedding.

1.3 Research objectives

The goal of this study is to understand the dynamic effects of shock-load-induced ice shedding on overhead lines by proposing a numerical model using nonlinear finite element analysis. In this study, shock loads result from an external impulse-type load intended to remove accreted ice from the cable.

The specific research objectives are:

1) to develop a numerical model where the ice deposit is explicitly considered so that modeling of ice failure propagation along the span becomes possible.

2) to apply this novel iced cable modeling approach to study the dynamic effects of shock-load-induced ice shedding on real-scale overhead lines.

3) to investigate how variables including ice thickness, line parameters such as span length, cable tension and axial rigidity, and pulse-load characteristics affect the dynamic responses of iced cables subjected to mechanical shocks.

4) to compare the dynamic responses of iced cables subjected to mechanical shocks obtained from numerical simulations to those observed in reduced-scale laboratory experiments.

1.4 Originality and contributions to knowledge

In most previous studies of ice shedding on lines [32, 48, 66 and 67], the response of the line to instantaneous shedding was modeled. Actual observations of natural ice shedding on lines are scarce, and the assumption of instantaneous random shedding on span sections cannot be discarded especially when shedding is triggered by melting. However, experiments on mechanically-induced shedding show the progressive shedding of ice along the span as an "unzipping" effect [44]. Therefore, in this study, a numerical model considering the propagation of ice shedding along the span is needed.

Coupling this new modeling approach of ice shedding with several previous modeling approaches of transmission lines [42, 49 and 52] subjected to icing would provide a

powerful simulation tool for several practical industrial applications. This new modeling approach may also help to improve the design of the DAC de-icing device [44] in particular.

1.5 Methodology

This research is carried out mainly in two stages:

1) numerical simulations using finite element modeling of overhead iced cables subjected to mechanical shocks and

2) physical simulations using reduced-scale laboratory experiments of a suspended iced cable subjected to mechanical shocks.

In both stages, the mechanical shock loads result from an external load intended to remove accreted ice from the cable.

1.5.1 Finite element modeling

As in previous numerical studies [32, 66 and 67] of ice shedding on line conductors, the commercial finite element software package ADINA [2] is used here to simulate the dynamic effects of ice shedding induced by a pulse-type excitation applied directly on the cable of a level single-span section.

The finite element modeling of overhead iced cables subjected to mechanical shocks is carried out in the following steps:

Modeling assumptions:

1) Several different iced cable modeling approaches are investigated in order to model ice failure propagation along the span. The cable is modeled with a uniform mesh of prestressed tension-only isoparametric truss elements relying on successful previous studies [32, 42, 49, 52, 66 and 67]. The novelty introduced in this research is that the ice deposit on the cable is modeled as a separate beam element parallel to each cable element (Fig. 3.1). Four ice-deposit elements available in ADINA were deemed worthwhile to be investigated: the isoparametric truss, the Hermitian beam, the isoparametric beam- and the pipe-beam with post-elastic behavior.

2) Ice failure and subsequent shedding or detachment is modeled using the "element death upon rupture" option available for the beam (iso- and pipe-) elements with a plastic bilinear material model [2].

3) Several ice-shedding scenarios are studied with variables including ice thickness and line parameters such as span length, cable tension and axial rigidity, and pulse-load characteristics. However, the flexibility of the towers and their foundations is not modeled and the cable ends are assumed to be rigidly fixed.

4) In this study, shock loads result from the effect of an external point load intended to remove accreted ice from the cable, similarly to the DAC system. However, the exact time functions of the shock loads generated by the DAC [44] are confidential information. Therefore, the shock load used in this study is simply defined by a triangular pulse-type excitation, which is defined as a concentrated vertical upward

force (Fig. 3.1a). Different pulse-load characteristics are represented by the variation of load amplitude and pulse duration.

5) Aerodynamic damping is neglected and only structural damping of the iced cable is considered in the numerical models. Therefore, damping is modeled by using a non-linear axial dashpot element parallel to each cable element (Fig. 3.1b) relying on previous studies [32, 42, 49, 52, 66 and 67].

Sequence of analyses:

6) Before starting the transient dynamic analyses, several natural frequencies and mode shape analyses are conducted on various iced-span models to validate and adjust the parameters of the mesh and investigate alternative modeling approaches. The calculated mode shapes and corresponding natural frequencies are compared to each other, and to those obtained from Irvine's theory [31], respectively.

7) The selection of the time step and the mesh size is such as to provide adequate sampling of the shock wave as it travels through the cable finite element mesh. Then, to validate the finite element mesh size and type of elements selected for both the cable and the ice, several mesh densities are investigated.

8) Dynamic analyses start from the initial static equilibrium of the iced cable. In order to avoid the stiffening effect of the flexural rigidity of the ice beam (Hermitian-, iso- or pipe-) elements on the initial static profile, the deformed cable profile is calculated beforehand using an increased density cable model as in previous studies [32, 42, 52,

66 and 67]. This deflected static profile serves as the initial profile of the ice-cable composite model.

9) The failure criteria of glaze ice in terms of axial and bending stress-strain relations, and strain-rate effects in particular, are based on the mechanical properties of fine-grained freshwater ice published in the literature, since it is the best information available. However, further refinements of the failure criteria of glaze ice deposits can be readily integrated into this model as they become available.

1.5.2 Reduced-scale laboratory experiments

The reduced-scale laboratory experiments on a suspended iced cable subjected to mechanical shocks are carried out in the following steps:

Description of the experimental setup:

1) The experimental setup is installed at the CIGELE icing precipitation simulation laboratory. It consists of a rigid support mounting a flexible stainless-steel cable pin-ended to load cells.

2) The shock load (impact) is provided by a pneumatic cylinder (pneumatic shock load generator) installed at the cable mid span.

3) Voltage excitation and signal conditioning are provided by a four-channel signal conditioner for the piezoelectric force sensor and by strain gauge signal conditioners for each strain gauge load cell. Data acquisition is provided by a computer with a USB

interfaced analog-digital converter. Data acquisition is controlled by the DT Measure Foundry DAQ software [11].

4) Ice accretion onto the cable is provided by a water spraying system installed at the CIGELE icing precipitation simulation laboratory.

General experimental considerations:

5) Horizontal and vertical components of cable end-tensions in both the static and dynamic regimes are measured by the load cells.

6) The force acting on the cable due to the impact is measured by a piezoelectric force sensor mounted on the end of the pneumatic cylinder piston rod.

7) Time histories of the vertical displacement of the cable at mid span are monitored using a digital high-speed camera. Images are processed to yield some quantitative time history responses.

8) Several ice-shedding scenarios are studied with variables including ice thickness and pulse-load characteristics. Pulse-load characteristics are defined by the load amplitude and pulse duration considering the capacity of the pneumatic shock load generator. The initial cable tension and span length are kept constant.

9) Experiments are carried out in the 0°C to -10°C temperature range most likely prevailing when structures are exposed to severe atmospheric icing.

1.6 Thesis organization

This introduction chapter has presented the motivation for this research: the increasing need of reliable de-icing and anti-icing methods aimed at preventing power lines from getting damaged following severe atmospheric icing events and therefore the necessity of this study dealing with a narrow section of the problem, i.e. the effects of ice removal on overhead transmission line cables by mechanical shocks. The objectives and the original contributions of this research along with the methodology have also been presented. The thesis is composed of seven more chapters outlined next.

The salient features of a comprehensive literature survey related to the mechanical problems associated with atmospheric icing of power lines, recent de-icing and anti-icing methods and recent numerical model developments of the ice shedding phenomenon are summarized in Chapter 2. A brief review of current knowledge on the mechanical properties of atmospheric ice is also included. Chapter 3 presents the newly developed finite element model that explicitly considers the rupture of ice deposit by integrating the mechanical properties of ice into the model. Limitations of the numerical model are also highlighted in this chapter, followed by the presentation and discussion of the typical numerical model results of a single-span of an overhead ground wire. The reduced-scale experimental setup and the description of a typical test sequence along with the test results are introduced in Chapter 4. A comparison of numerical and experimental results of the reduced-scale model is presented in Chapter 5. The numerical model is applied to simulations of real-scale lines and the results of several ice-shedding scenarios with variables including ice thickness, line parameters such as span length, cable tension and

axial rigidity, and pulse-load characteristics are discussed in Chapter 6. Chapter 7 introduces alternative ice-modeling approaches and discusses the effect of numerical procedures and finite element formulations. In addition, thematic conclusions are given at the end of each chapter as relevant, while the general conclusions and recommendations for numerical model improvements and future studies are presented in Chapter 8. Key references are also provided.

Appendix A provides a summary of the basic theoretical expressions used in this study, such as the equation of the catenary, the equations of the transverse and longitudinal waves in transmission line cables and the natural frequencies and mode shapes of suspended cables. Experimental test parameters including the parameters involved in icing, parameters of the shock load generator, damping of the level single-span reduced-scale conductor model and the characteristic material properties of the wire rope obtained from static tensile tests are presented in Appendix B. Appendix C summarizes the main parameters of the cables used in this study: a Condor ACSR 54/7 conductor, a classical stranded steel ground wire, an optical ground wire, an extra-high strength ground wire used for long-span lines and the stainless steel wire ropes used for the experiments. In Appendix D, program codes written in FORTRAN to calculate the static profile of a level single-span axially rigid catenary under its self-weight and the natural frequencies of a level single-span suspended cable are presented. Technical drawings such as the reduced-scale conductor model assembly, the schematic of the shock load generator and that of the instrumentation are presented in Appendices E, F and G, respectively.

CHAPTER 2

LITERATURE REVIEW

2.1 Atmospheric icing

2.1.1 Introduction

Atmospheric icing is a complex phenomenon that results either from precipitation icing or from in-cloud icing [30]. It may take place at ambient air temperatures between -10°C and 0°C, or sometimes, at lower temperatures under particular conditions. The occurrence, severity, and type of atmospheric icing depend largely on temperature, wind speed, total water content of the air, and water droplet size.

In-cloud icing occurs when suspended, supercooled droplets freeze immediately upon impact on an object exposed to the airflow. The occurrence and severity of this type of atmospheric icing strongly depend on the location of the exposed object and on the topography of the surroundings.

Precipitation icing can take the form of freezing precipitation and frozen precipitation. Freezing precipitation occurs when any form of precipitation (freezing rain, freezing drizzle, or freezing fog) freezes upon impact on or contact with an exposed object. Frozen precipitation is any form of precipitation that reaches the ground in frozen form such as snow, snow pellets, snow grains, ice crystals, ice pellets, and hail [30].

2.1.2 Types of ice accretion

Essentially five types of ice accretion may deposit on structures, as defined in Table 2.1, that are basically classified by their density as glaze, rime (soft and hard), wet snow, dry snow, and hoar frost [63].

Type	Description	Density (kg/m^3)
Glaze	Hard, almost bubble-free, clear homogenous ice with a density close to that of pure ice. Very strong adhesion.	700 – 900
Hard rime	Rather hard, white or translucent homogenous ice with inclusions of air bubbles. Strong adhesion.	300 – 700
Soft rime	White or opaque ice with a loosely bonded structure ("feather-like" or "cauliflower-like"). Can be removed by hand.	150 – 300
Wet snow	Opaque ice with a crystal size much smaller than that of glaze ice. When the temperature is close to zero it may possess high liquid water content and slip off easily. If the temperature drops after the accretion, it may have very strong adhesion.	100 – 850
Dry snow	Very light pack of regular snow. Very easy to remove.	50 – 100
Hoar frost	Crystal structure (needle-like, scale-like). Low adhesion.	< 100

Table 2.1 Types and characteristics of ice accretion (adapted from [8, 19 and 63])

Glaze ice forms on exposed objects by the freezing of a film of supercooled water (i.e. water still in the liquid phase but at sub-zero temperatures) deposited by rain, drizzle, or fog. The large droplet size, slight supercooling, and slow dissipation of heat of fusion favor the formation of glaze which is the most probable at temperatures between 0°C and -3°C [19]. It produces the densest form of atmospheric icing and on overhead power lines in particular, very large ice loads are reached within hours [8].

Rime ice forms when the freezing of small, supercooled water droplets impinge upon an exposed object at air temperatures typically below -5°C. The small droplet size, slow

accretion, high degree of supercooling, and rapid dissipation of heat of fusion favor the formation of rime [19]. Rime density varies depending on the size of droplets and the freezing time (Fig. 2.1). When the droplets possess small momentum and freeze quasi-instantly on impact, air pockets are created between the frozen droplets and a soft rime deposit is produced. When the droplets possess greater momentum, or the freezing time is greater, the frozen droplets pack closer together in a dense structure and create a hard rime deposit [63].

Wet snow commonly occurs as an agglomeration of snow flakes at temperatures just above the freezing point (0.5-2°C) and is a mixture of ice, liquid water and air [65, 68]. If free water entirely fills the air space in the snow, it is classified as "very wet" snow. Snow flakes are more likely capable of causing wet snow accretion at liquid water content between 15 and 40% in mass (i.e. percentage of the mass of liquid water per the total mass of wet snow) [8, 65]. The density range of wet snow deposits depends on the wind force that compresses the snow on the surface of accretion. It may have strong adhesion with the exposed objects, and like glaze ice, it can lead to very high loads within hours on overhead conductors.

Dry snow flakes may also accumulate on objects to form a dry snow accretion at temperatures significantly below freezing point under very low wind speed conditions [8].

Hoar frost forms when the vapor in the air with a dew-point below freezing condensates [19]. It causes very thin and porous layers of ice usually on the windward side of objects and is therefore not critical when the ice is regarded as a gravity load as these deposits have low density. However, large hoar frost deposits on overhead conductors may

result in significant wind loads.
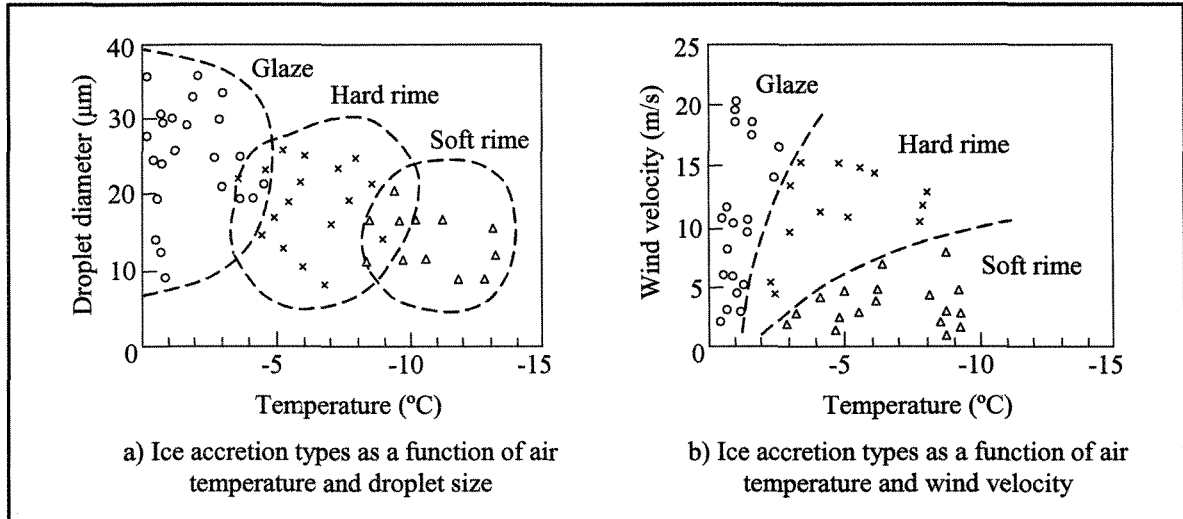
Figure 2.1 Ice accretion types (adapted from [16])

2.1.3 Accretions on overhead transmission lines

As discussed in the previous section, ice can deposit on overhead transmission line cables and their supporting structures in different forms and densities. The types of atmospheric ice accretions that are significant for our purpose are heavy adherent wet snow, hard rime, large deposits of lightweight rime ice, and dense glaze ice. In this section, examples of these types of atmospheric ice accretions on transmission lines are illustrated. Figures 2.2a, b and c present examples of glaze, wet snow and rime accumulations on overhead conductors, respectively.

a) Glaze accumulation on overhead conductors (source: Brownstown Electric Supply Co., Inc.)

b) Wet snow accumulation on overhead conductors (source: [18])

c) Rime accumulation on overhead conductors (source: [18, 27])
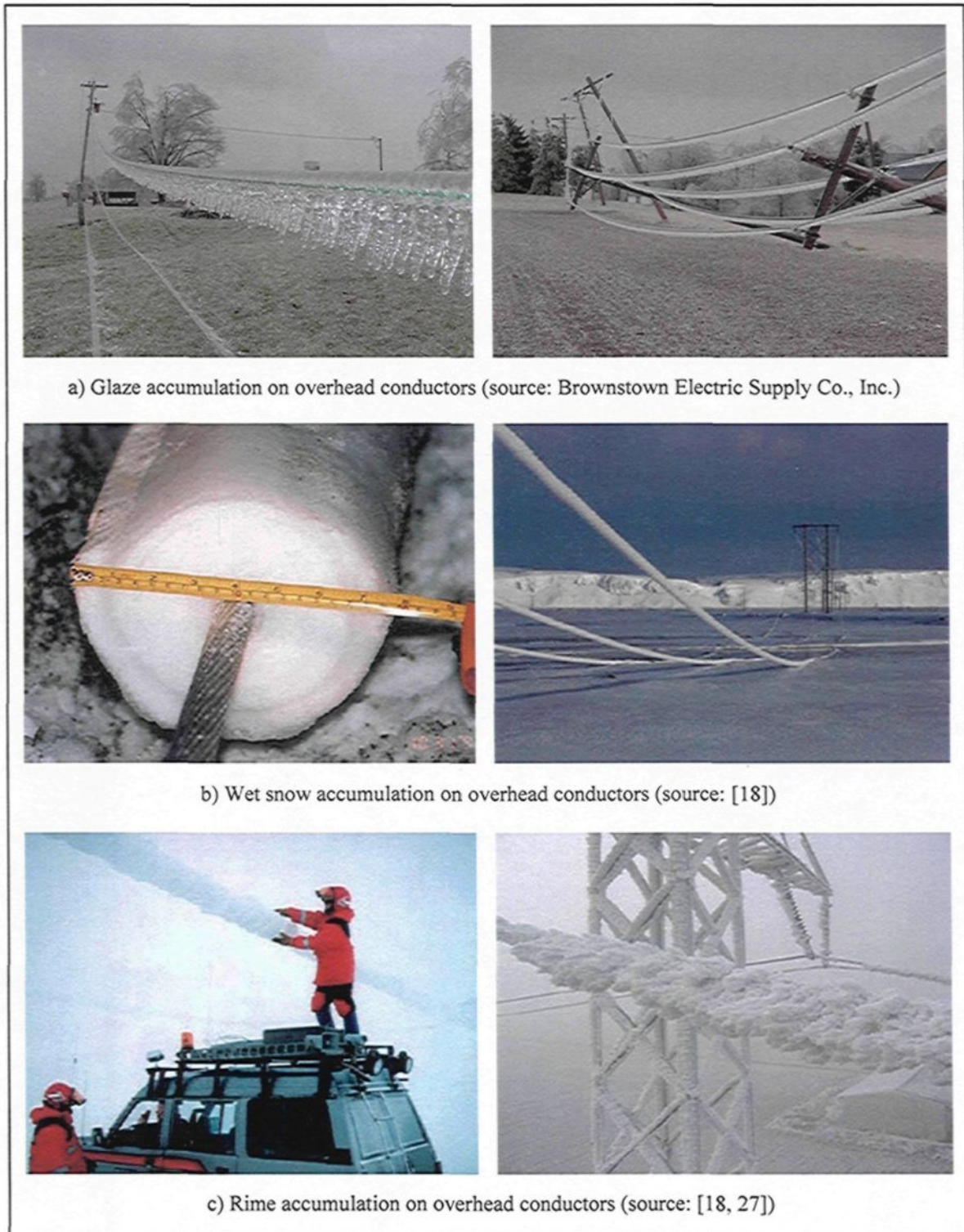
Figure 2.2 Atmospheric ice accretions on overhead conductors

2.2 Ice-related loads on overhead transmission lines

2.2.1 Introduction

Ice accretions on exposed transmission line cables and their structures can be the source of several mechanical and electrical problems. In this study, only the ice-related mechanical problems are emphasized.

The gravity loads due to heavy ice accretion on overhead lines, coupled with wind-on-ice loads, may lead to structural damages, or failure and even cascading collapse of towers. Ice shedding from cables, wind-induced cable motions such as galloping associated with aerodynamically unstable ice profiles and severe Aeolian vibrations of ice-covered cables are among the most severe loads acting on transmission lines.

2.2.2 Ice shedding

Ice shedding is the physical phenomenon that occurs when accreted ice on the overhead cables drops off. It is responsible for large imbalance forces and moments on supports, impact forces, overloads, vibrations, and in the case of electrical conductors, short-circuits causing flashover [13] when electrical clearances become insufficient. In extreme situations, the increased cable tensions may result in broken insulator assemblies, or short circuits may cause cable breakages that may in turn lead to longitudinal cascading failure of the line [5, 48]. Despite the serious potential consequences of ice shedding, actual observations of natural ice shedding on lines are scarce and therefore the phenomenon still requires additional research.

Three physical mechanisms are expected to induce ice mass reduction or ice shedding. These mechanisms are ice melting, ice sublimation and mechanical ice breaking [7, 13]. Each type of ice shedding can be identified from atmospheric parameters (air temperature, wind velocity and direction, relative humidity), ice load variations, ice shedding duration, and ice strength [13].

Natural ice shedding by melting obviously occurs when the air temperature is above 0°C. It also requires a small amount of accumulated ice on the line when only the outer surface of the ice is affected by the temperature. However, if the cable is already partly ice-free, it can transfer the heat to the cable-ice interface leading to ice melting that reduces the adhesive strength of the ice to the cable. This mechanism is characterized by a relatively low shedding rate and depends on the air temperature, solar radiation and wind velocity. When the adhesive strength of the ice is less than the aerodynamic and/or gravity forces, ice chunks start falling [7, 13].

Ice mass reduction by sublimation takes place at the ice-air interface when the temperature is below 0°C. The amount of ice sublimated depends on several atmospheric factors such as the temperature, relative humidity and wind velocity, as well as on the extent of the ice surface [7, 13]. The sublimation rate increases as the temperature, wind velocity and ice surface increase, while the relative humidity decreases. Measurements [7, 13] have shown that the ice mass reduction rate by sublimation is low (3-20 g/m·h). However, the phenomenon can be apparently observed during several consecutive days, and the total ice mass reduction can be important.

Natural ice shedding by mechanical ice breaking usually occurs at temperatures below 0°C when forces acting on the iced line section initiate the adhesive or cohesive failure of the ice deposit in terms of stress-strain relations beyond the ice crystal rheological limits. The initiation and propagation of such failures are complex and can be induced by static (torsion, flexure, tension) or dynamic loads related to wind effects. It can be expected that the wind velocity, temperature, ice load and ice strength influence the natural ice shedding by mechanical breaking. Very little is known about this complex phenomenon and therefore this research is also aimed at increasing this knowledge.

Furthermore, full-scale physical observations [40] indicate that when shedding is initiated by melting, the shedding mechanism can extend to mechanical ice breaking. It is explained by the fact that during the melting process, liquid water film forms on the surface of the cable at the interface thus allowing the eccentric ice deposits to rotate and reach a static equilibrium. Then water covered ice deposits begin to break off in large pieces at the center of the span. After the initial ice chunks fall to the ground, ice deposits located at higher positions on the span begin to slide down along the cable towards the mid span and strike either other pieces of ice or an obstacle positioned at a lower level. As they strike other pieces of ice, mechanical ice breaking may take place (Fig. 2.3).

a) Sliding and shocking ice deposits at the   b) Few seconds later
cable mid span
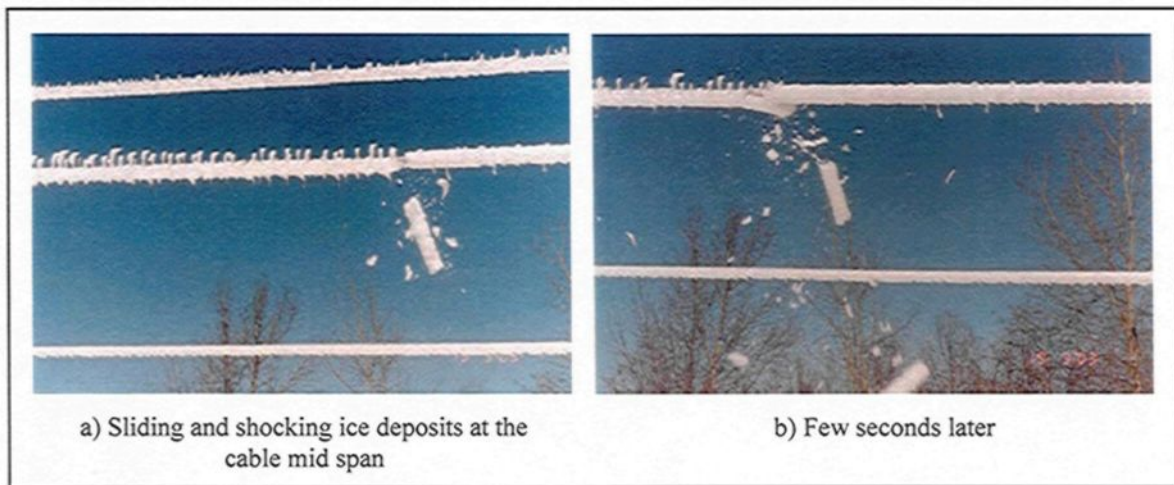
Figure 2.3 Ice shedding by melting coupled with mechanical ice breaking (source: [40])

2.2.3 Galloping

Galloping is defined as low frequency and high amplitude wind-induced vibration of both single and bundle conductors due to aerodynamic instability, with a single or a few loops of standing waves per span [16, 73]. Four sources of conductor galloping are distinguished. They are: corona galloping, bare-wire galloping, wake-induced galloping and iced conductor galloping [16]. However, the most often observed galloping on overhead lines is associated with aerodynamically unstable ice profiles [26, 73] and therefore the term galloping used in this study represents iced conductor galloping only.

Galloping usually occurs when a moderately strong and steady crosswind (above 7 m/s) acts upon an asymmetrically iced conductor surface. The wind at an angle greater than 45° to the line with a small (a few mm may suffice) ice deposit on the conductor can lend suitable aerodynamic characteristics of the iced cable to gallop and may position the ice deposit (angle of attack) to favor aerodynamic instability (Fig. 2.4) [16]. Hard rime and

glaze are responsible for most conductor galloping as they have sufficient strength and flexibility to withstand the forces deriving from the galloping motion. Wet snow accretions may also result in ice shapes on the windward side of conductors that lead to galloping. Little ice thickness (1 or 2 mm) is required for galloping but galloping has also been observed with ice thickness as great as 5 cm [16]. Most of the galloping observed occurred at temperatures close to 0°C [73].

The ability of the ice-cable composite to gallop is also affected by the torsional rigidity of the span [16]. It is explained by the fact that the eccentric weight of ice deposit on the conductor in a span with low torsional rigidity may twist the conductor (Fig. 2.5) resulting in a shape of ice with aerodynamic characteristics less conducive to galloping. However, significant conductor rotation during ice accretion is prevented to occur in bundled conductors due to the torsional restraint provided by spacers. Therefore, bundled conductors are widely thought to be more prone to galloping than single conductors.

Galloping can cause various kinds of structural damage in overhead lines. Some types of damage result directly from the large forces that galloping waves or loops apply to the supports (e.g. crossarm failure, broken insulators etc.): many of these failures are related to low-cycle fatigue. It is often reported that the amplitudes of galloping conductors are in a vertical plane (but not always) (Fig. 2.6) and can be very large, sometimes in the order of the sag of the line, increasing the risk of flashover between different phases or from phase to ground. Flashovers can result in broken strands or complete failure of conductors or ground wires [16, 26].
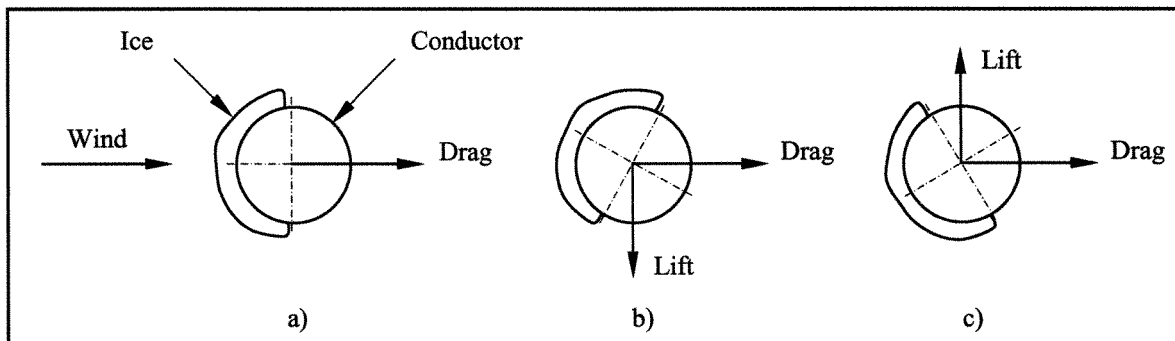
Figure 2.4 Aerodynamic instability of iced conductor (adapted from [16])
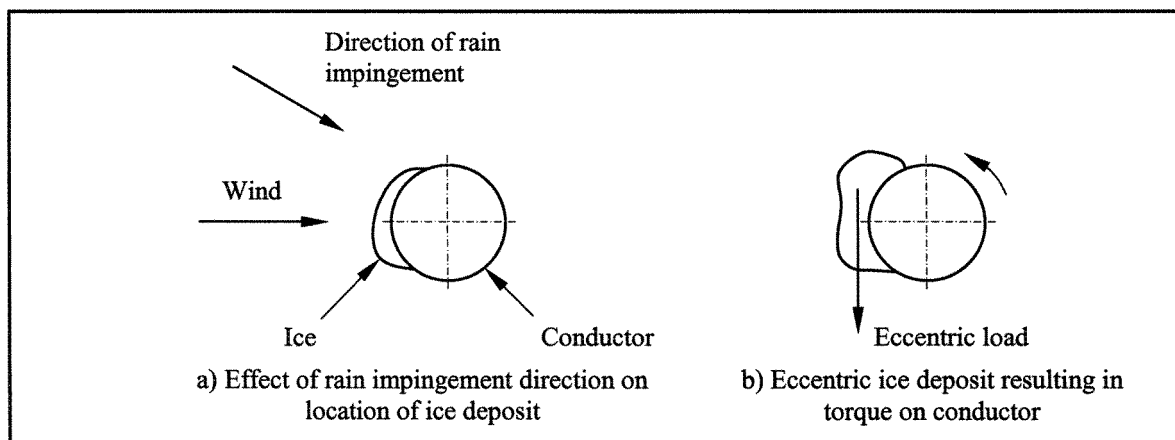
Figure 2.5 Eccentric weight of ice deposit (adapted from [16])
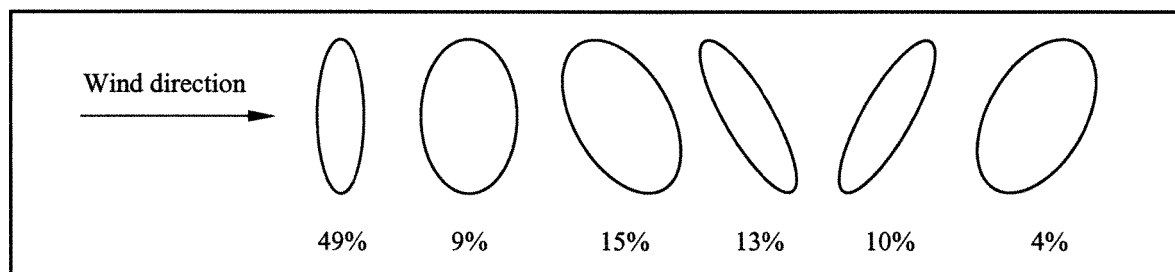
Figure 2.6 Percentage of observations of various galloping paths and tilts (adapted from [16])

2.2.4 Aeolian vibration

Severe Aeolian vibrations of the enlarged-diameter, ice-covered conductor may also lead to fatigue failures of conductor strands at suspension clamps. In opposition to galloping, Aeolian vibration is defined as high frequency and low amplitude wind-induced vibration of both single and bundled conductors. The peak-to-peak amplitude rarely exceeds one conductor diameter. The primary cause of this type of conductor vibration is the alternate shedding of wind-induced vortices from the top and bottom sides of the conductor that creates an alternating pressure unbalance which causes the conductor to move up and down at right angle to the direction of air flow [16]. Aeolian vibrations usually occur when a steady, low-velocity crosswind (below 7 m/s) acts upon a bare or uniformly iced conductor surface.

Fatigue failure of conductor strands is the most common form of damage resulting from Aeolian vibration. It is caused by cyclic stresses resulting from alternate bending of the conductors where their motion is restrained (e.g. at support locations, suspension clamps etc.) [16]. Several methods are used to protect the line against vibration fatigue. The most widely used technique is the addition of external damping devices to the conductor that dissipate some of the mechanical energy in the vibrating span.

Increasing conductor damping also tends to decrease the amplitudes of vibration. However, uniform hoar frost accretion preserves the cylindrical shape of the conductor, and increases its diameter without significant change in conductor damping and therefore it tends to increase the amplitudes of vibration with respect to bare conductor diameter. This is due to the fact that the wind power input to the conductor increases in proportion to its

diameter despite the lower frequency vibration induced. Furthermore, the lower frequencies may fall below the efficient operating range of vibration dampers and they may also experience fatigue failure. It was also found that vibration fatigue failures are more likely to occur with high conductor tension [16].

2.3 Transmission line de-icing and anti-icing techniques

2.3.1 Introduction

In the previous section, the effects and mechanisms of ice-related loads on transmission lines were emphasized that revealed the possible serious consequences of such loads. Therefore, in order to protect the line against loads resulting as a consequence of accreted ice on the line and to ensure the reliability of electrical power delivery networks, various mitigation methods have been used. One category of these methods deals with the root of the problem, such as to remove or prevent formation of ice deposits on overhead lines.

In general, methods that are used after an ice storm when the line is covered with a significant sheet of ice are termed as de-icing techniques. They aim essentially to limit the time it takes to restore the lines to service (with sufficient electrical clearances) after a storm and to limit the extent of damages. On the other hand, methods that are applied before an ice storm and thus prevent the formation of significant ice deposit throughout the precipitation period are termed as anti-icing techniques. However, de-icing systems that are put into action early in a storm when the ice layer is still thin (1 or 2 mm) can be considered as anti-icing devices [39].

De-icing and anti-icing techniques can be classified according to various criteria [74]. First, classification can be made based on the physical principle used in the method to remove the ice from the structure, such as thermal, mechanical, passive and miscellaneous methods [39]. Then, they can be classified in terms of their applicability to ground wires, energized conductors, or to both [74]. Another classification is proposed to illustrate the permanent or temporary character of the method, its operational mode (automated or manual) and the need for line modification, such as inline, punctual and permanent [74].

In recent years, a total of 37 line de-icing and anti-icing techniques were reported potential for power lines [74]. These 37 techniques were classified as anti-icing (11), de-icing (13) and mitigation (13) methods. At the time of this inventory (2005), among the 37 techniques, 15 were operational, 4 had been tested, 13 were at a conceptual or developmental stage and 3 at the prototype stage. However, among the 15 operational methods only 7 were found effective and 2 had been proof-tested for ice prevention or de-icing. Out of the 7 effective methods, 4 are inline thermal methods based on the Joule effect and 3 are punctual (i.e. temporarily installed or used only once) mechanical methods [74].

2.3.2 Thermal methods

The heating of ice-covered lines by an electrical current based on the Joule effect is recognized worldwide as the most efficient engineering approach to minimize the consequences of severe ice storms on overhead lines [74]. The efficiency of de-icing and/or anti-icing, i.e. ice melting, depends on various parameters including the ambient air

temperature, ice thickness, conductor diameter, thermo-physical parameters of the ice and the conductor, mean heat transfer coefficient, and electric current [60]. Both types of current (AC and DC) have been used in different countries to melt ice on power lines [74].

The de-icing techniques most widely and effectively used by Hydro-Québec are based on the Joule effect [64]. Several of these techniques have been developed worldwide for both energized conductors and ground wires. However, their application to ground wires has several serious drawbacks: they require an external power source, the ground wire needs to be insulated from the tower, spark gaps need to be installed to protect insulators from direct lightning, and the grounding resistance increases, to name a few [64]. Therefore, several methods aimed at de-icing overhead ground wires have been developed by Hydro-Québec TransÉnergie in recent years [43, 44].

2.3.3 Mechanical methods

Mechanical methods are based on the breaking of ice deposits. Two of the aforementioned methods aimed at de-icing overhead ground wires following severe atmospheric icing are considered to be punctual (i.e. temporarily installed) mechanical methods [43].

The automation of a manual device (Fig. 2.7a) that was initially operated from the ground with a pulling rope has led to the development of a Remotely Operated Vehicle (ROV) (Fig. 2.7b) [43]. This device provides gradual de-icing of overhead cables without inducing significant dynamic loads on structures. It was successfully tested on 315 kV live-line conductors that revealed that the ROV electronics are protected against

electromagnetic interferences and that the device has an operational range of 1 km [43].

| a) Manual prototype of the de-icer | b) Prototype of the ROV de-icer |
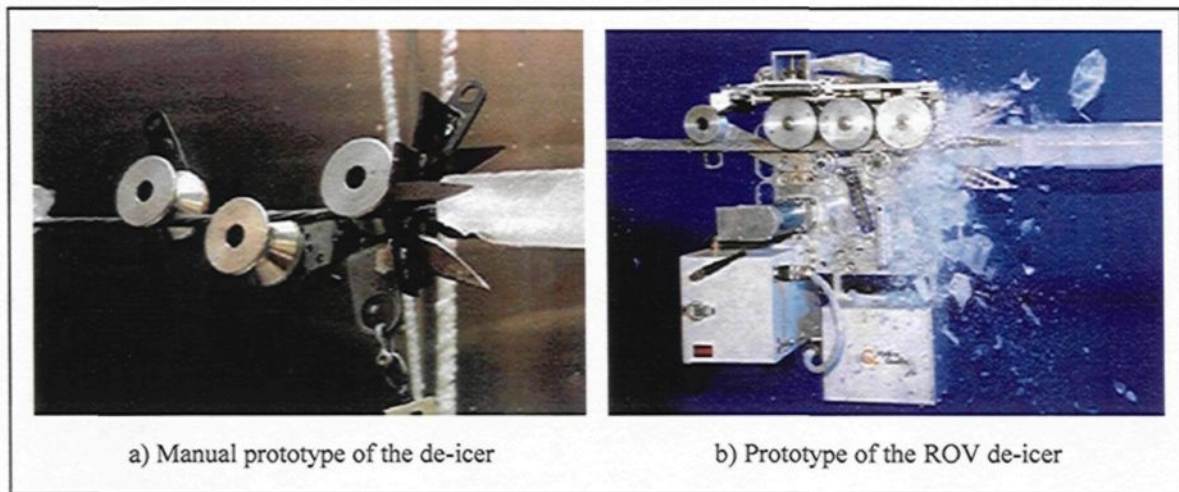
Figure 2.7 De-icer by remotely operated vehicle (source: [43])

Another mechanical method has also been developed that uses mechanical shocks to de-ice the ground wire taking advantage of the brittle behavior of ice at high strain rates. Since this method is the subject of interest in this study, the de-icing device is presented in detail. The mechanical de-icing device illustrated in Figure 2.8 is called DAC (De-icer Actuated by Cartridge) and is aimed at de-icing steel conventional and optical overhead ground wires one span at a time [43, 44].

DAC consists of a portable cylinder-piston system that is firmly kept into contact with the cable through an open-ended clamp. It generates transverse waves in the cable (Fig. 2.9) through a powerful gas expansion by remotely firing cartridges in a barrel. The transverse waves generated propagate along the span and can remove the accreted ice deposit by breaking it down into small fragments (Fig. 2.10). This ice-breaking action

absorbs energy from the traveling waves and reduces their amplitude. The waves die out when all the power conveyed by the waves has been absorbed by the ice and the cable. They may reach the span extremities with enough energy to be reflected back in the span with reverse amplitude and therefore they may propagate back and forth with slowly decreasing amplitude. The operation can be carried out entirely from the ground using a line-thrower to install the device onto the overhead cable, which represents a major advantage. Numerous tests have been performed at Hydro-Québec's research institute on both OHGWs and OPGWs to assess the efficiency of this method and to optimize its physical parameters. In 2005, the project was reported to be at the industrial stage and the prototype was ready to be tested under field conditions [44].
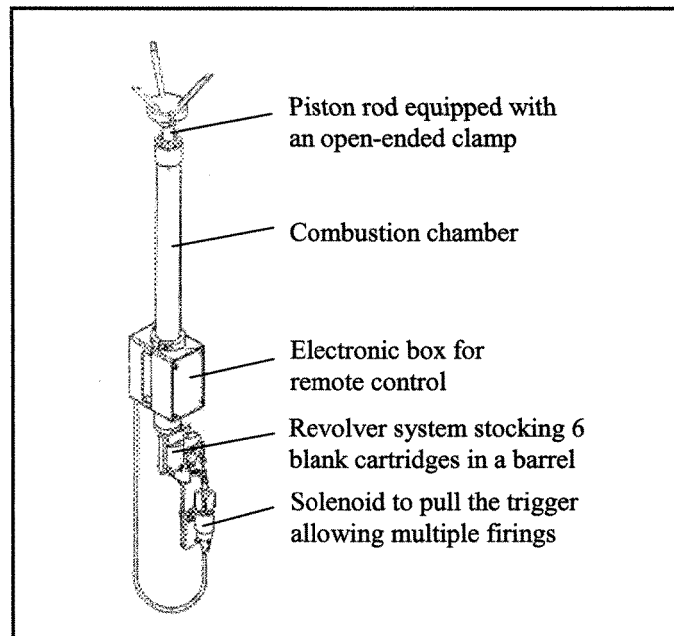
Figure 2.8 Sketch of the DAC prototype (adapted from [44])
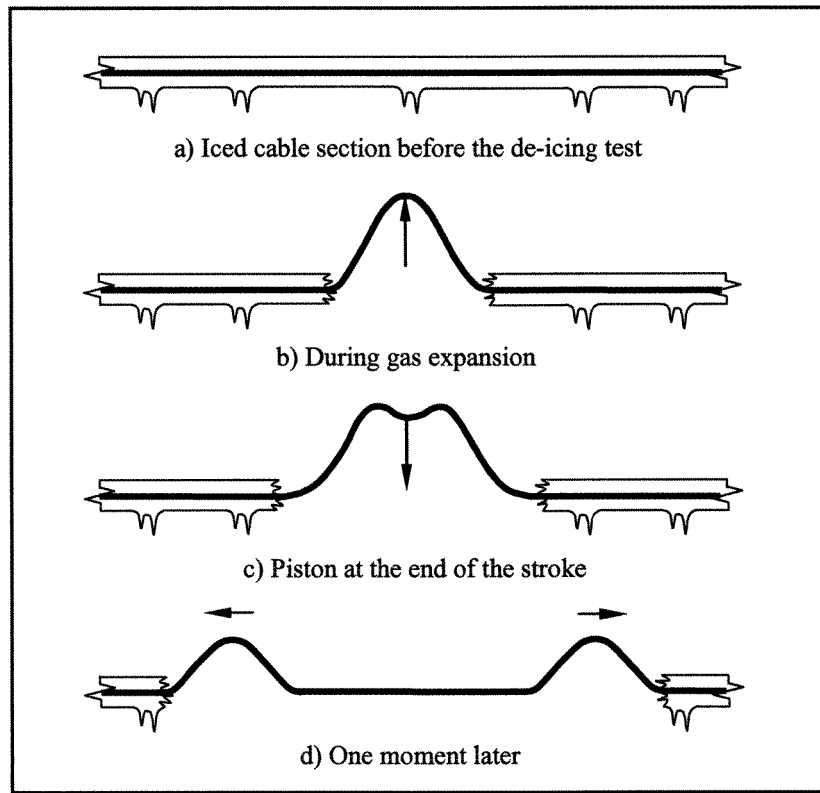
Figure 2.9 Schematic of transverse wave propagation and ice breaking
(adapted from [44])

2.4 Mechanical properties of atmospheric ice

As it was already stated, the ice deposit breaks when the forces acting on the iced line section are large enough to initiate the adhesive or cohesive failure of the ice accretion. In order to predict (with reasonable accuracy) the magnitude of these forces, it is necessary to know the mechanical properties of atmospheric ice. However, despite much research effort in the last few decades, information about the mechanical properties of atmospheric ice in natural conditions is still lacking.

Nevertheless, a detailed microstructure and air bubble analysis of ice samples collected from transmission lines after significant ice storms [38], and a complementary texture analysis of laboratory ice samples [20], as well as experiments on the ductile-brittle transition of laboratory glaze ice under compression [12], indicate that the mechanical properties of fine-grained freshwater ice are a reasonable assumption for this study. The mechanical properties of freshwater ice are presented in the next section.

a) Iced span before the de-icing test   b) Iced span during the de-icing test

c) Span after the de-icing test (with colored
ice fragments on the ground)
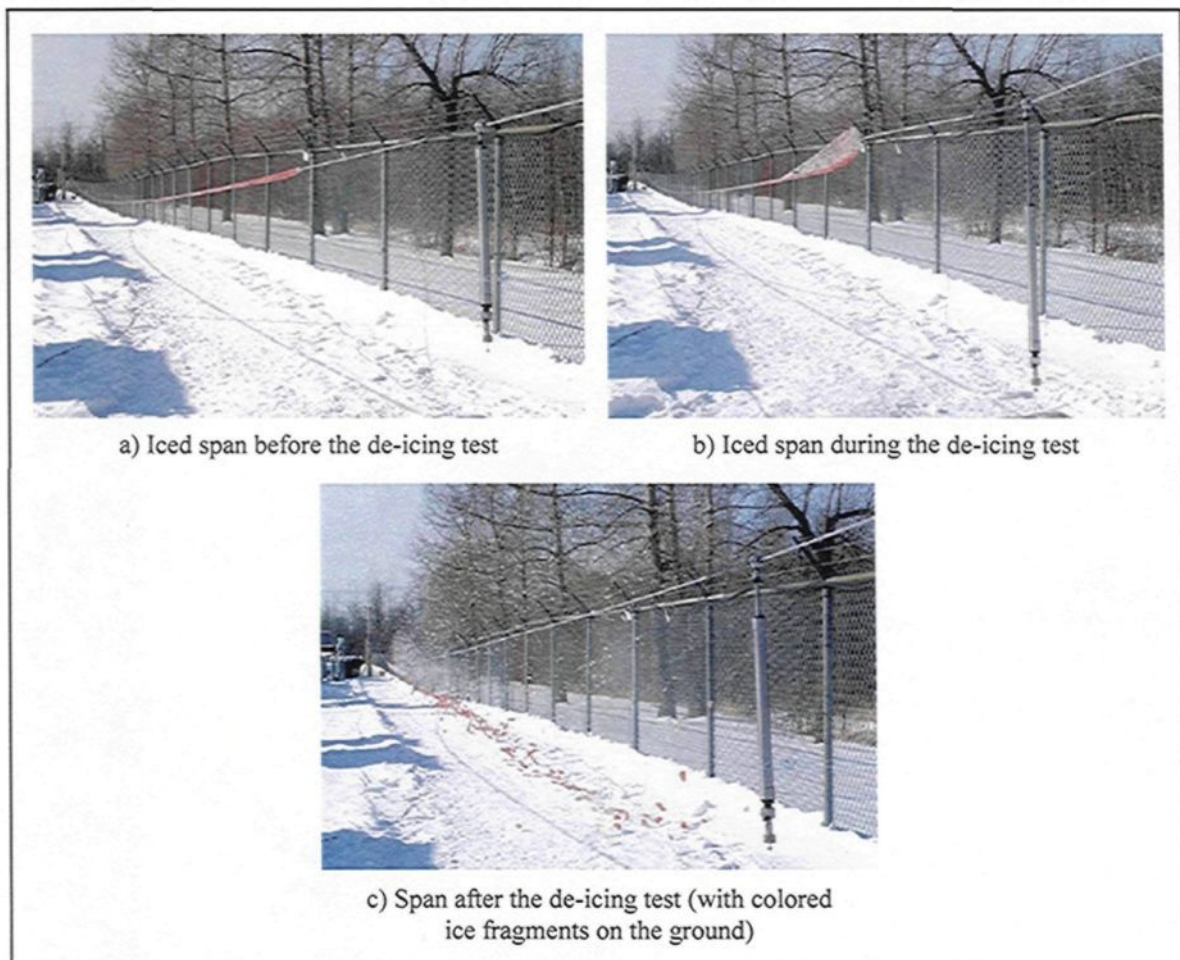
Figure 2.10 Photos of a de-icing test by DAC showing the transverse wave
propagation and ice breaking (source: [44])

2.5 Mechanical properties of freshwater ice

2.5.1 Microstructure of ice

On the macro-scale, ice is a polycrystalline material and its texture depends on the freezing process and its thermo-mechanical history [70]. It can be classified according to grain shape, size, and crystallographic orientations such as granular and columnar ice. Granular ice (T1 ice) is an isotropic material in which the crystallographic orientations of the c-axes (i.e. normals of the crystallographic basal planes) are randomly oriented. Three types of columnar ice are distinguished and labeled S1, S2 and S3. In S2 columnar ice the c-axes are randomly distributed in a plane perpendicular to the columns, while in S1 the c-axes are aligned in the columnar direction. In S3 the c-axes are also in a plane perpendicular to the columns (as in S2) but in a preferred direction rather than randomly. Both the S1 and S2 ice crystals can be considered as a transversely isotropic material, while S3 is orthotropic [20].

The texture of atmospheric ice deposits on power lines can be classified as columnar (S1 and S2), feathery, and granular based on its grain shape [20]. Glaze is considered to be S2 columnar ice in a very wet regime of ice accretion and S1 in the transition regime from wet to dry. On the other hand, soft rime accreted in the dry growth regime has a fine granular structure, while hard rime has a columnar to granular structure (feathery). The mean crystal width measured on natural [38] and laboratory [20, 38] ice samples is a few millimeters (below 5 mm) depending on the sampling location above the conductor surface and on different growth conditions.

2.5.2 Characteristics of ice under tension, compression and flexure

Ice is a very complex material: its mechanical properties depend on crystal structure, temperature, presence of impurities, and type, rate and direction of loading. In short-term loading, ice behaves elastically and fails in a brittle manner. However, if the loading rate is low (below 10^{-5} s^{-1}), creep and plastic failure predominate [12, 19, 20 and 70].

In the case of ice breaking induced by mechanical shock loads, the main properties that govern the failure of the accreted ice deposit on cables relate to the tensional (axial) and flexural strengths and rigidities of the iced section. In addition, the properties of ice associated with short-term loading are assumed to prevail. Therefore, the characteristic properties of ice under tension, compression and flexure are introduced next.

Ice under tension becomes brittle at a much lower strain rate than it does when it is under compression (Fig. 2.11) [12, 19, 20, 61 and 70]. Investigations of the brittle failure of polycrystalline freshwater ice [70] indicate that ice generally exhibits negligible tensile ductility. The tensile strength of freshwater ice depends mainly on the grain size, only slightly on temperature, and was found to be independent of strain rate (Fig. 2.12). Freshwater ice under compression exhibits brittle behavior only at high strain rates (above 10^{-3} s^{-1}). When this occurs, its strength decreases with increasing temperature, strain rate (Fig. 2.13) and grain size. In the transition zone at intermediate strain rate values (between 10^{-5} and 10^{-3} s^{-1}), the compression failure of ice exhibits both brittle and plastic features (Fig. 2.14). It is reported that difficulties in making the measurements occur when the strength of ice is measured at high strain rates, but it is believed that the strength of ice does not decrease considerably at strain rates higher than 10^{-2} s^{-1} [19].

Petrovic [61] reviewed the mechanical properties of freshwater ice and summarized some characterizing values for its Young's modulus, Poisson's ratio, tensile strength and compressive strength. The Young's modulus and the Poisson's ratio of ice measured at a temperature of -10°C are reported to be in the range of 9.7-11.2 GPa and 0.29-0.32, respectively. The tensile and compressive strength of ice measured at temperatures between -10°C and -20°C are reported to vary in the range of 0.7-3.1 MPa and 5-25 MPa, respectively.

Characterization of the flexural properties of fine-grained (grain size: 1-5 mm) freshwater ice (S1 and S2) at low deformation rates [25, 72] indicates that the flexural strength (governed by tensile stresses) of ice is a function of the grain size, crystal structure and temperature but not a function of the loading rate. However, it is believed that the flexural strength of ice at high deformation rates is rate-dependent. Its strength increases with decreasing grain size and temperature. Average values of the flexural strength of freshwater ice are reported to be 2 ± 0.4 MPa.
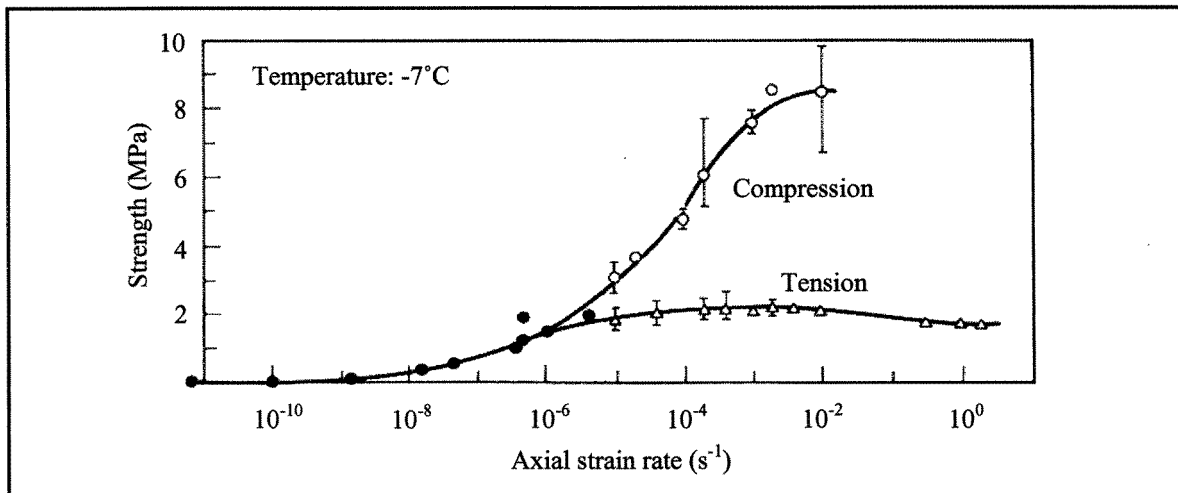
Figure 2.11 Tensile and compressive strength of ice versus strain rate (adapted from [19])
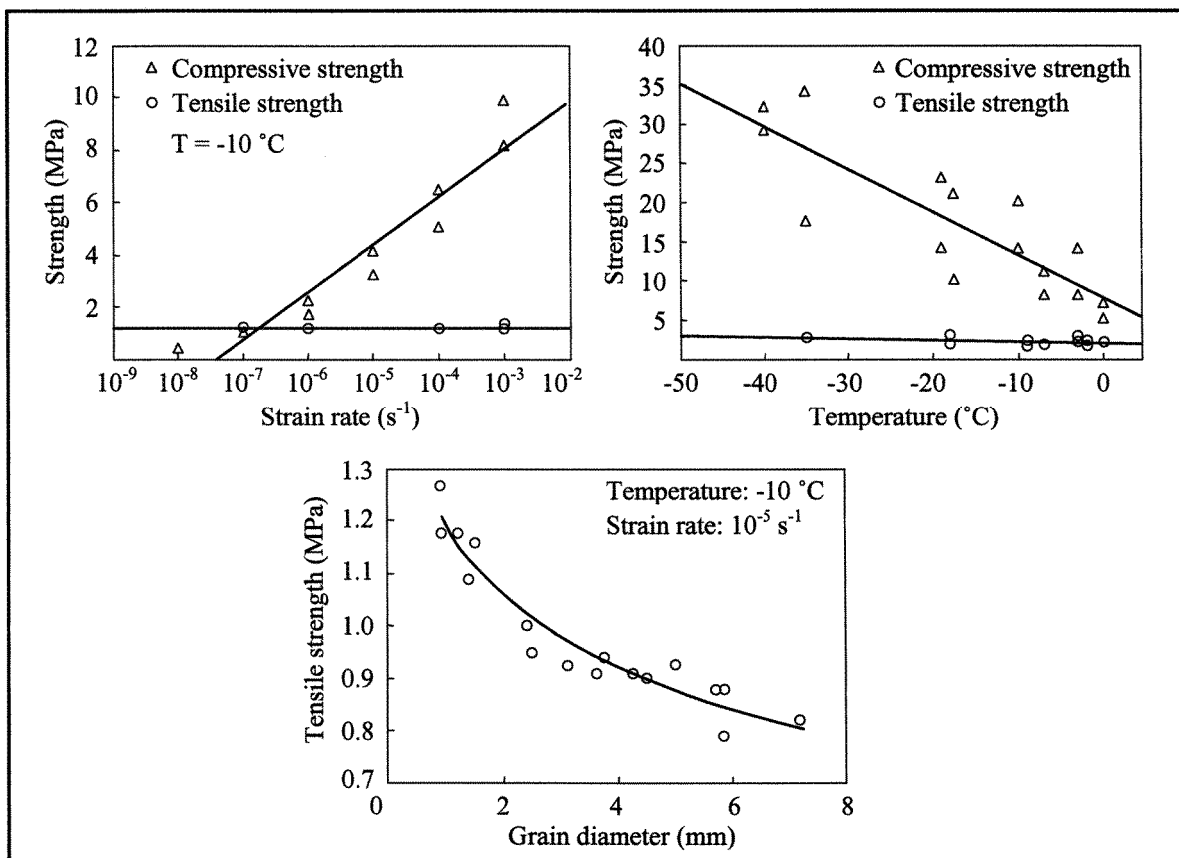
Figure 2.12 Tensile and compressive strength of ice in terms of strain rate, temperature and grain size (adapted from [61])
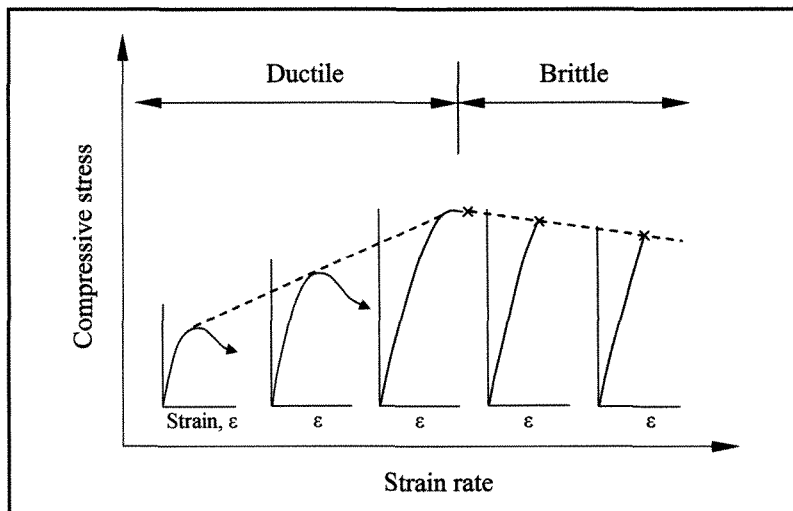
Figure 2.13 Schematic of the effect of strain rate on the compressive
stress-strain behavior of ice (adapted from [70])
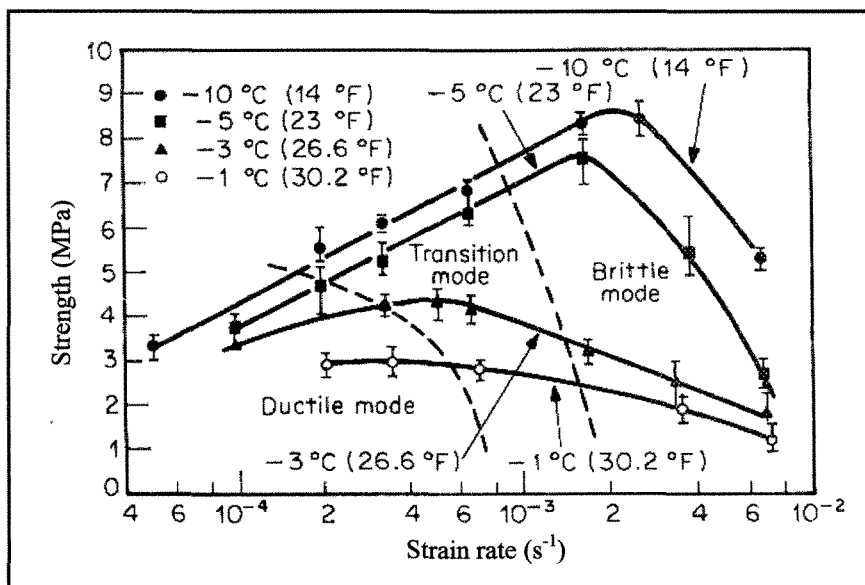
Figure 2.14 Compressive strength of fine-grained freshwater ice (S2)
versus strain rate at various temperatures (adapted from [19])

2.6 Numerical modeling of ice shedding

The first attempts to estimate rebound heights of conductors due to sudden ice release were made decades ago [56]. More recently, the improvement of computing tools and software has led to the finite element modeling of both static and dynamic effects of instantaneous ice shedding on overhead lines [32, 48, 66 and 67].

Jamaleddine *et al.* [32] studied the effect of ice shedding on overhead lines using Automatic Dynamic Incremental Nonlinear Analysis (ADINA), a commercial software package [2]. In their study, reduced-scale ice shedding simulations were also carried out experimentally by the sudden drop of dead weights. A comparison of the experimental and finite element model results confirmed the good performance of the numerical models for both static and transient dynamic analyses.

Following Jamaleddine's work, a numerical study of a two-span line section response to instantaneous shedding was undertaken by Roshan Fekr [66, 67]. In this study, several ice-shedding scenarios were analyzed with variables including ice thickness, span length, difference in elevation between end and suspension points, number of spans per line section, presence of unequal spans and partial ice shedding on sub-spans.

Matsuura *et al.* [48] carried out real-scale observations and analyses of ice shedding from power lines fully exposed to heavy atmospheric icing (6 kg/m). They measured the meteorological conditions, weight of the ice, the tension of insulator strings, and monitored the motion of the conductors. They also performed finite element analysis of the dynamic effects of sudden ice shedding from the line for a particular scenario observed. A detailed description of their numerical model is lacking, but they concluded that the numerical and

experimental results of the maximum cable jump were in general agreement and therefore numerical analysis of the ice shedding phenomenon by the finite element method could be useful for the design of transmission lines prone to severe atmospheric icing.

2.7 Summary

In this chapter, it was emphasized that the main loads applied to transmission line structures come from the cables they support. The most frequent external loads to which a line section is subjected during its service life are wind, and in cold regions prone to atmospheric icing, ice loads. It is well known that ice deposits on cables can be the source of several mechanical problems.

Ice can deposit on overhead transmission line cables and their supporting structures in different forms and densities. The types of atmospheric ice accretions that are significant for our purpose are heavy adherent wet snow, hard rime, large deposits of lightweight rime ice, and dense glaze ice. The latter is the focus of this study.

Therefore, in order to protect the line against loads resulting as a consequence of accreted ice on the line and to ensure the reliability of electric power delivery networks, various protection methods have been used. One category of these techniques directly deals with the root of the problem, such as to remove or prevent formation of ice accretion on overhead lines. In recent years, a total of 37 line de-icing and anti-icing techniques were reported, aiming at preventing power lines from getting damaged following severe atmospheric icing.

The de-icing techniques most widely and effectively used are based on ice melting

using the Joule effect. Several of these techniques have been developed worldwide for both energized conductors and ground wires. However, their application to ground wires has several serious drawbacks. Therefore, several methods aimed at de-icing overhead ground wires have been developed by Hydro-Québec TransÉnergie.

One of the developed techniques uses mechanical shocks to de-ice the ground wire by taking advantage of the brittle behavior of ice at high strain rates. The mechanical de-icing device is called DAC (De-icer Actuated by Cartridge) and is aimed at de-icing steel OHGWs and OPGWs one span at a time.

Numerical analysis studies of ice shedding on lines are scarce, and in most previous studies, the response of the line to instantaneous shedding was modeled. Actual observations of natural ice shedding on lines are also scarce, and the assumption of instantaneous random shedding on span fractions cannot be discarded especially when shedding is triggered by melting. However, experiments on mechanically-induced shedding show the progressive shedding of ice along the span as an "unzipping" effect. Therefore, further analysis of this phenomenon is still required to determine whether the extreme motions and damages that have been attributed to the sudden ice shedding are real or the by-product of galloping motions. As a result, in this study a numerical model considering the propagation of ice shedding along the span is proposed.

In order to model the propagation of ice shedding along the span and therefore to integrate the failure criteria of glaze ice into the model, knowledge of the mechanical properties of ice is essential. Ice is a very complex material and its mechanical properties depend on crystal structure, temperature, presence of impurities, and type, rate and

direction of loading. In short-term loading, ice behaves elastically and fails in a brittle manner. If the loading rate is low, creep and plastic failure predominate. In this study, the properties of ice associated with short-term loading are assumed to prevail.

In the case of mechanically-induced ice breaking by shock loads, the main properties that govern the failure of the accreted ice deposit on cables relate to the tensional (axial) and flexural strengths and rigidities of the iced section. On the basis of observations and numerical simulations, a simple model is suggested where the flexural properties of the ice deposit are mainly responsible for mechanical ice shedding. However, information about the mechanical properties of dense glaze ice under high strain rate (above 10^{-3} s^{-1}) is lacking to develop a more realistic model at this stage. Therefore, the mechanical properties of fine-grained freshwater ice are used for this study as the best information available.

Experimental analysis of ice shedding problems on a full-scale is difficult and costly to achieve. Therefore, it is envisioned that finite element models will provide a powerful simulation tool to assist in the management of mitigation for atmospheric icing on power lines.

CHAPTER 3

MODEL ELABORATION AND NUMERICAL RESULTS

3.1 Numerical modeling approach

3.1.1 Introduction

In this section, the general numerical modeling approach originally proposed in [49] for transient analysis of overhead transmission lines, enriched in the last decades by collaborators [32, 42, 52, 66 and 67], including our contributions [33, 34], is summarized. As in previous numerical studies [32, 42, 49, 52, 59, 66 and 67], ADINA [2] is used to simulate the dynamic effects of ice shedding induced by a pulse-type excitation on a level single-span section.

3.1.2 Cable modeling

The cable is assumed to be perfectly flexible in bending and torsion; therefore it is represented by 3-D two-node isoparametric truss elements using the total Lagrangian formulation with large displacement kinematics but small strains [2, 6]. Each cable element has four degrees-of-freedom corresponding to the horizontal and vertical translations at each end. The cable material properties are linear elastic tension-only, therefore allowing

slackening whenever the cable loses its pre-stressing force. In the models presented here, meshes with 0.2 m long cable elements were found to be adequate (Fig. 3.1). The initial tensile strain of the truss element is specified from a preliminary static analysis assuming an axially rigid catenary under its self-weight (Appendices A and D). The finite element mesh selection is based on the dynamic considerations discussed in Section 3.1.6.
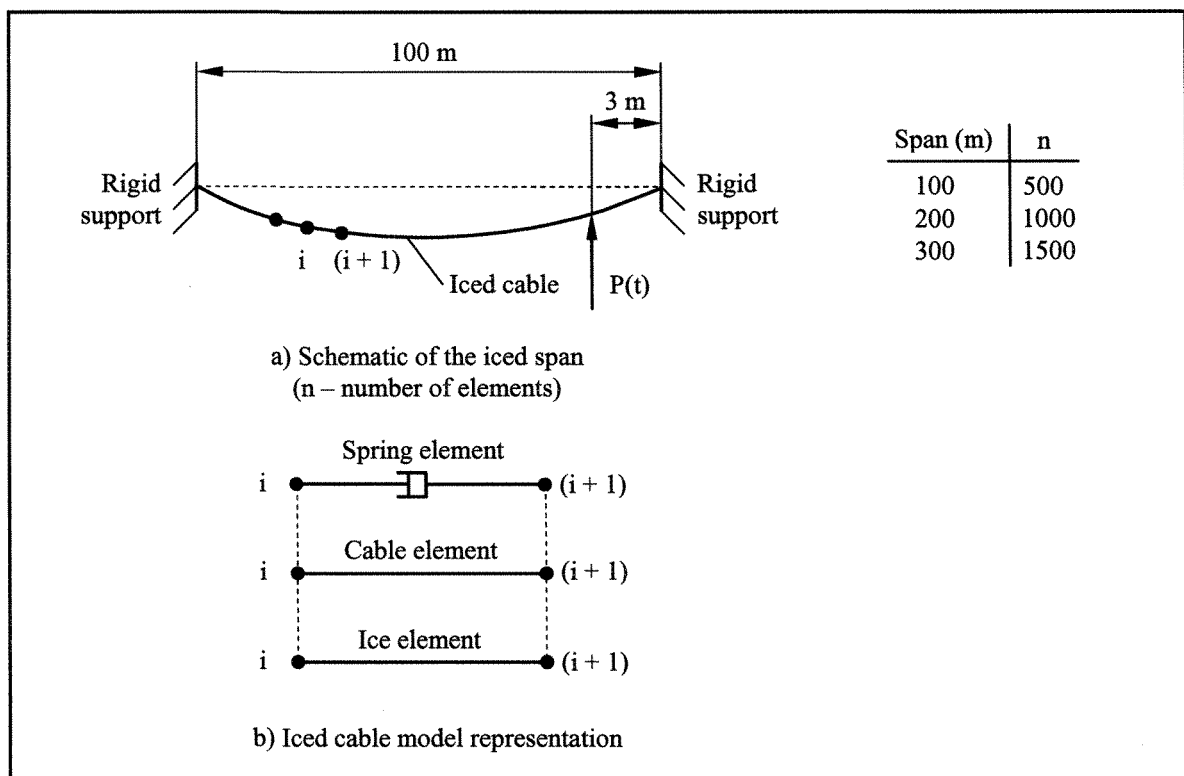
Figure 3.1 Iced cable modeling approach

3.1.3 Accreted ice modeling

Accreted ice on the cable is modeled as a separate beam element parallel to each cable element (Fig. 3.1b). It was found adequate to represent the accreted ice on the cable by the

3-D iso-beam element with post-elastic behavior. Each beam element has six degrees-of-freedom corresponding to the horizontal and vertical translations and the in-plane rotation. Since only rectangular cross sections can be considered for the materially nonlinear iso-beam element in ADINA, the cross-sectional parameters of the iso-beam ice deposit are specified to yield a bending rigidity equivalent to that of the idealized shape of accreted ice (Fig. 3.2). In order to avoid spurious stiffening of the system caused by fixed rotational boundary conditions at the supports, ice beam elements are omitted just next to the support nodes. It should be noted that alternative ice modeling approaches are also investigated using the 2-D plane stress iso-beam and pipe-beam elements as described in Section 3.1.8.
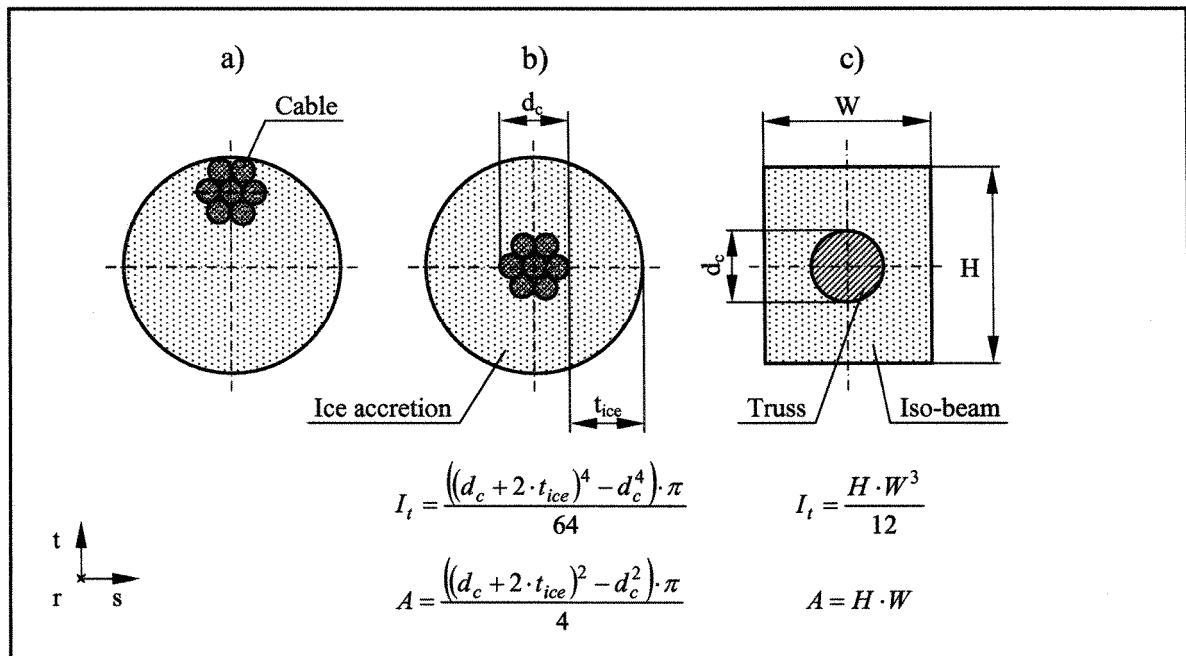
Figure 3.2 Ice accretion on a cable and its model representations
a) Artificial ice accretion on a cable; b) Idealized shape of accreted ice on a cable;
c) Iso-beam representation of accreted ice (equivalent bending rigidity and cross-sectional area)

3.1.4 Damping

In this study, based on satisfactory results of previous studies [32, 42, 52, 66 and 67], the aerodynamic damping is neglected and only axial structural damping of the iced cable is considered. Therefore, damping is modeled by using a non-linear axial spring element as a viscous discrete dashpot parallel to each cable element (Fig. 3.1b). The damping constant is determined from the critical axial viscous damping of a Hookean rod given in (3.1) [42] where C is the damping constant, ξ is the damping ratio, AE is the axial rigidity of the rod and m is its mass per unit length. The damping constant is set to represent an equivalent viscous damping of 2% critical [75].

$$C = 2\xi\sqrt{AEm} \tag{3.1}$$

Besides this viscous structural damping, algorithmic (numerical) damping is also used to filter out spurious high frequencies of the response due to finite element discretization. Numerical damping is introduced using the Newmark integration operator with parameters δ and α set to 0.55 and 0.3, respectively, relying on previous work [50]. Studies of the effects of different numerical integration parameters on the calculated dynamic response are also performed as summarized in Chapter 7.

3.1.5 Initial static equilibrium

In order to avoid the stiffening effect of the flexural rigidity of the ice element on the initial static profile, the deformed cable profile is calculated beforehand using an increased density cable model as in previous studies [32, 42, 52, 59, 66 and 67]. This deflected static

profile serves as the initial profile of the ice-cable composite model where the cable element is initially prestressed by setting the initial strain to the value obtained from static analysis of the increased density cable model.

3.1.6 Dynamic analysis

A restart option is available in ADINA to start the dynamic analysis from the initial static equilibrium profile obtained for the iced cable. Static analysis is completed in five load increments so that dynamic analysis is usually started at time $t = 5$ s. Since the exact time function of the shock load generated by DAC [43, 44] is confidential information with regard to the device's intellectual property, the shock load used in this study is simply defined by a triangular pulse-type excitation (Fig. 3.3), which is specified as a concentrated vertical upward force applied, at this stage of analysis, at 3 m from the span extremity (Fig. 3.1). The load is activated at time $t = 5$ s with the given triangular pulse functions. In order to investigate the effects of pulse-load characteristics on the dynamic response, the load is assigned different triangular pulse functions and at different locations on the span as discussed in Chapter 6. The selection of the time step and the mesh size is such as to provide adequate sampling of the shock wave as it travels through the cable finite element mesh [6, 42, 49, 52 and 59] (Appendix A).

3.1.7 Ice failure modeling

Ice failure and subsequent shedding or detachment is modeled using the *"element death upon rupture"* option available in ADINA. For the iso-beam ice element used with the plastic bilinear material model, the element death option is automatically activated when the rupture criterion is fulfilled at any given integration point of the element. The element is then considered as "dead" for the remainder of the analysis and its mass and stiffness contributions are removed from the model [2]. The ice material model is defined in ADINA by setting the Young's modulus to 10 GPa, the Poisson's ratio to 0.3, the density to 900 kg/m^3, the initial yield stress to 2 MPa, and the maximum allowable effective plastic strain to 10^{-10}.
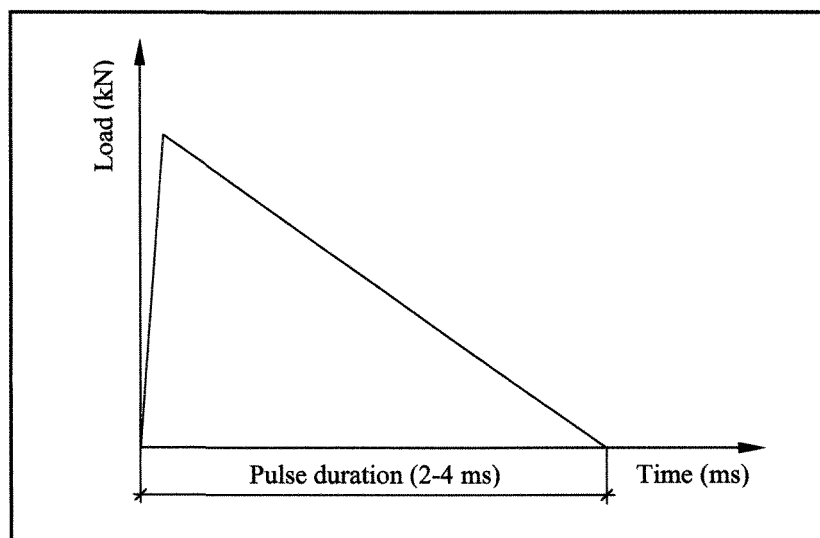
Figure 3.3 Triangular pulse-type excitation

3.1.8 Other considerations

A) Numerical considerations

For the calculation of all element matrices and vectors, numerical Gauss integration is used. As previously indicated, the Newmark direct implicit integration method is selected to solve the dynamic equilibrium equations, with the full Newton iteration method for stiffness updates. The convergence criterion is based on the energy, ETOL, and displacement tolerances, DTOL, of the system with ETOL = 1.0^{-7} and DTOL = 1.0^{-5}. A lumped mass formulation is used throughout [6].

B) Alternative ice modeling approaches

Two alternative modeling approaches were also found adequate to represent the accreted ice on the cable in ADINA. The use of the 2-D two-node plane stress iso-beam element parallel to each cable element tends to reduce the computational effort considerably for this simple single-span model since the numerical integration is only performed in two dimensions and the number of degrees-of-freedom is reduced [2]. However, as it is emphasized in Chapter 7, the application of this modeling approach was found to require careful analysis when partial ice shedding is predicted by the model. Another model representation of accreted ice on the cable entails the use of the pipe-beam element parallel to each cable element. In this model representation, the geometrical restrictions regarding the cross-sectional parameters of the iso-beam element, as described in Section 3.1.3, are not applied in ADINA, which represents a major advantage.

3.1.9 Modeling limitations

A) Towers and their foundations

Power transmission lines comprise four major components that are intricately interconnected: towers, foundations, cables, and interfaces such as insulators and other items of line hardware. The response of a line section to shock-load-induced ice shedding depends also on the interaction between all these components. Therefore, very accurate modeling of a line section subjected to shock loads may become complex. In addition, the work of Lapointe [42] related to cable rupture emphasized the importance of the 3-D modeling of the towers. It was found that the response time obtained by the 3-D models is significantly delayed in comparison to the 2-D models and the simplified 2-D models tended to overestimate (in the order of 10-30%) the tensions in the conductors at the supports adjacent to the broken span compared to the results obtained with the more realistic detailed 3-D models of the suspension towers. This study also indicated that the presence of intact wires is important as it reduces the maximum load amplitudes and the magnitude of the displacements calculated. Torsional displacements of the tower were also found non-negligible while the dynamic interaction between intact conductor spans and the suspension structures seemed negligible for relatively rigid classical towers. However, ground wires were found to affect the dynamic response of the line section.

Nevertheless, in this study, to start with a simple model, only a 2-D level single-span numerical model is defined in the vertical plane where neither the suspension structure nor the towers are considered. Therefore, the flexibility of the towers and their foundations is not modeled and the cable ends are assumed to be rigidly fixed.

B) Damping

In a typical line section – that is not equipped with any special damping devices – the source of damping mainly comes from the cables and their supporting structures. Damping of the cables may arise from internal/structural damping and aerodynamic damping. The internal damping is a complex combination of hysteretic damping within the individual cable strands and damping due to the sliding friction and contact between strands as they move past one another during cable movement. The internal damping can be further specified as axial damping that takes place due to changes in the cable tension, and transverse damping due to bending of the cable. Aerodynamic damping arises from the motion of the cable relative to the air.

Much of the research done on the damping of transmission conductors is related to the study of wind-induced vibrations (Aeolian vibrations and galloping). These studies often do not distinguish between the internal damping and the aerodynamic damping [59] but most of them conclude that aerodynamic damping plays an important role in the dynamic behavior of the cables [46, 55]. However, the influence of aerodynamic damping on the transient response of a line section still needs to be quantified [52] and is presumably small. In addition, in previous time history analyses of conductor motion [32, 42, 52, 66 and 67], it is stated that the effect of structural damping of the cable is not predominant in the first few seconds of the transient response when peak values are of interest. Damping mostly affects the free vibration behavior of the cable as it returns to rest. Nevertheless, introduction of damping in the model is beneficial to filter out spurious high frequencies of the response generated by the finite element discretization.

3.2 Numerical modeling results

3.2.1 Introduction

In this section, the numerical modeling results of one typical case with parameters adopted from [44] (Table 3.1) and the pulse-load defined in Figure 3.4 are presented in some details to illustrate the calculated dynamic response of iced cables subjected to mechanical shocks. At this stage of analysis, the shock load is defined as a concentrated vertical upward force applied on a ground wire (Appendix C) at 3 m from the span extremity (Fig. 3.1).

3.2.2 Eigenvalue analysis

It was found to be a good practice to conduct eigenvalue analysis on the line section studied prior to transient dynamic analysis since unrealistic natural frequencies or mode shapes are good troubleshooters. Therefore, several natural frequencies and mode shape analyses were conducted on various iced span models to validate and adjust the parameters of the mesh and to investigate alternate modeling approaches. In all cases, the cable was modeled with the pre-stressed truss elements while the ice deposit was represented either by the increased-density truss element, the Hermitian beam element, the iso-beam element or the pipe-beam element, respectively. The calculated in-plane mode shapes and corresponding natural frequencies were identical in all models and comparable to those obtained from Irvine's theory [31] (Appendices A and D) (Table 3.2). For the frequency of the first symmetric mode, the results of Irvine's theory and increased density truss are

identical and smaller than for the first three cases since these two iced cable models neglect

the stiffness contribution of the ice deposit itself. The simplification does not affect higher

frequencies.
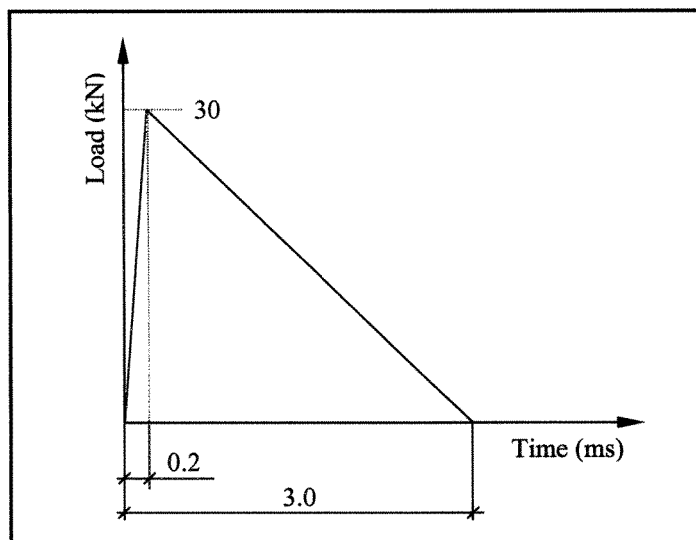
Figure 3.4 Pulse-load characteristics

Line parameters		Ice parameters	
Span length (m)	100	Type	Glaze
Initial horizontal tension (kN)	12.5	Density (kg/m^3)	900
Cable axial rigidity (kN)	16,636.6	Radial ice thickness (mm)	12.7

Table 3.1 Parameters of the case study

Mode	Truss Herm. - beam (Hz)	Truss Iso - beam (Hz)	Truss Pipe - beam (Hz)	Increased - density truss (Hz)	Irvine's theory (Hz)
1st symmetric	0.75	0.75	0.75	0.67	0.67
1st asymmetric	1.00	1.00	1.00	1.00	1.00
2nd symmetric	1.51	1.51	1.51	1.50	1.51
2nd asymmetric	1.99	1.99	1.99	2.00	2.00

Table 3.2 Natural frequencies of the corresponding 1st and 2nd in-plane modes obtained for different iced cable models (case study: Table 3.1)

3.2.3 Axial and bending effects in ice deposit

Transient dynamic analyses were performed in order to investigate the axial and bending responses of the ice deposit. At this stage of analysis, ice is modeled as a linear isotropic material to allow monitoring its axial and bending responses to pulse-loads without failure, so that the dynamic response of the fully iced span can be examined. Results obtained at ¼ of the span, depicted in Figure 3.5, show that both the axial (Fig. 3.5b) and bending (Fig. 3.5e) deformation rates calculated are large enough to assume ice mechanical properties at high strain rate. As expected, however, the bending effects (in terms of stress and strain rate) in the ice deposit are more significant than the axial effects and should, therefore, govern the failure. Bending strain rates and corresponding stresses and strains in the ice deposit (Fig. 3.5d, e and f) are large enough to likely cause ice failure in a brittle manner.
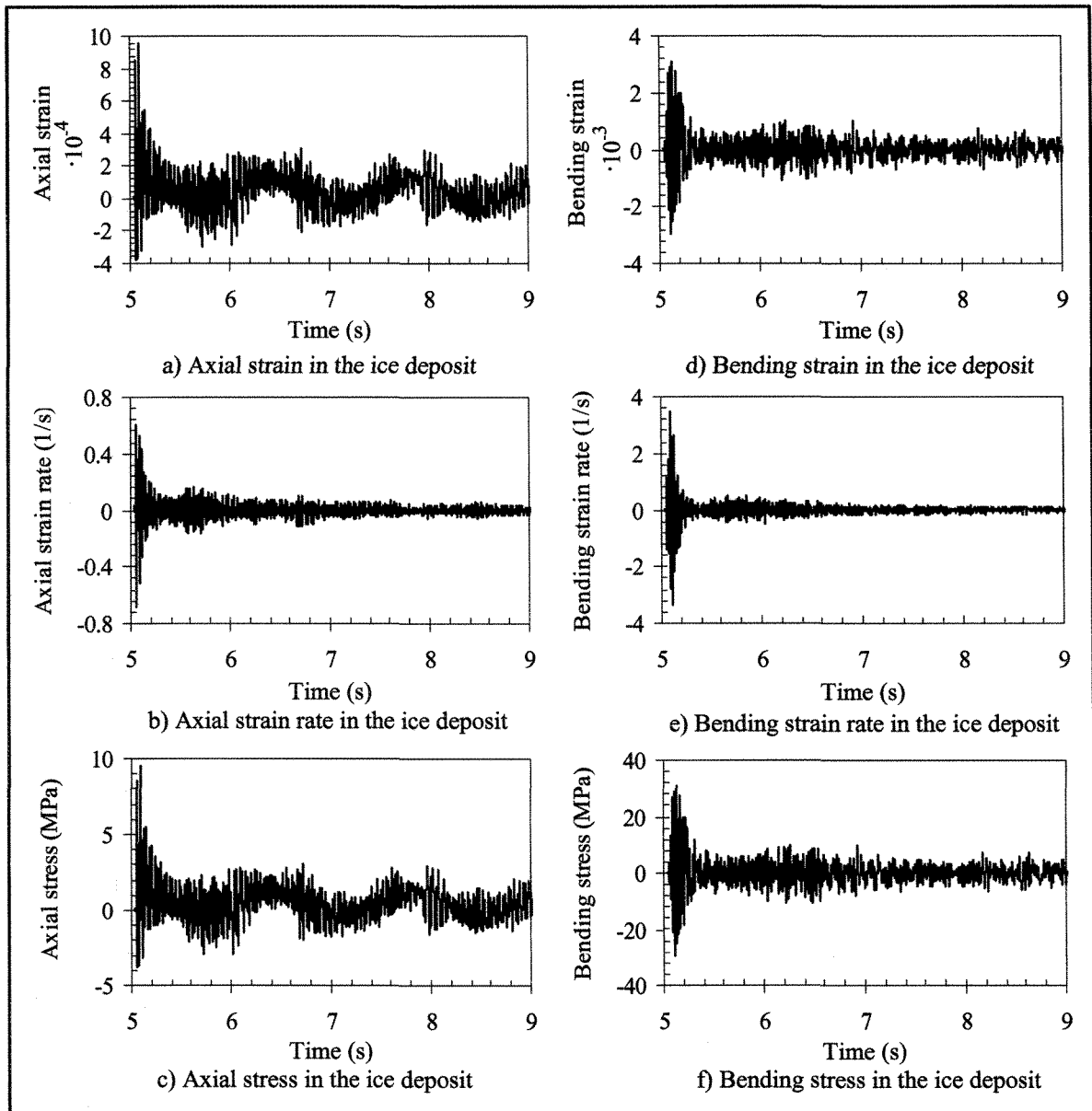
Figure 3.5 Axial and bending effects in the ice deposit under shock load at ¼ of the span

3.2.4 Ice-shedding analysis

A) Instantaneous ice shedding

It is useful to compare the dynamic characteristics of cable response due to progressive ice shedding along the span ("unzipping" effect) to those due to instantaneous ice shedding, and to validate our new iced cable modeling approach. To this end, instantaneous ice-shedding scenarios are analyzed using two modeling approaches with the parameters summarized in Table 3.1.

The first approach was successfully used in previous studies where ice shedding was simulated by the sudden decrease of cable density from static to dynamic analysis [32, 66 and 67]. In this study, ice shedding is modeled using the element death option available in ADINA for the ice beam elements at a specified time step. Results obtained for instantaneous ice shedding analyses using both approaches were found identical and as shown in Figure 3.6 where zero displacement refers to the initial, fully iced cable configuration.

B) Progressive ice shedding ("unzipping" effect)

The shock point load (Fig. 3.4) applied to the cable at 3 m from the span extremity (Fig. 3.1) generates a transverse wave in the ground wire that propagates along the span at an approximate average speed of 130 m/s. This transverse wave propagation causes significant bending of the ice deposit on the wire at high deformation speed and can break

up the ice (Fig 2.9). The wave propagation speed is obtained from the time histories generated (Fig. 3.7) and is in good agreement with the theory described in Appendix A.

Time histories of the vertical displacement of the overhead ground wire were recorded at three different points along the span: at the excitation point (Fig. 3.7a), at a point 2 m from the other span extremity (Fig. 3.7b) and at the mid span (Fig. 3.7c). The mid-span displacement (Fig. 3.7c) is clearly dominated by low-frequency (evaluated at about 0.7 Hz) oscillations combined with smaller amplitude higher frequency content (evaluated at about 10 Hz). The latter is more pronounced for vertical displacements near the fixed support (Fig. 3.7b). As expected, the shock load generates additional cable tension and the frequency content of the signature is higher than for transverse displacements (Fig. 3.8). The numerically-generated high frequency content of the response is partly filtered out by the numerical integration operator. However, high frequency oscillations are still present, which correspond to the fundamental longitudinal (axial) vibration of the iced cable (evaluated at about 18 Hz) (Appendix A).

a) Vertical displacement at the mid span due to instantaneous full-span ice shedding

b) Cable tension at the support due to instantaneous full-span ice shedding
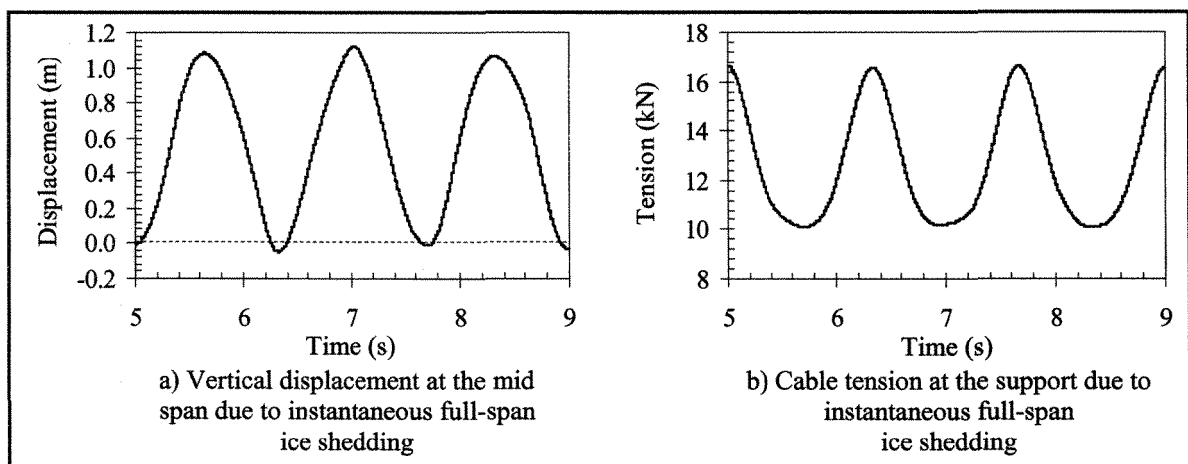
Figure 3.6 Transient dynamic wire response to instantaneous full-span ice shedding (no concentrated shock load is applied)
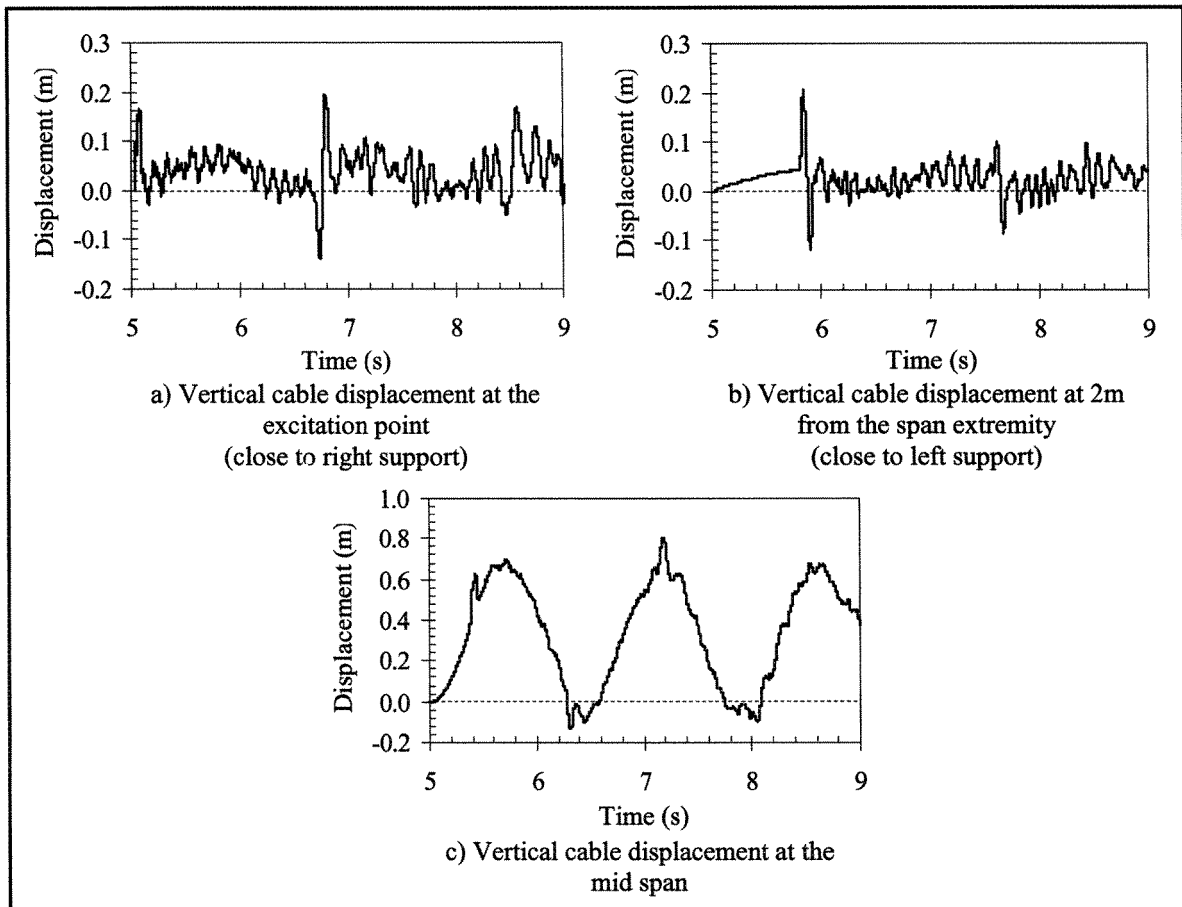
Figure 3.7 Vertical displacement of the overhead ground wire
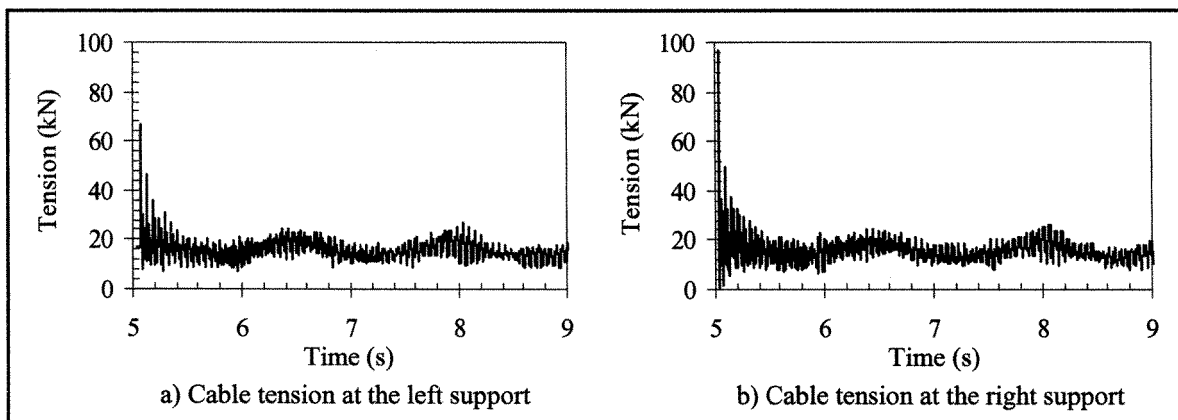
Figure 3.8 Cable tension at the supports

As expected, numerical results indicate that the maximum cable jump at the mid span obtained for the instantaneous ice shedding simulation is higher than that when progressive ice shedding takes place (c.f. Fig. 3.6a and Fig 3.7c). The impact is not as strong in the case of progressive shedding since the time needed to achieve full-span unloading can reach several seconds. However, the characteristics of cable tension are significantly dominated by the intensity of the shock load (Fig. 3.8), especially in the transient phase, whereas instantaneous shedding causes essentially free vibrations (Fig. 3.6b).

CHAPTER 4

EXPERIMENTAL STUDY

4.1 Introduction

In this chapter, considering the lack of availability of a real-scale test line, a level single-span reduced-scale experimental model is proposed in order to validate the numerical model presented in Chapter 3. Despite the certitude that no direct correlation can be made between reduced-scale and real-scale lines due to high nonlinearities of the problem and the exaggerated sensitivities of the reduced-scale model, it is believed that the reduced-scale model can serve to analyze and better understand the problem. It is also believed that if the numerical results of the level single-span reduced-scale experimental model are in good agreement with those obtained experimentally, the numerical model can likely be used to simulations of real-scale lines as well.

4.2 Experimental setup

4.2.1 General

The experimental setup consists of two rigid supports mounting a flexible stainless steel cable (Appendix C) pin-ended to load cells (Appendix E). The shock load (impact) is provided by a pneumatic cylinder (pneumatic shock load generator) (Appendix F) installed

at the cable mid span. A force sensor to measure the shock load is mounted on the tip of the pneumatic cylinder piston rod. A high speed digital camera is used to capture the cable mid-span displacement. The data acquisition system (Appendix G) also pertains to the setup.

4.2.2 Icing precipitation simulation laboratory

The experimental setup is installed at the CIGELE icing precipitation simulation laboratory. This laboratory is housed in a refrigerated room where the air temperature is controlled and can reach -20 °C. Six equally spaced (50 cm) air atomizing nozzles [15] manufactured by Spray System Co. (Fig. 4.1) incorporating a stainless steel water cap (No. 2050) and a stainless steel air cap (No. 67147) are installed onto an oscillating frame in front of a honeycomb duct (290x15 cm^2) (Fig. 4.2). The horizontal oscillating motion of the frame, i.e. the motion of the air atomizing nozzles, is provided by a gear motor with adjustable speed (0-30 rpm). This sway motion of the nozzles provides a more uniform precipitation distribution. Six fans of 315 mm blade diameter with speed control (0-3400 rpm) are installed behind the honeycomb duct. Each spray nozzle is installed with a heating coil and attached to the central air and water system as shown in Figure 4.3. The inlet water is locally pre-cooled to 1 °C by a mobile condensing unit.
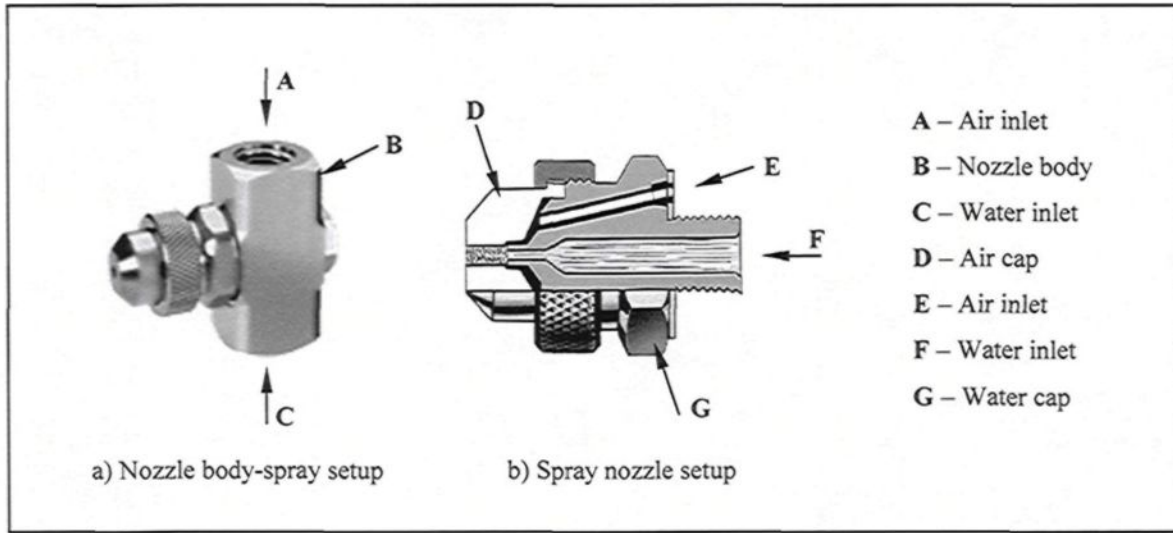
Figure 4.1 Air atomizing nozzle (model 1/4J-SS-SU11-SS) (adapted from Spray System Co.)

4.2.3 Level single-span reduced-scale conductor model

The level single-span reduced-scale conductor model comprises two electrical post insulators that serve as rigid supports and a flexible stainless steel cable pin-ended to four load cells (Appendix E). The post insulators are fixed to the ground at a distance 4.45 m from each other and 2.15 m from the spray nozzles (Fig. 4.4). The four load cells are mounted to the flat and perpendicular surfaces of two rigid steel frames in the horizontal and vertical planes (Fig. 4.5). These steel frames are installed face to face at the top of the insulators. The horizontal position of the frames can be adjusted in order to extend the span length to 4 m. The center of the span is aligned with the center of the honeycomb duct. The length and the position of the span were chosen after considering the limitation of the spray distribution zone and the refrigerated room configuration.

Two RR-W-410D flexible stainless steel cables (Appendix C) were used during the experimental study. Their length was defined to provide an initial sag-to-span ratio of 6% by keeping the span length at 4 m. The stainless steel cable is pin-ended to the load cells using hinged arms as depicted in Figure 4.5. In order to avoid plays at the pin joints and to reduce localized frictional damping, ball bearings are used to assemble the arms.

A – Oscillating frame   B – Fan
C – Stainless steel cable   D – Gear motor
E – Honeycomb meshes   F – Spray nozzle
G – Nozzle heating coil

a) Bottom view showing two nozzles

b) Spray nozzle with heating (detail H)

c) Side view

d) Front view showing six nozzles
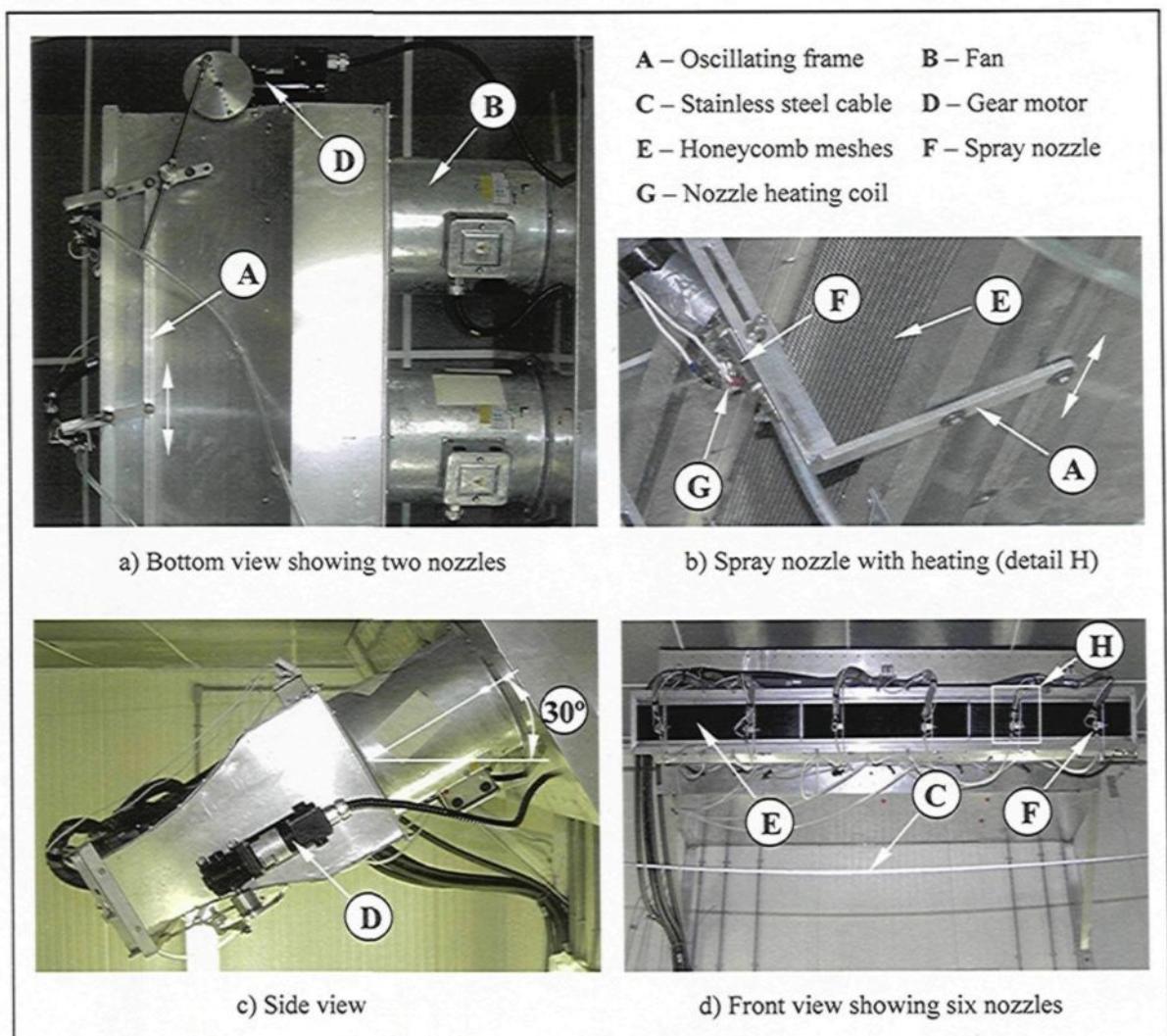
Figure 4.2 Honeycomb duct water spraying unit
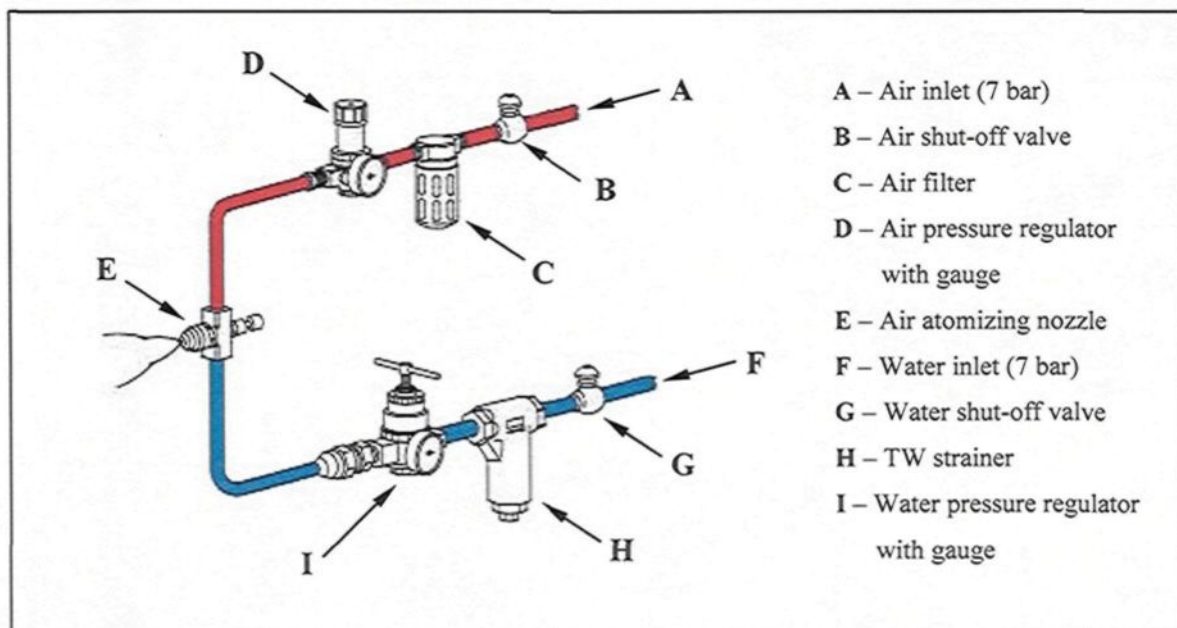
Figure 4.3 Schematic of the spraying system (adapted from Spray System Co.)

A – Air inlet (7 bar)
B – Air shut-off valve
C – Air filter
D – Air pressure regulator
with gauge
E – Air atomizing nozzle
F – Water inlet (7 bar)
G – Water shut-off valve
H – TW strainer
I – Water pressure regulator
with gauge
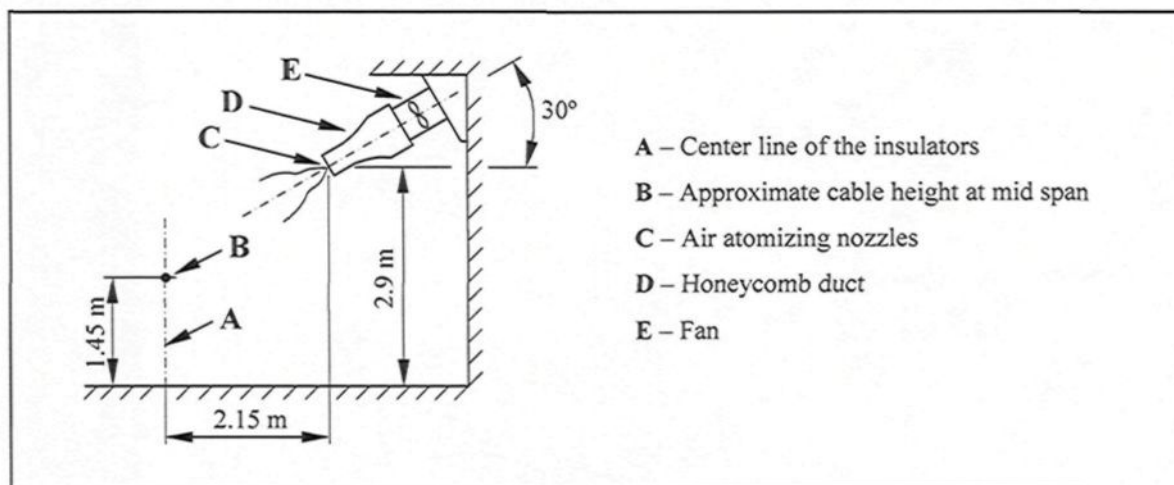
Figure 4.4 Schematic of the level single-span reduced-scale model configuration

A – Center line of the insulators
B – Approximate cable height at mid span
C – Air atomizing nozzles
D – Honeycomb duct
E – Fan

30°
2.9 m
1.45 m
2.15 m
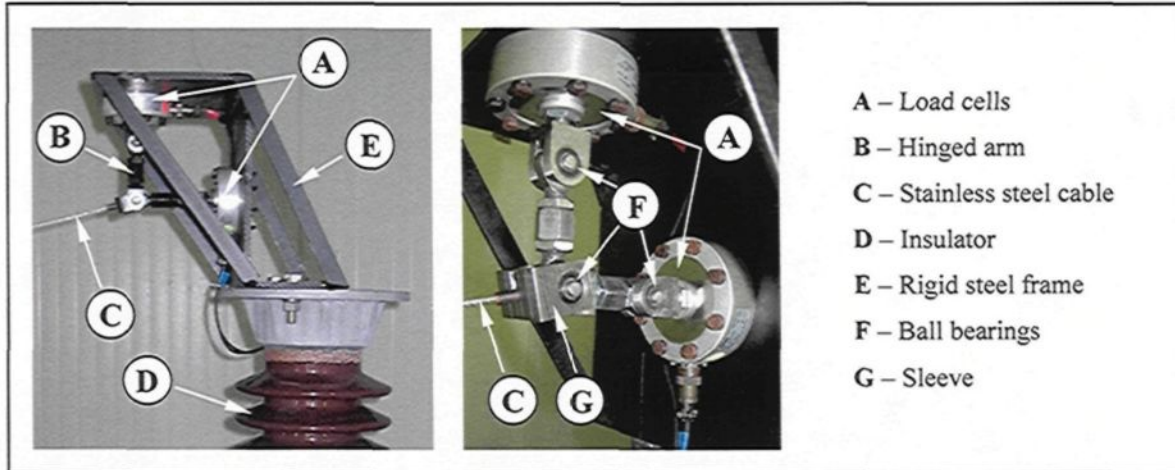
Figure 4.5 Pin-ended stainless steel cable end connection

A – Load cells
B – Hinged arm
C – Stainless steel cable
D – Insulator
E – Rigid steel frame
F – Ball bearings
G – Sleeve

4.2.4 Shock load generator

The shock load generator consists of an air cylinder (Parker series 2A) installed to a vertically adjustable lifting stage at the cable mid span (Fig. 4.6a). A urethane bumper is installed above the cylinder piston in order to reduce unwanted loads on the steel head at the time of impact (Fig. 4.6b). Furthermore, the piston rod stud that mounts the piston is also reinforced in order to improve its bearing capacity.

The shock load generator is part of a pneumatic system described in Appendix F. In order to provide accurate and stable air supply, an air tank (6) manufactured by Hoosier Tank Inc. is installed close to the setup in the refrigerated room. The air pressure is controlled by a filter-regulator unit (7) equipped with a gauge and installed to the connection point of the central air system outside the refrigerated room. Quick actuation of the shock load generator is provided by a normally closed high speed inline poppet valve (9). The air cylinder (1) is equipped with a quick exhaust valve (2) in order to provide

rapid exhaust of control air. A normally open air control valve (4) that serves to return the piston rod after the impact (shock load) is connected to the quick exhaust valve. In order to allow manual operation of the cylinder (e.g. position adjustment), the system is equipped with by-pass ball control valves. The shock load generator is actuated using a control panel that comprises a push button in series with the solenoid of the high speed inline poppet valve and that of the air control valve. Despite the air filter which is supposed to provide water-free air in the system, in order to avoid malfunction of the shock load generator in harsh cold conditions, the air temperature in the pneumatic system is maintained above the freezing point by using a cartridge type air heater and an automatic pipe heating cable. The cartridge type air heater manufactured by Watlow is installed into the air tank with a thermostat. The automatic pipe heating cable is used around the cylinder and the high speed inline poppet valve (Fig. 4.7). Therefore, all the system is covered by insulating material.

a) Lifting stage before system assembly   b) Cylinder assembly

A – Air cylinder
B – Lifting stage
C – Rigid base fixed to the ground
D – Jack
E – Handle
F – Piston rod
G – Steel head
H – Urethane bumper
I – Piston
J – Cylinder body
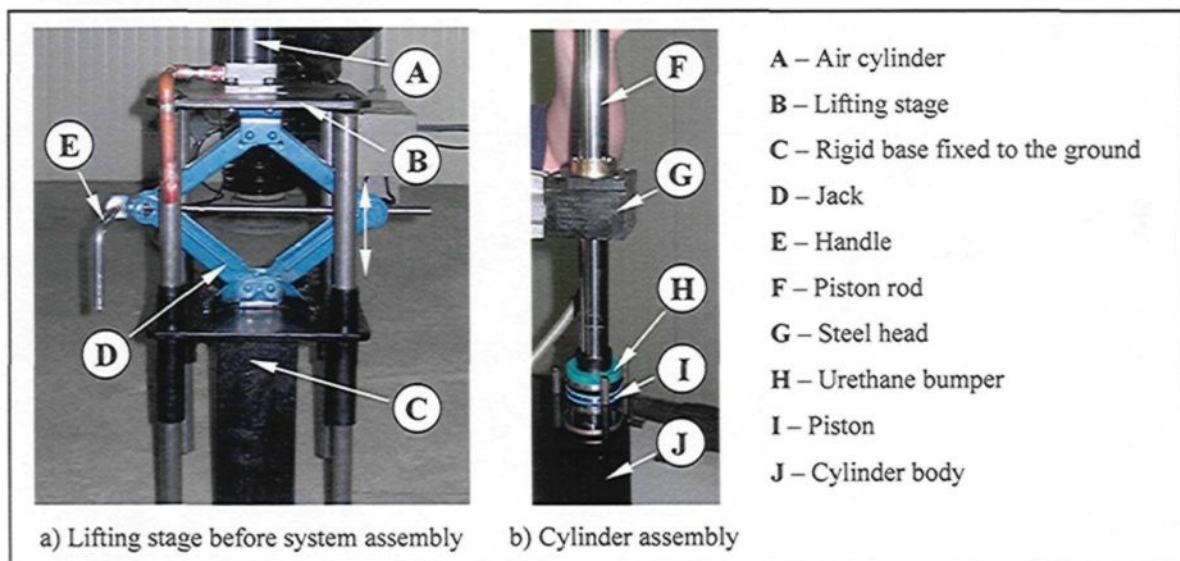
Figure 4.6 Air cylinder installation
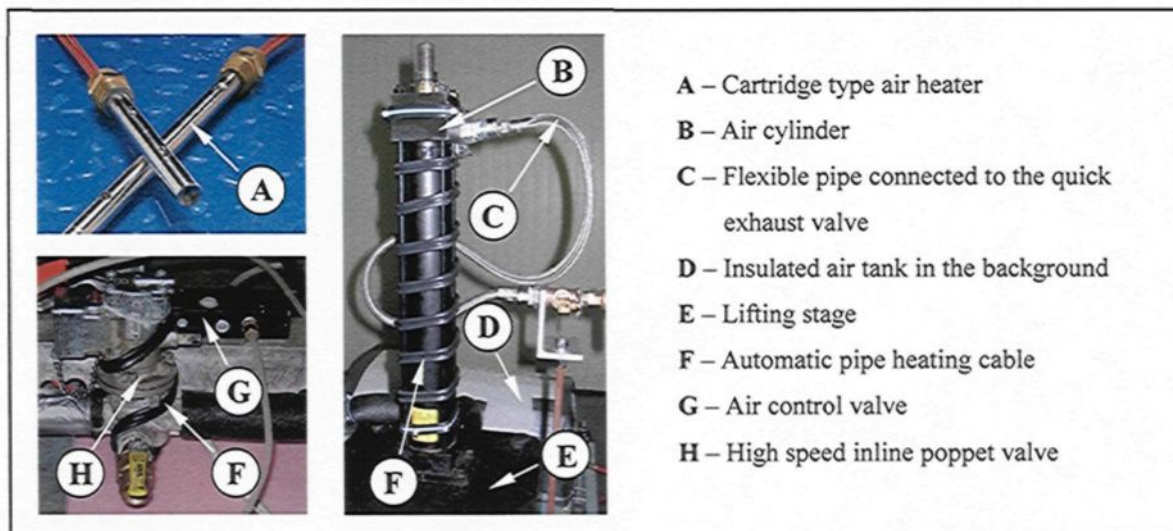
Figure 4.7 Heating of the pneumatic system without insulating covers (source A: Watlow)

4.2.5 Measuring devices and data acquisition system

Horizontal and vertical components of the stainless steel cable end-tensions are measured using low profile universal pancake load cells manufactured by FUTEK (model: LCF 450). This model uses metal foil strain gauge technology [4]. The load cells are designed for both tension and compression applications and have a capacity of 2,224 N (500 lbf) each. They have a rated output of 2 mV/V nominal, a nonlinearity of ±0.1% of the rated output, an operating temperature of -50°C to 93°C, and deflection of 0.05 mm to 0.13 mm nominal. Four load cells are installed to the rigid frames as already indicated (Fig. 4.5). The bridge excitation of 10 VDC for each load cell is provided by a signal conditioner amplifier manufactured also by FUTEK (model: CSG110). It has a built-in regulated bridge excitation source that requires a power supply at the range of 12 to 24 VDC @ 100 mA. It provides a voltage output of ±10 VDC at ±2 mV/V (Fig. 4.8a). The

four signal conditioners are installed outside of the refrigerated room and, therefore, the

signals are driven on 12 m shielded conductors, respectively, as shown in Appendix G.

Calibration of the measuring system is performed in compression.
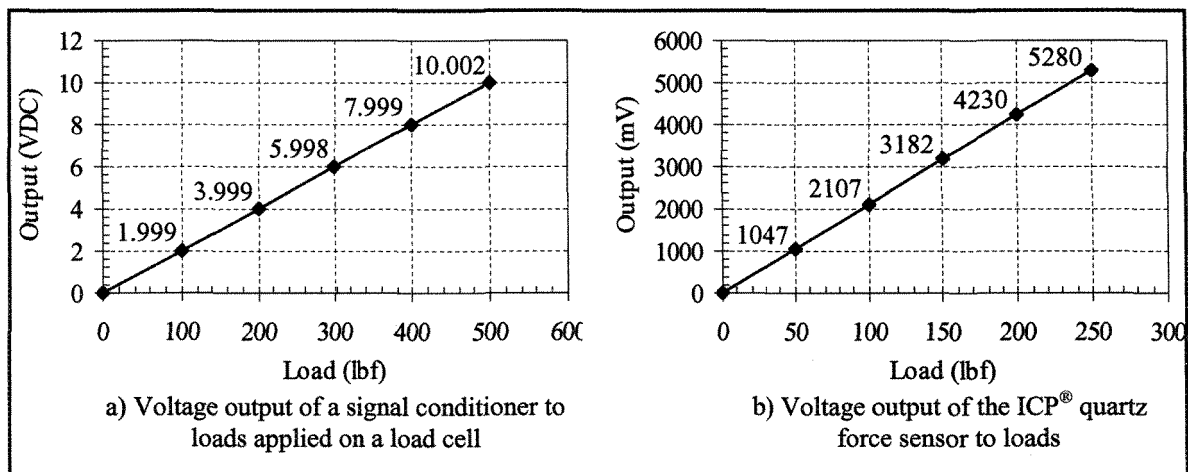
Figure 4.8 Voltage output of measuring devices

The shock load is measured by an ICP® low-impedance quartz force sensor manufactured

by PCB Piezotronics Inc. (model: N223M11). ICP® force sensors incorporate a built-in

MOSFET microelectronic amplifier that serves to convert the high-impedance charge

output into a low-impedance voltage signal for analysis or recording [4, 57]. This sensor

has a measuring capacity of 1,112 N (250 lbf). However, it is designed for high range

applications and therefore endures a load of 70 kN in compression and 20 kN in tension. It

has a sensitivity of 4.752 mV/N, an operating temperature range of -54°C to 121°C, and an

upper frequency limit of 10 kHz. It provides a voltage output as depicted in Figure 4.8b.

The sensor is mounted with a torque of 10 N·m to a flat aluminum stud installed to the end

of the piston rod (Fig. 4.9). An impact cap with a spherical surface to direct the force toward the middle of the sensor is used. Power to operate the sensor is in the form of a low cost, 25 to 27 VDC, 2 to 20 mA constant current supply provided by a signal conditioner manufactured also by PCB Piezotronics Inc. (model: 482A22). It is installed outside of the refrigerated room and, therefore, the sensor operates over an 8 m ordinary coaxial cable. However, the cable connected to the sensor is exposed to a high rate of deformations during operation. Therefore, a short (1.5 m) and light-weight coaxial sensor cable with a 90° microdot connector (10-32) manufactured by PCB Piezotronics Inc. (model: 018AK005EB) is used in order to add strain relief to the cable (Fig. 4.9).

A – ICP® quartz force sensor
B – Mounting stud
C – Piston rod
D – Impact cap with spherical surface
E – 90° microdot connector
F – Light-weight sensor cable
G – Insulator covered air cylinder
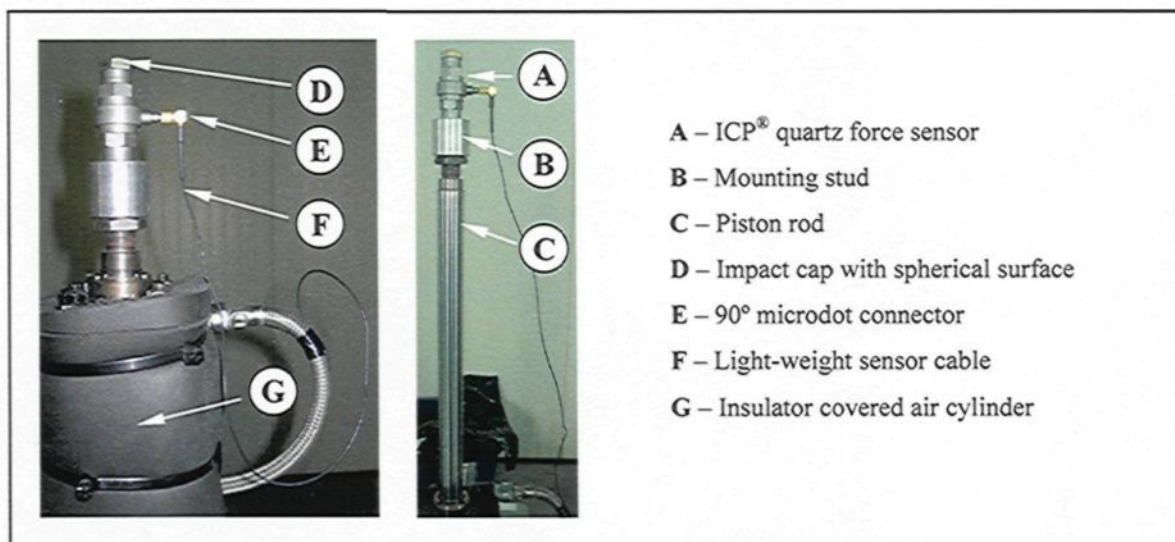
Figure 4.9 ICP® quartz force sensor installation

Analog to digital conversion is provided by a USB function module manufactured by Data Translation Inc. (model: DT9804). This module offers 16 single-ended or 8 differential

inputs with 16-bit resolution, up to 100 kS/s throughput, 16 digital I/O lines and 2 user counter/timers, and optional 16-bit analog outputs. The module is installed outside of the refrigerated room and connected to a computer through a Universal Serial Bus (USB) port. The five analog input signals are connected to the module using differential configuration [4] (Fig. 4.10). A bias return path for the five differential channels is provided through the software by adding a 10 kΩ of termination resistance from the low side of the channel to the isolated analog ground. A measurement application is built using a commercial test and measurement application software called DT Measure Foundry [11]. Schematic of the instrumentation wiring diagram is found in Appendix G.
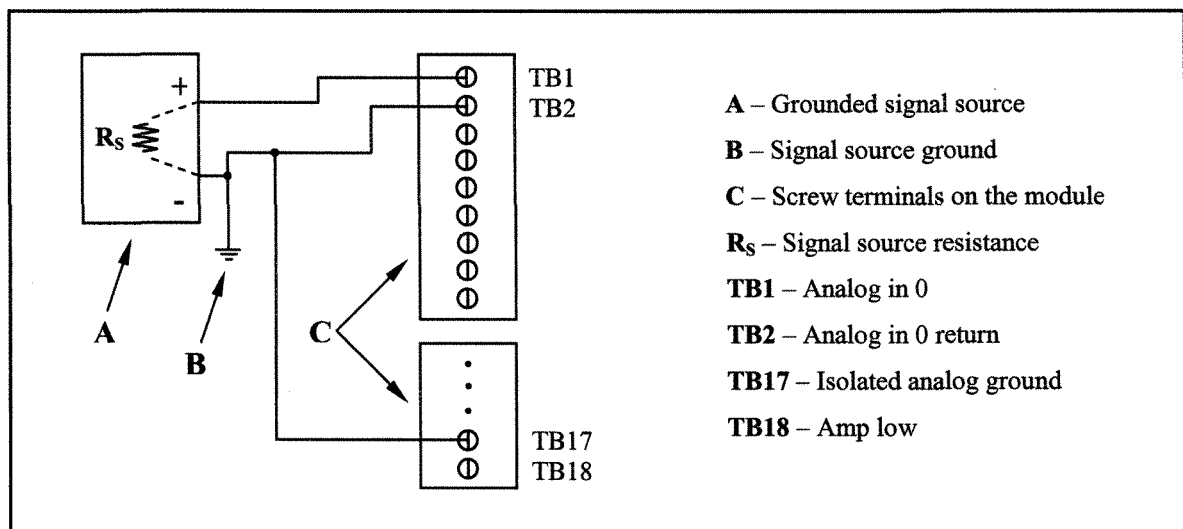
Figure 4.10 Schematic of the differential voltage input connection to the DT9804 module

A high speed digital camera manufactured by Kodak (model: EktaPro 1012) is used to capture the mid-span displacement of the stainless steel cable. There are two separate units

that make up the EktaPro: the camera and the processor. The processor is where the processing and timing take place and where the digital frames are stored. The camera is connected to the processor using a 4.5 m (15 ft) cable. A portable keypad allows the user to direct commands to the processor. The variables that can be controlled via the keypad are frame rate, exposure time (normally 1/frame rate), just to name a few. The frame rate of a camera is the number of frames recorded per second. In full-frame mode (239 x 192) the maximum frame rate of the EktaPro is 1000 fps that allows 3.2 s of recording time.

4.3 Description of a typical test

A typical test sequence comprises four major steps: (1) producing glaze deposit on the suspended stainless steel cable; (2) applying a shock load to the iced cable by actuating the shock load generator; (3) measuring and recording the characteristics of the shock load, the generated dynamic cable end-tensions and the cable mid-span displacement; and the (4) data processing.

The spraying system needs to be cleaned every time before starting the refrigeration of the room in order to avoid malfunction of the system caused by frozen left-overs. This procedure comprises the cleaning of the spray nozzles and pipes that connect them to the water and air supply. Heating of the spray nozzles and that of the pneumatic shock load generator system is turned on simultaneously with the refrigeration system. The spraying system (i.e. the precipitation) is put in action when the desired room temperature is reached. Experimental parameters that define the type and properties of ice [63] are

controlled as described in Appendix B in order to obtain a uniform icicle-free glaze deposit

with a density close to 900 kg/m^3 and to reduce the time needed for the ice formation. The

ice thickness of the ice accretion on the cable is continuously monitored visually and

indirectly by the measurement of the horizontal and vertical components of cable end-

tensions during the precipitation. When the desired ice thickness is reached the spraying

system is turned off and the vertical position of the shock load generator is adjusted by

manually lifting or lowering the lifting stage. The position of the shock load generator is

set to obtain a shock load duration of 2 to 4 ms. Based on experiments, this condition is

provided at the given air pressure when the impact cap of the ICP$^®$ force sensor at the

upper dead center of the air cylinder is positioned at 15 to 20 mm above the iced cable

level. The air pressure defines the speed of the piston rod (i.e. the characteristics of the

shock load) as shown in Appendix B. Our objective is to obtain the highest shock load

possible and therefore, the air pressure is set to 4 to 6 bar, for safety reasons. However, an

empirical expression for these interconnected parameters cannot be sharply defined since

the shock load characteristics are influenced by several uncontrollable factors that change

from one test to another such as the reflex of the operator (i.e. the release of push button on

the shock load generator control panel), the correctness of impact, the mass of impacting

objects etc. Recording of the shock load and the cable end-tensions by the measurement

application program and that of the cable mid-span displacement by the high speed digital

camera is started right before actuating the shock load generator since the recording time

allowed by the camera using 1000 fps in full-frame mode is limited to only 3.2 s as already

indicated. The shock load generator is actuated by the push button found on its control

panel. By pushing this button, the high speed inline poppet valve opens and for a fraction of a second the air control valve closes allowing the piston rod to impact the iced cable. By releasing the button, the high speed inline poppet valve closes and the air control valve opens providing the return of the piston rod right after the impact. Finally, the results are documented and the entire system is turned off.

4.4 Typical test results

In this section, characteristics of the measured parameters such as the shock load, the horizontal and vertical components of cable end-tensions and the cable mid-span displacement are presented and analyzed. However, it should be noted that the presented graphs are selected from different tests and one not necessarily corresponds to another. They serve only to interpret the characteristics of measured parameters in general.

4.4.1 Shock load characteristics

Figure 4.11 shows a typical dynamic force characteristics measured by the ICP$^{®}$ force sensor during a test. Recording of data is started at t = 0 s. However, the shock load generator is actuated only after the first second. Visual analysis of the cable mid-span displacement recorded by the high speed digital camera also served to analyze the dynamic force characteristics measured by the ICP$^{®}$ force sensor. The full spectrum of the force measured (Fig. 4.11a) shows a peak tensile force (point A: -2.1 kN) derived from the sudden deceleration of the piston rod at the upper dead center. It also indicates the path of the piston rod towards its lower dead center (point B) after the impact. The cable impact

takes place between points C and D right before the high peak of deceleration force (Figs. 4.11b and c). Therefore, the net shock load characteristic is considered as shown in Figure 4.11d. However, this analysis also indicates that the highest load the ICP® force sensor and the shock load generator must endure derives from the sudden deceleration of the piston rod at the upper dead center. This observation has led to the reinforcement of the air cylinder as described in Section 4.2.4.
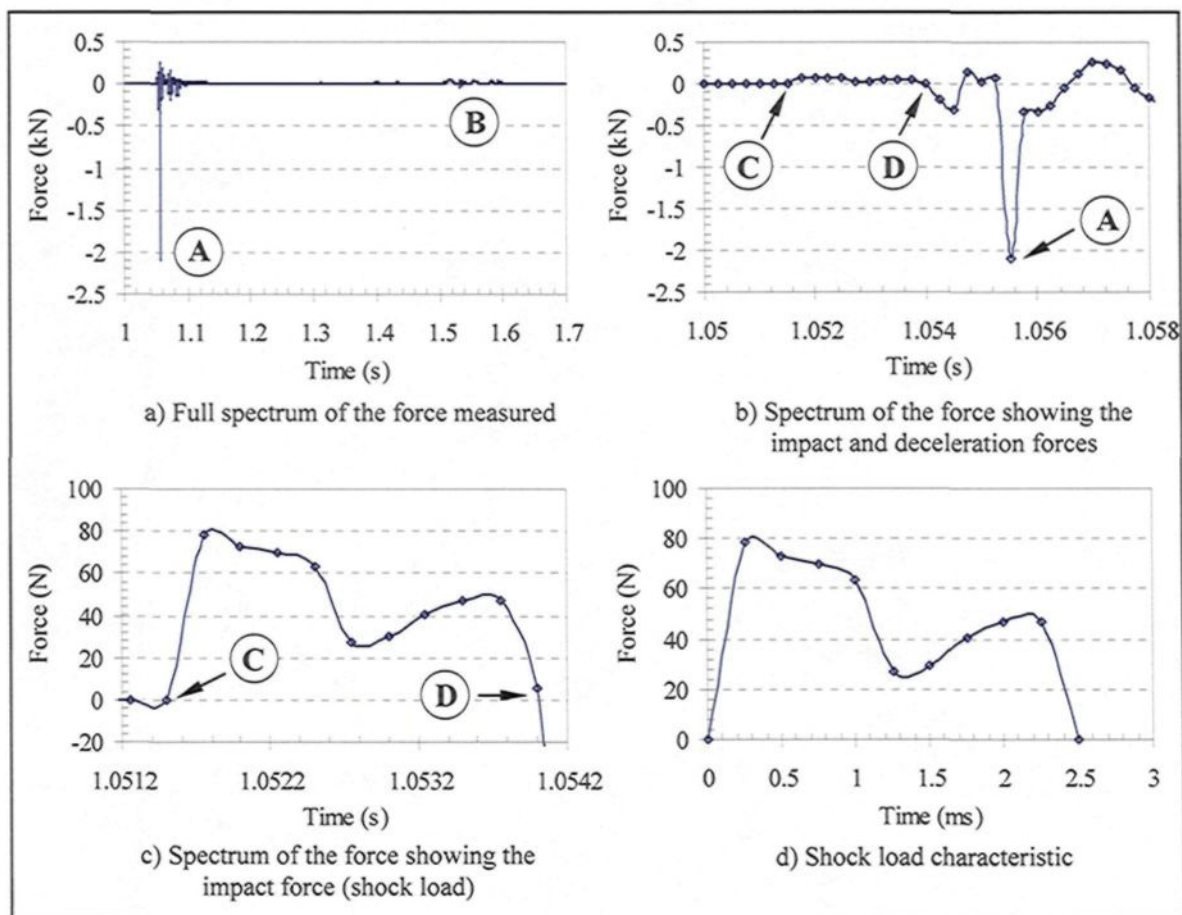
Figure 4.11 Dynamic force characteristics measured by the ICP® force sensor
(A – piston rod at the upper dead center; B – piston rod at the lower dead center;
C – beginning of the cable impact; D – end of the cable impact)

4.4.2 Time history of cable end-tensions

Horizontal (Fig. 4.12a) and vertical (Fig. 4.12b) components of the dynamic cable end-tensions generated by the shock load depicted in Figure 4.11 are measured using the load cells as described in Section 4.2. The resultant cable end-tension (T_R) shown in Figure 4.13 is calculated using

$$T_R = \sqrt{T_V^2 + T_H^2} \tag{4.1}$$

where T_V and T_H are the vertical and horizontal components of the cable end-tensions, respectively. Results show that the maximum cable tension measured occurs right after the shock load takes place.

a) Horizontal component of cable end-tension

b) Vertical component of cable end-tension
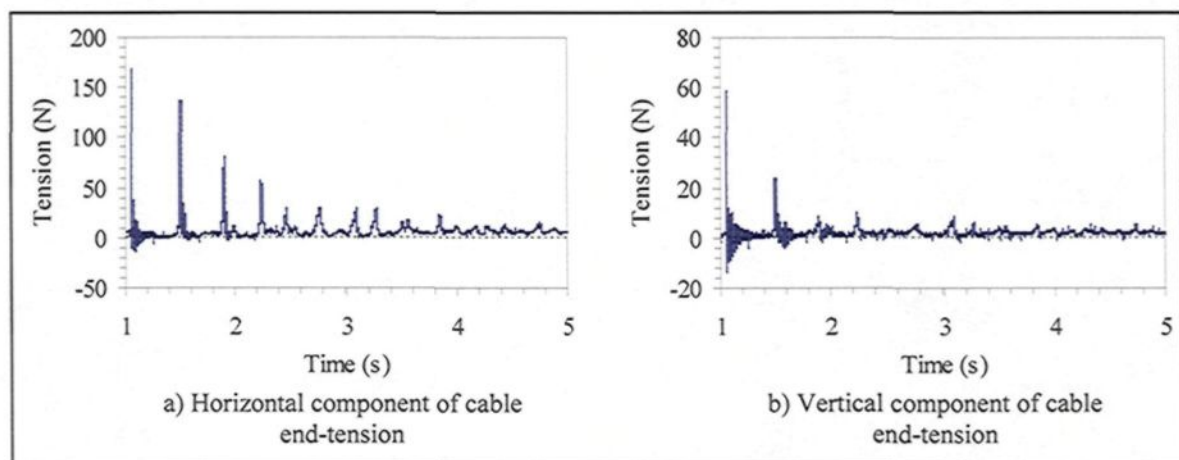
Figure 4.12 Time histories of the horizontal and vertical components of cable end-tensions
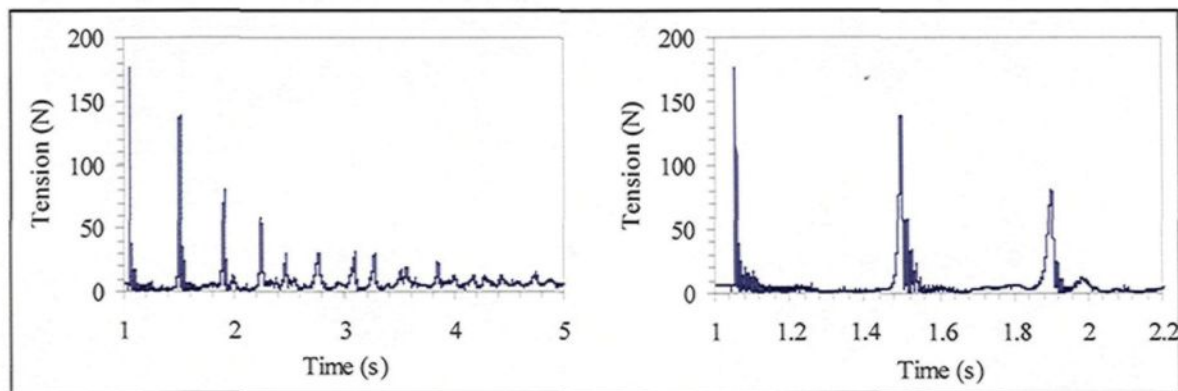
Figure 4.13 Time history of the resultant cable end-tension

A comparison of the bare cable dynamic end-tensions (Fig. 4.14a) measured at the two extremities of the span, resulting from the shock load applied at mid span, showed symmetry. Furthermore, a comparison of the dynamic response of the cable to the shock load measured at the ambient (20°C) and operational (-10°C) temperatures indicates agreement despite the impossibility to reproduce exactly the same shock load characteristics in the two tests (Fig. 4.14b).

a) Time history of cable end-tensions at the two extremities of the span

b) Time history of cable end-tensions measured at different temperatures
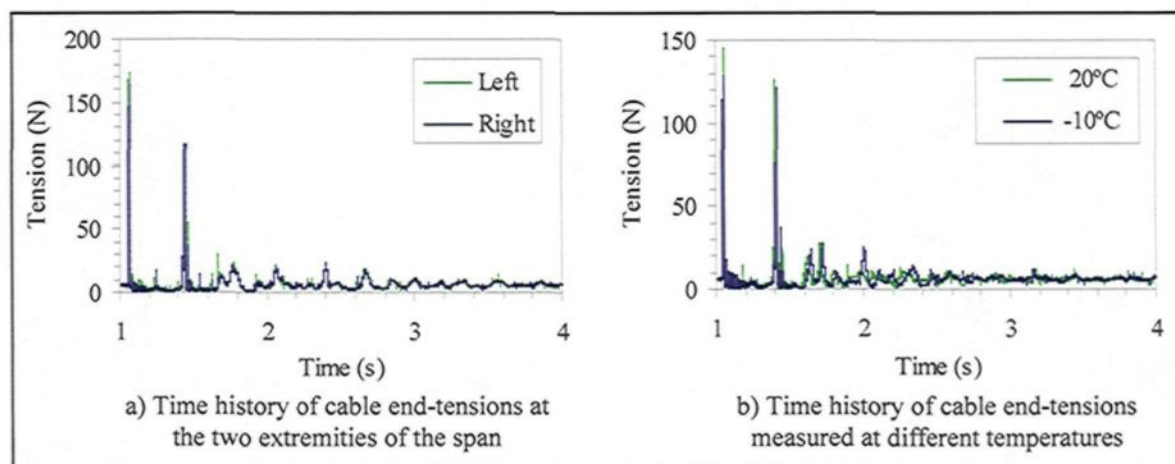
Figure 4.14 Time history of cable end-tensions

4.4.3 Time history of mid-span displacement

The vertical mid-span displacement of the stainless steel cable as a response to the shock load applied at mid span and depicted in Figure 4.11 is captured by the high speed digital camera and shown in Figure 4.15. Considering the available recording time of 3.2 s provided by the camera with the settings described in Section 4.2, the cable mid-span displacement history is available for only 1.2 s. Zero displacement refers to the cable configuration under its self weight. Time history of the cable vertical displacement at the mid span indicates an equivalent viscous damping in the order of 5% critical. The fundamental period of the cable span setup and the damping ratio are estimated from free vibration measurements as discussed in Appendix B.
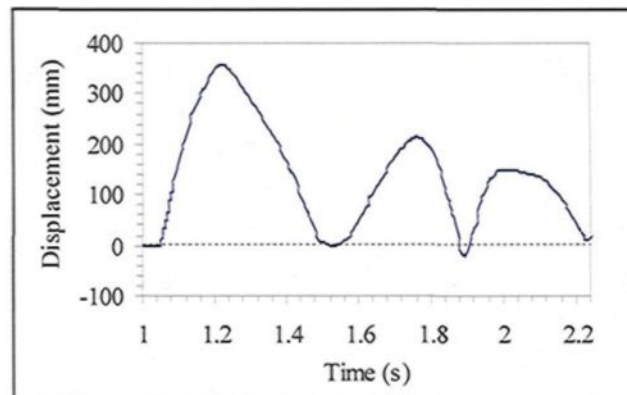
Figure 4.15 Vertical displacement at mid span

CHAPTER 5

COMPARISON OF NUMERICAL AND EXPERIMENTAL RESULTS

5.1 Introduction

In this chapter, the experimental results measured on the level single-span reduced-scale model are compared to those obtained from the numerical model. Several icing scenarios are studied that comprise bare and iced cable models with 1, 2 and 4 mm of equivalent radial ice thickness. A stainless steel cable (Appendix C) with a diameter of 4.1 mm is used throughout the analyses. However, one case with 1 mm equivalent radial ice thickness is studied using a more flexible stainless steel cable with a diameter of 3.2 mm. The span length is set to 4 m and the initial sag-to-span ratio is chosen to be 6% for all scenarios. The general numerical modeling approach presented in Chapter 3 is used throughout the analyses with the parameters specific to each cable span tested in the laboratory.

5.2 Bare cable model

In this section, the numerical and experimental results of a level single-span reduced-scale bare line subjected to a shock load (impact) at the mid span are compared in order to assess the parameters of the numerical model.

5.2.1 General considerations

In the experimental setup the cable and the centers of the attachment points at the end of the span are aligned so that the cable is in the same plane along its entire length. Furthermore, the shock loading piston setup at the mid span is also aligned in the cable plane. Therefore, the numerical model is also represented in the same 2-D plane. At this stage of analysis, the flexibility of the supports is not modeled and the cable ends are assumed to be rigidly fixed. The cable is modeled by 3-D two-node isoparametric truss elements using a linear elastic tension-only material model (MAT-1) (Fig. 5.1) as described in Chapter 3. In the model used here, the length of each cable element is found to be adequate by using a mesh of 25 elements, i.e. each element has a length of about 0.16 m with a constant cross-sectional area of 13.2 mm^2. The damping constant is set to represent an equivalent viscous damping of 2% critical. A value smaller than the one observed from the measurements (Appendix B) is chosen because some numerical damping is also introduced by the Newmark integration operator with parameters δ and α set to 0.55 and 0.3, respectively, as already indicated in Chapter 3.
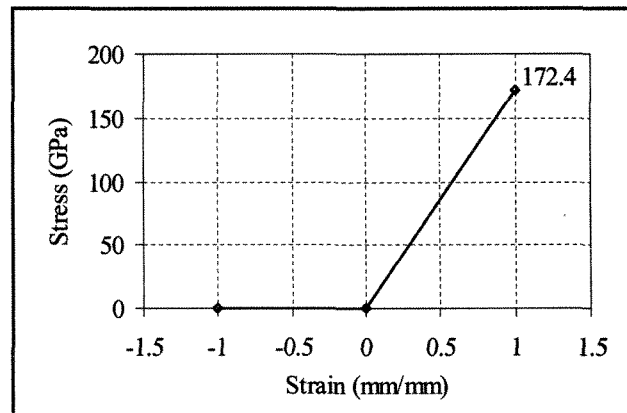
Figure 5.1 Tension-only cable material model (MAT-1)

Dynamic analysis is started after the first second, the preceding time being used for a static analysis of the initial equilibrium configuration. Besides the considerations introduced in Chapter 3 for the selection of time step, the sampling rate of each parameter measured during the experiments (4 kS/s) is also taken into account. Therefore, the time step is set to 0.25 ms. Several experimental tests were performed on the bare cable model at ambient temperature to investigate the nature of the problem and to obtain several data sets for comparison purposes. However, it should be noted that exact reproducibility of the experimental results is not feasible due to reasons explained in Chapter 4. In this section, comparisons of the numerical and experimental results of only one test with the shock load depicted in Figure 5.2 are presented. This shock load function serves as an input to the numerical model and is applied to the cable at mid span in the vertical upward direction.
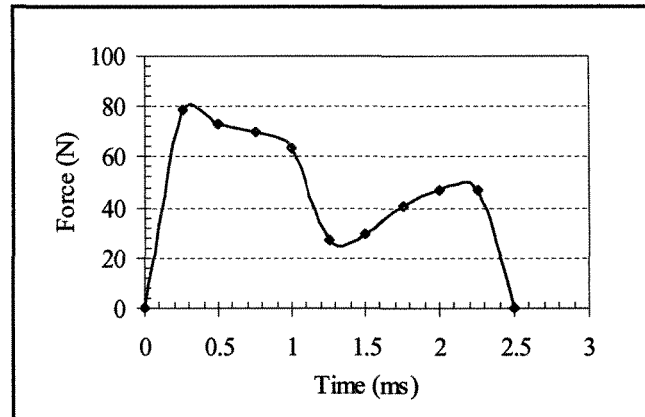
Figure 5.2 Shock load characteristics

5.2.2 Time history analysis results

Figures 5.3a and b present comparisons between the time history of cable tension calculated by the numerical model and that obtained experimentally for the first 3 s after the shock load was applied to the cable at t = 1.05 s. All values before t = 1.05 s represent the static response of the system subjected to its self-weight. The static initial tension of the cable is 5.86 N. Examination of the results reveals that the most severe dynamic effect occurs during the first second following the shock load. Comparison of the time history of the cable tensions (Fig. 5.3) shows general agreement between the calculated and measured values. However, the first peak value of cable tension obtained by the numerical model is overestimated compared to that obtained experimentally (Fig. 5.3b). Comparisons of other results of this test series show the same discrepancy, i.e. the first peak value of cable tension obtained numerically is overestimated while the rest of the graph shows good agreement between the measured and calculated values. The problem is assumed to arise from the sensitivity of the numerical model to the flexibility of the cable end supports of

the experimental setup, which is not considered in the numerical model at this stage of analysis, and also from the simplifying assumption in modeling the tensional rigidity of the cable. These assumptions are further investigated and discussed in this chapter. Comparisons of the time history of the cable mid-span displacements (Fig. 5.3c) reveal that the maximum cable jump at the mid span is accurately calculated by the numerical model. However, amplitude decay can be observed for the second and third peaks of the cable jump while there is agreement on the time scale. Zero displacement refers to the bare cable initial state.
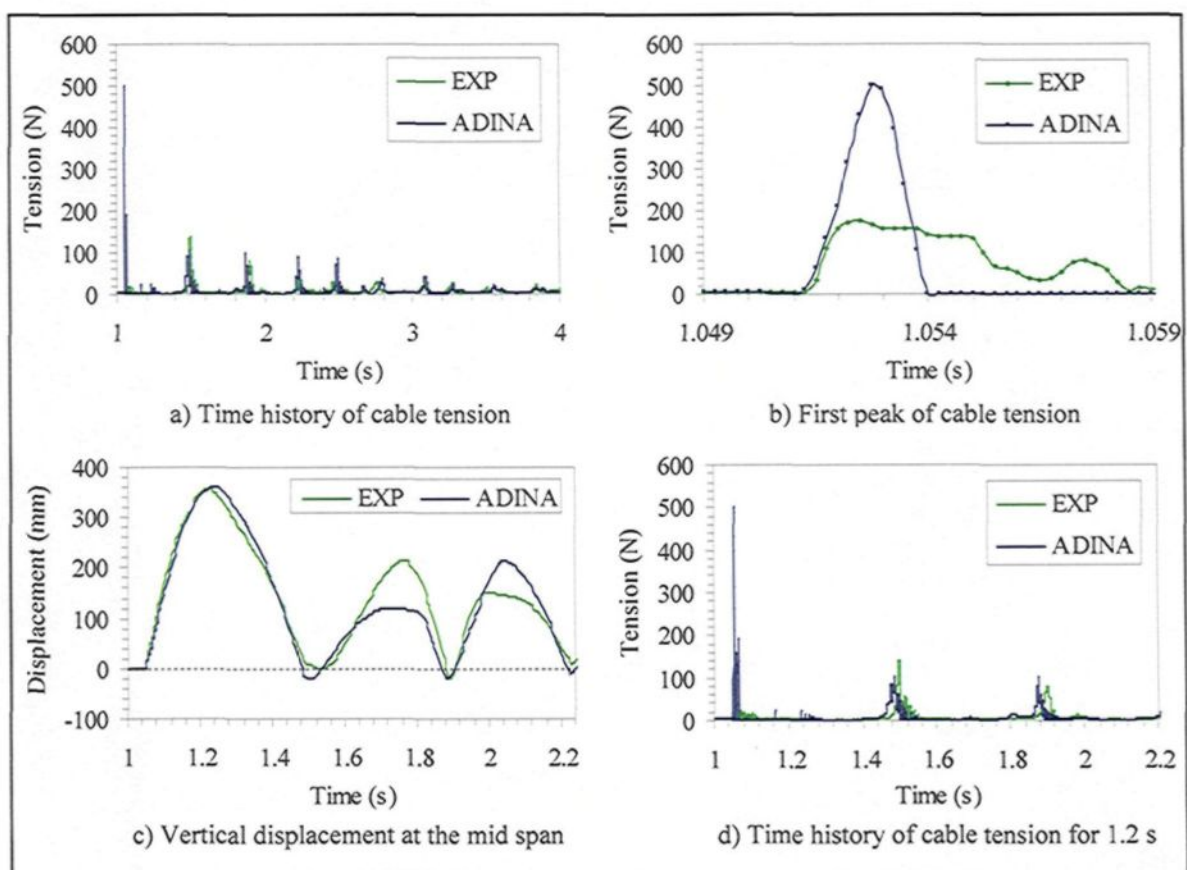
Figure 5.3 Comparison of numerical and experimental results of cable tension at the support and mid-span displacement

5.2.3 Sensitivity studies of the reduced-scale numerical model

In order to study the sensitivity of the reduced-scale numerical model, a number of parametric studies were performed introducing support flexibility and a more realistic cable extension material model. The sensitivity of the reduced-scale numerical model to the selection of the finite element mesh size is also presented next.

A) Model sensitivity to finite element mesh size

The sensitivity of the numerical model to the selection of the finite element mesh size is studied using 20- and 32-element models, i.e. each element has a length of about 0.2 m and 0.125 m, respectively. All other parameters of the model are kept the same. Figures 5.4 and 5.5 present comparisons between the time histories of cable tension and mid-span displacement calculated by the 20- and 32-element numerical models, respectively, and those obtained experimentally for the first 3 s after the shock load was applied to the cable at t = 1.05 s. Examination of the results reveals that the use of the 20-element numerical model yields to distorted time history graphs, as well as to period shortening (Fig. 5.4). Furthermore, the initiation of the first peak of cable tension at the support calculated by this numerical model is delayed in time compared to that obtained experimentally (Fig. 5.4b). The use of the 32-element numerical model yields to improved time history graphs (Fig. 5.5). However, the initiation of the first peak of cable tension at the support obtained by this numerical model occurs prior to that obtained experimentally (Fig. 5.5b), and this model overestimates the mid-span displacement (Fig. 5.5c).
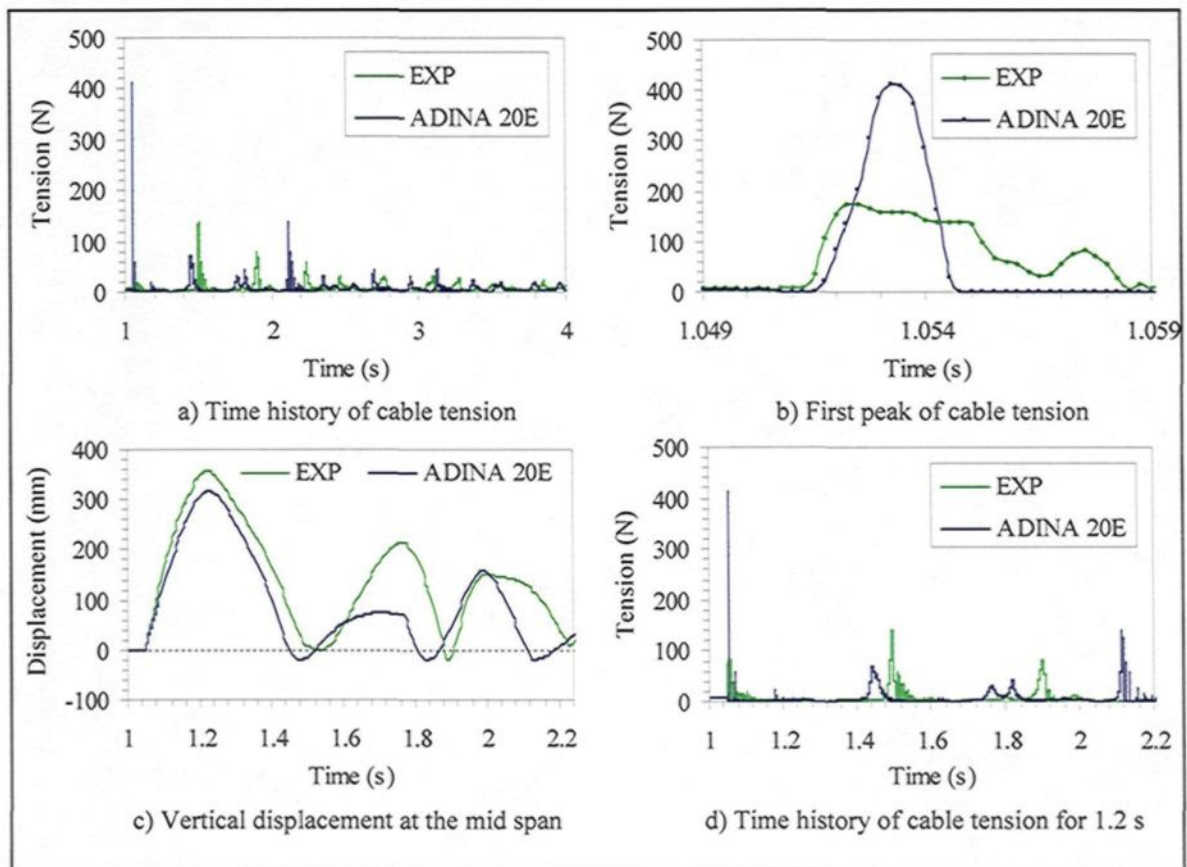
Figure 5.4 Comparison of numerical and experimental results of cable tension at the support and mid-span displacement using the 20-element numerical model
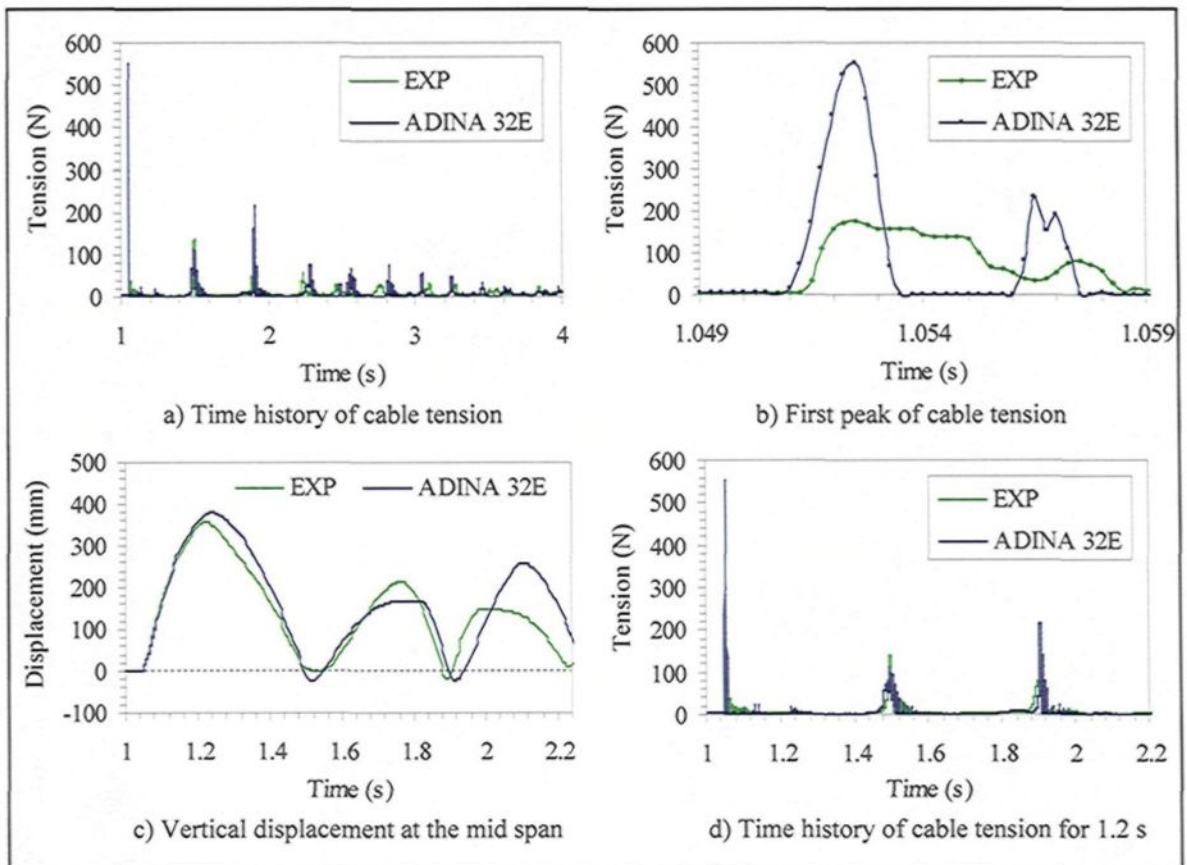
Figure 5.5 Comparison of numerical and experimental results of cable tension at the support and mid-span displacement using the 32-element numerical model

B) Model sensitivity to support flexibility

In order to introduce support flexibility in the numerical model, the hinged support arms are modeled using linear spring elements. Four spring elements are defined at the two extremities of the cable in the horizontal and vertical directions, respectively. Each spring element has two degrees-of-freedom corresponding to the horizontal and vertical translations at each cable attachment point. Fixed boundary conditions are assigned to the spring elements as depicted in Figure 5.6. The length and the mass of each spring element are set to 0.09 m and 0.62 kg, respectively. Elements with arbitrary axial rigidity values (EA) ranging from $5 \cdot 10^4$ to 10^7 N and with (C = 100 Ns/m) and without viscous damping are studied. The modeling results obtained with these parameters are shown in Figure 5.7.
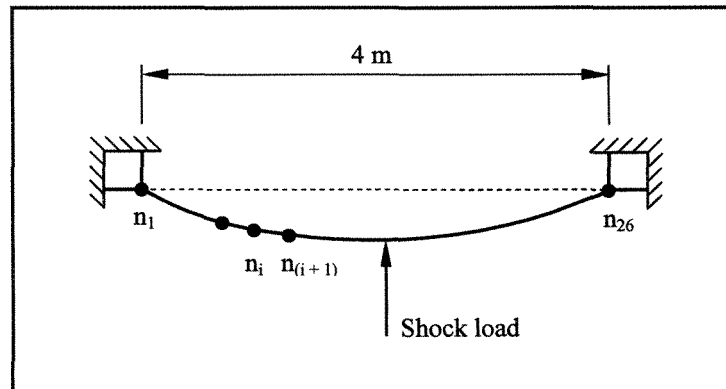
Figure 5.6 Modeling representation of hinged support arms

Comparisons of the results obtained for the maximum cable tensions at the support (Fig. 5.7a) indicate that the more flexible the support is, the smaller the amplitude of the maximum cable tension, and i.e. it shows convergence towards the experimental value.

However, the results obtained for the maximum cable jump at mid span (Fig. 5.7b) show the reverse tendency, i.e. the stiffer the support is, the more accurate the maximum mid-span displacement obtained numerically. Furthermore, analysis of the displacement results of the cable attachment points in the horizontal and vertical directions (Figs. 5.7c and d) reveals that the more flexible the support is, the higher the displacement of the attachment points. For instance, a numerical model with a support rigidity value of $5 \cdot 10^4$ N and without element damping showing to model the maximum cable tension the most accurately but the cable mid-span displacement the least accurately (c.f. Figs. 5.7a and b) results in a horizontal displacement of the cable attachment point of 2.06 mm, which is unrealistic. Furthermore, analysis of the time history results of cable tensions and mid-span displacements reveals that the more flexible the support, the more distorted the graphs compared to those obtained experimentally. The same negative effect is observed when support damping is used. The numerical model seems to be non-sensitive to support damping used (100 Ns/m) for the stiffer supports (e.g. EA > $5 \cdot 10^6$ N). However, it has a negative effect on all results for the lower values of the support rigidity studied. Therefore, one can conclude that the use of support damping is unrealistic.
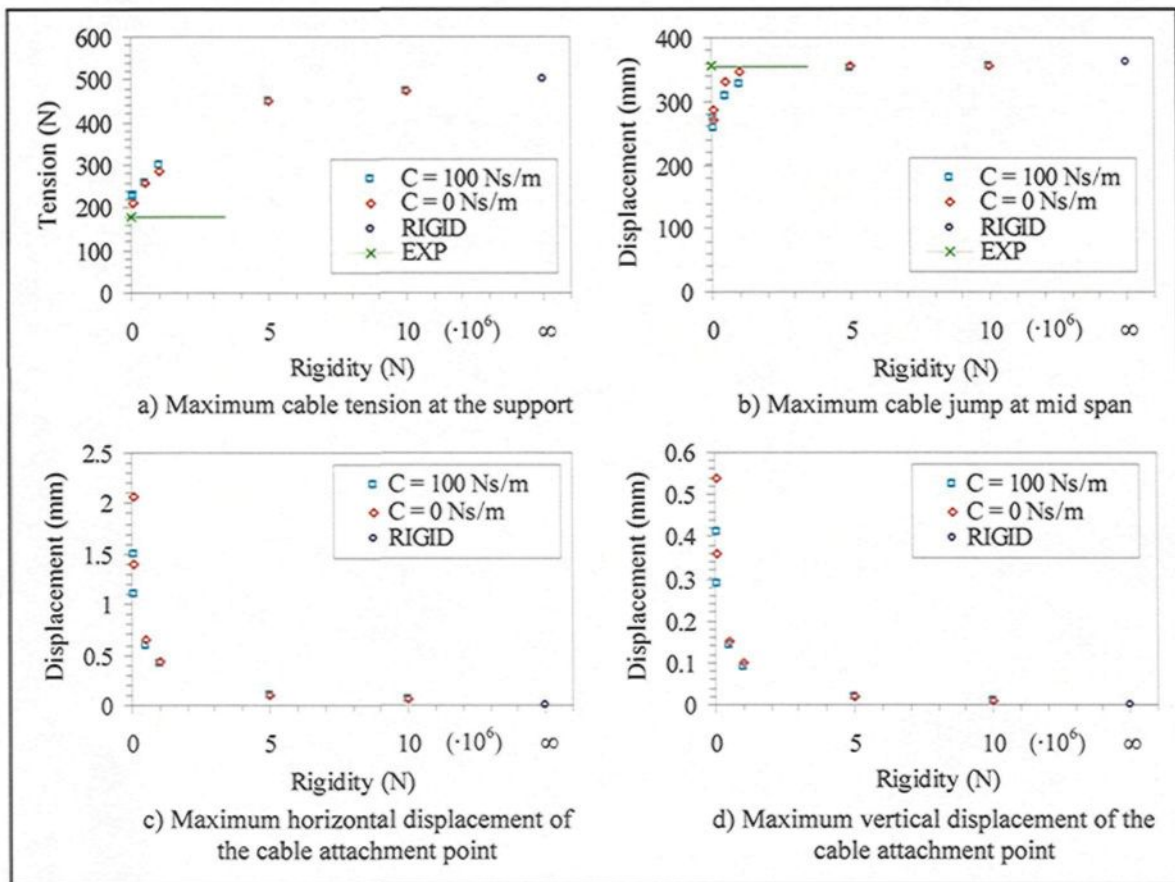
Figure 5.7 Effect of support flexibility

Figure 5.8 shows comparisons between the most accurate time history results of cable tension and mid-span displacement obtained by the numerical model with flexible supports (FLEX) and those obtained experimentally (EXP). The use of flexible supports with an axial rigidity of 10^6 N, without element damping, results in a decrease of 45% of the maximum cable tension (c.f. Fig. 5.3b and Fig. 5.8b) without severe distortion of the time history results of cable tension and mid-span displacement obtained for the first 1.2 s (Figs. 5.8c and d). However, a slight shift of the period can be observed compared to that obtained without modeling the support flexibility (RIGID) (Fig. 5.9). Furthermore, a slight

distortion of the time history of cable tension at the support can also be observed after t = 3

s (c.f. Fig. 5.3a and Fig. 5.8a).
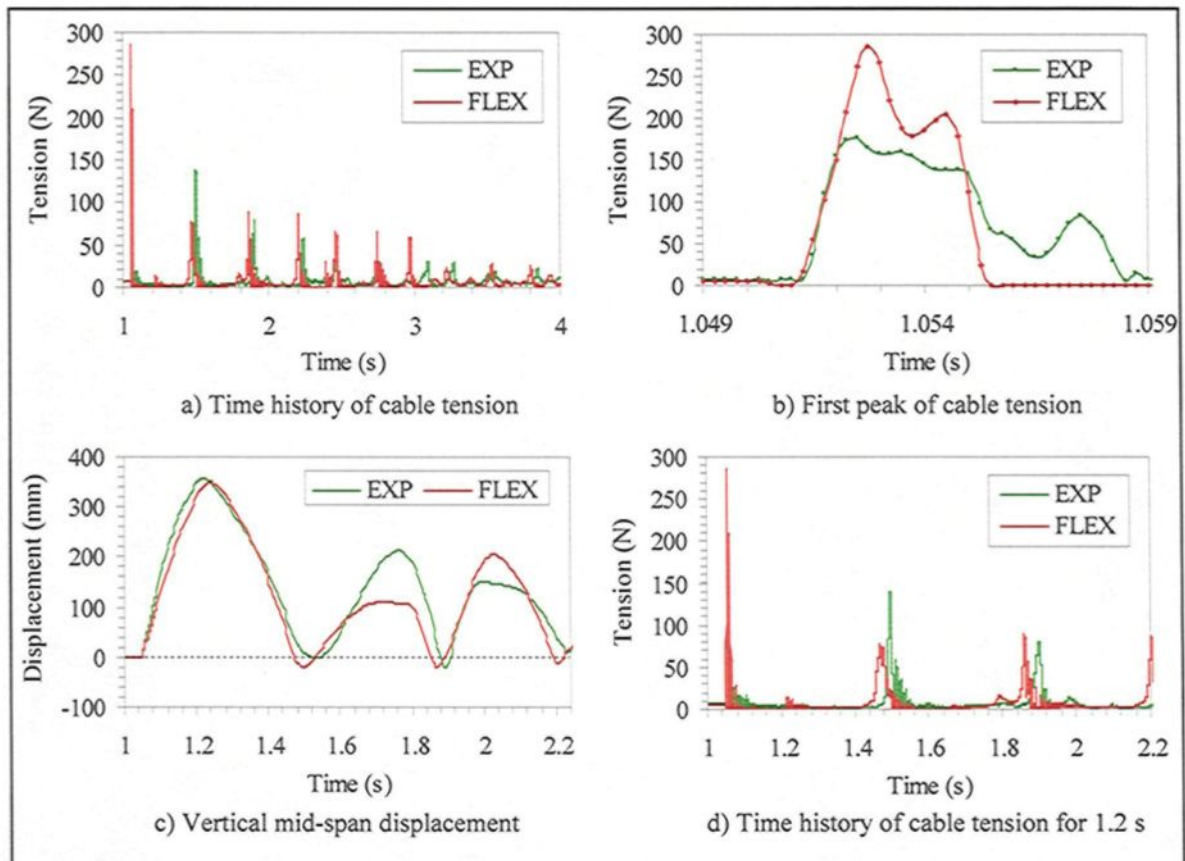
Figure 5.8 Comparison of numerical and experimental results of cable tension at the support and mid-span displacement by modeling support flexibility (EA=10^6 N)

88
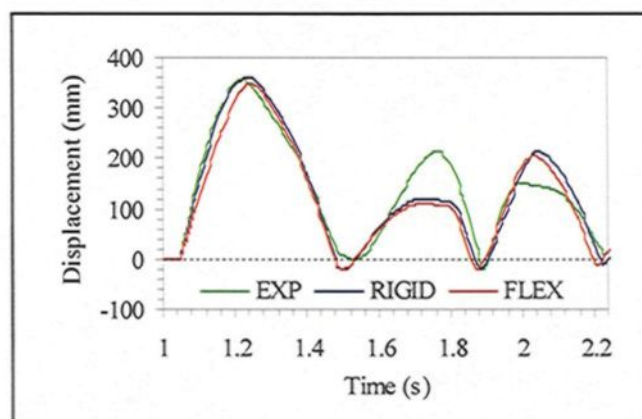
Figure 5.9 Comparison of numerical and experimental results
of cable mid-span displacement with rigid (RIGID)
and flexible (FLEX) supports

C) Model sensitivity to cable tensional rigidity

The tensional rigidity of the cable (EA), defined as the product of its elastic modulus
(E) and cross-sectional area (A), was measured with a standard tension machine as
described in Appendix B. The results show that the effective tensional rigidity of such
stainless steel wire rope made of seven strands is less than its theoretical value, as well as
being nonlinear and dependent on the initial tension in the cable. Furthermore, in terms of
cable vibration, it appears that EA varies with cable deformation, meaning that it is not the
same along a given vibrating loop, and also varies with time during the vibration cycle.
Therefore, the influence of the tensional rigidity of the cable elements on the dynamic
response calculated by the reduced-scale numerical model is studied by using a cable
material model with the characteristics obtained from the static tensile tests. This tension-
only material model (MAT-2) defined for each cable element is obtained by a multi-linear

approximation of the experimental stress-strain curve of the stainless steel stranded cable

(Fig. B.6a), as shown in Figure 5.10.
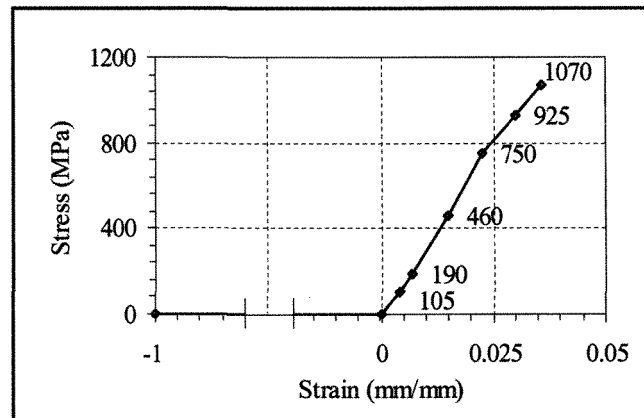
Figure 5.10 Approximate multi-linear tension-only
elastic cable material model (MAT-2)

Figure 5.11 shows comparisons between the time history results of cable tension and mid-span displacement obtained by the numerical model using the MAT-2 cable material model (Fig. 5.10) and those obtained experimentally (EXP). The use of this cable material model (i.e. more flexible cable) in ADINA results in a decrease of 52% of the maximum cable tension (c.f. Fig. 5.3b and Fig. 5.11b) without severe distortion of the time history results of cable tension and mid-span displacement obtained for the first 1.2 s (Fig. 5.11c and d). However, as also stated for the results obtained by the numerical model with support flexibility, a shift of the period can be observed compared to that obtained by the numerical model with the MAT-1 (Fig. 5.1) material model (Fig. 5.12). In addition, there is a distortion of the time history of cable tension at the support occurring after t = 3 s (c.f. Fig. 5.3a and Fig. 5.11a). Nevertheless, this modeling approach results in a higher decrease of the first peak of cable tension, i.e. it provides a more accurate value for the maximum

cable tension at the support (c.f. Figs. 5.8b and 5.11b) without severe distortion of time history results. It also results in a higher decay of maximum cable jump than the most accurate numerical model with flexible supports (c.f. Figs. 5.9 and 5.12).
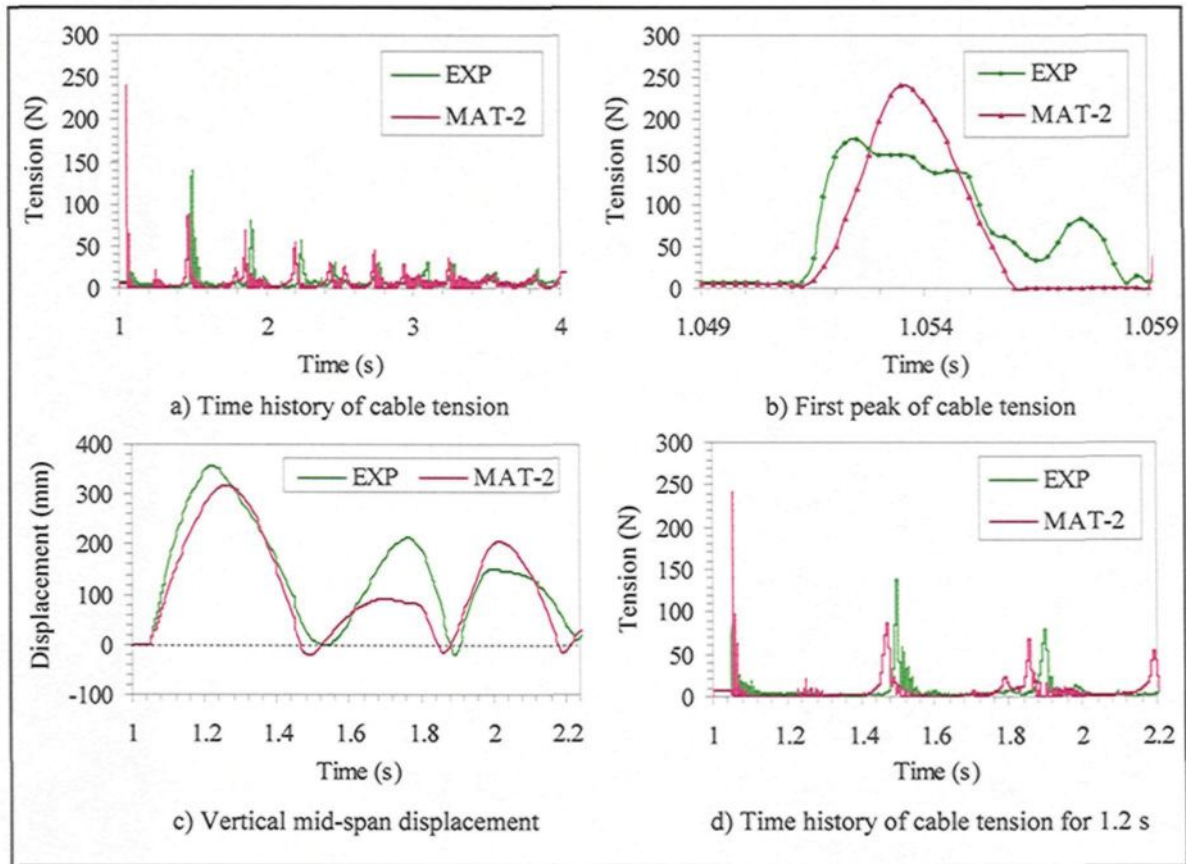
Figure 5.11 Comparison of numerical and experimental results of cable mid-span displacement and tension using MAT-2 cable material model
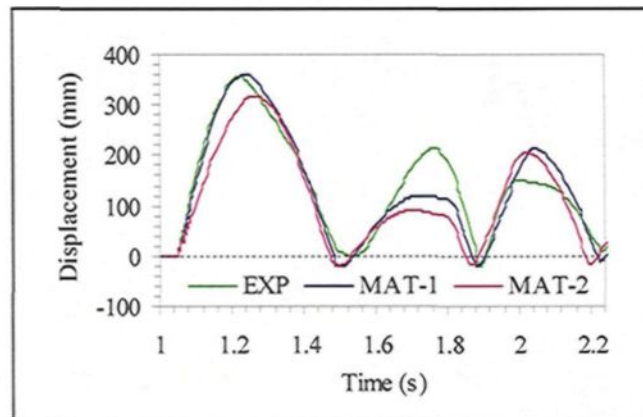
Figure 5.12 Comparison of numerical and experimental results
of cable mid-span displacement using MAT-1 and
MAT-2 cable material models

The maximum cable tension at the support obtained by the numerical model with the MAT-2 cable material model is 241 N (Fig. 5.11b). Hence, the maximum stress calculated in the cable at the support is 18.3 MPa indicating that only the first linear section (0-105 MPa) of the MAT-2 cable material model (Fig. 5.10) is used for the calculations in the numerical model (i.e. EA = 346,500 N). In spite of the fact that cable stiffness varies with conductor deformation due to strand slippage or inter-strand motion within the cable, the macroscopic modeling approach adopted for the cable cannot account for these variations in the region of prevailing loads.

D) Summary of the sensitivity studies

Sensitivity studies of the reduced-scale numerical model presented reveal that the most accurate predictions of the maximum cable tension are obtained with the 25-element mesh model including the effects of system flexibility that may arise from either the end supports or the cable itself. Both improved modeling approaches of the system flexibility tend to yield accurate results for the maximum cable tension. The best time history results of cable tension with flexible supports are obtained with a value of support axial rigidity of 10^6 N. However, modeling of the support flexibility yields to the displacement of the cable attachment points, and the more flexible the support is, the higher the displacement of the attachment points. Even a value of support rigidity of 10^6 N results in a horizontal displacement of cable attachment points of 0.44 mm. However, no explanation can be given for such a displacement of the attachment points in the reduced-scale experimental setup. Therefore, it is assumed that the effect of system flexibility of the reduced-scale experimental model derives from the flexibility of the stainless steel cable used. However, on the other hand, comparisons of time history results of cable mid-span displacement obtained by the numerical model and those obtained experimentally indicate that cable mid-span displacement is accurately modeled by using the taut cable modeling approach, i.e. MAT-1 cable material model with greater stiffness. Furthermore, comparisons of the time history results of cable tension obtained by the numerical model and those obtained experimentally reveal that the most accurate time history plots of cable tension at the support are also obtained by using the taut cable modeling approach, except for the maximum cable tension as described above. These reverse tendencies are probably due to

the fact that the displacements and tensions are not measured at the same location, and that at the moment when the shock load is applied to the cable at the mid span, a transverse as well as a longitudinal wave is generated that induces the maximum cable tension at the support. However, the energy of the shock load is dissipated much faster in a flexible cable (in both tensional and flexural effects) than in a taut cable before hitting the supports and therefore it results in a smaller value of the maximum cable tension at the support. Nevertheless, when the cable is already in motion in the vertical direction, it has the same behavior as that of a taut cable, i.e. a cable with greater stiffness. The numerical model does not take into account the variations in the cable stiffness in the region of prevailing loads: cable material characteristics are not available for such small loads due to the tensile test limitations described in Appendix B. The cable axial rigidity is, therefore, considered constant (EA = 346,500 N) for the region of prevailing loads in the calculations.

As a conclusion of these sensitivity studies, the 25-element numerical model is used in the remaining analyses of iced cables using the MAT-1 cable material model (EA = 2,275,680 N) (Fig. 5.1) to generate the time history results of mid-span displacement, and the first linear section (0-105 MPa) of the MAT-2 (tension-only) cable material model (Fig. 5.10) with a constant stiffness (EA = 346,500 N) to obtain the time history results of cable tension at the support.

5.3 Iced cable models

In this section, numerical and experimental results of a level single-span reduced-scale line with ice loads representing 1, 2 and 4 mm of equivalent radial ice thickness subjected to shock load (impact) at the mid span are compared.

5.3.1 General considerations

Despite the fact that the cable and the shock load applied at the mid-span are in the same plane, as stated above, due to asymmetric ice accretion on the cable related to wind direction (Fig. 5.13a), a small out-of-plane motion of the cable is observed during the experiments when the shock load is applied, i.e. eccentric out-of-plane forces occur. Nevertheless, accreted ice on the cable is modeled as separate 3-D two-node iso-beam elements with rectangular cross-sections parallel to each cable element in the 2-D plane, as described in Chapter 3. Parameters of the numerical ice-cable composite model are set as found in Table 5.1 including values used for the cable initial strains ($\varepsilon_{initial}$) and the cross-sectional parameters of the iso-beam ice elements (W and H) representing 1, 2 and 4 mm of equivalent radial ice thickness (t_{ice}) around a cable of 4.1 and 3.2 mm in diameter (d_c), respectively (Fig. 5.13). All the other parameters of the numerical ice-cable composite model are defined as discussed in the previous section. Due to limitations of the spraying trajectory, 30 cm of the cable at both ends of the span remain ice free. Therefore, two ice elements are omitted at both ends of the span just next to the support nodes and fixed rotational boundary conditions are assigned to nodes 2 and 25 as depicted in Figure 5.14. Analysis of the bare cable model revealed that the most severe dynamic effects occur

during the first second following the shock load application. Therefore, results are presented in the remainder of the analyses for a time interval corresponding to available cable mid-span displacement data (3.2 s of recording time).
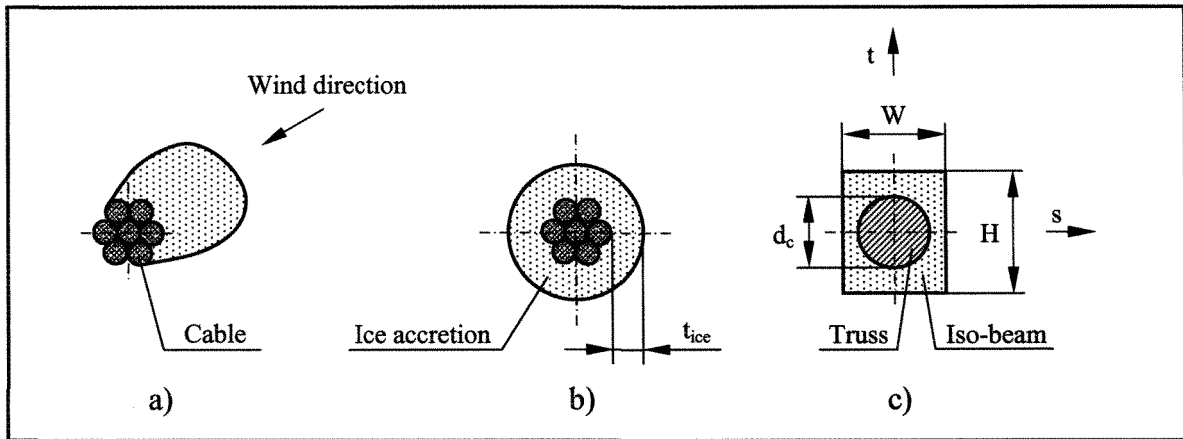
Figure 5.13 Ice accretion on the stainless steel cable and its model representation
a) Artificial ice accretion on the cable; b) Idealized shape of accreted ice on the cable;
c) Iso-beam representation of accreted ice

Ice-shedding scenario	Cable diameter d_c (mm)	Ice thickness t_{ice} (mm)	Cable initial strain $\varepsilon_{initial}$ (mm/mm)	Cross-section of ice accretion	
				W (mm)	H (mm)
1	4.1 [70 g/m]	1 [14.4 g/m]	$3.032 \cdot 10^{-6}$	6.36	2.52
2	4.1 [70 g/m]	2 [34.5 g/m]	$3.735 \cdot 10^{-6}$	7.86	4.87
3	4.1 [70 g/m]	4 [91.6 g/m]	$5.800 \cdot 10^{-6}$	11.00	7.09
4	3.2 [43 g/m]	1 [11.9 g/m]	$3.230 \cdot 10^{-6}$	5.29	2.49

[Mass per unit length]

Table 5.1 Parameters of the numerical ice-cable composite model

The shock load is applied to the cable at mid span at t = 1.05 s for all ice-shedding scenarios. Figure 5.15 shows the characteristics of shock loads measured and defined as input to the numerical model for the ice-shedding scenarios studied.
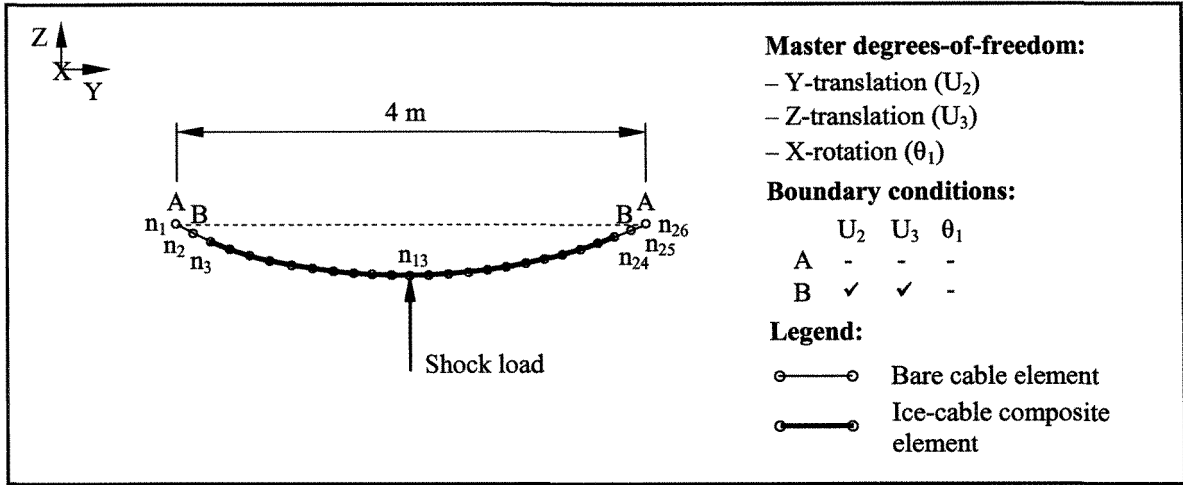
Figure 5.14 Schematic of the reduced-scale numerical ice-cable composite model
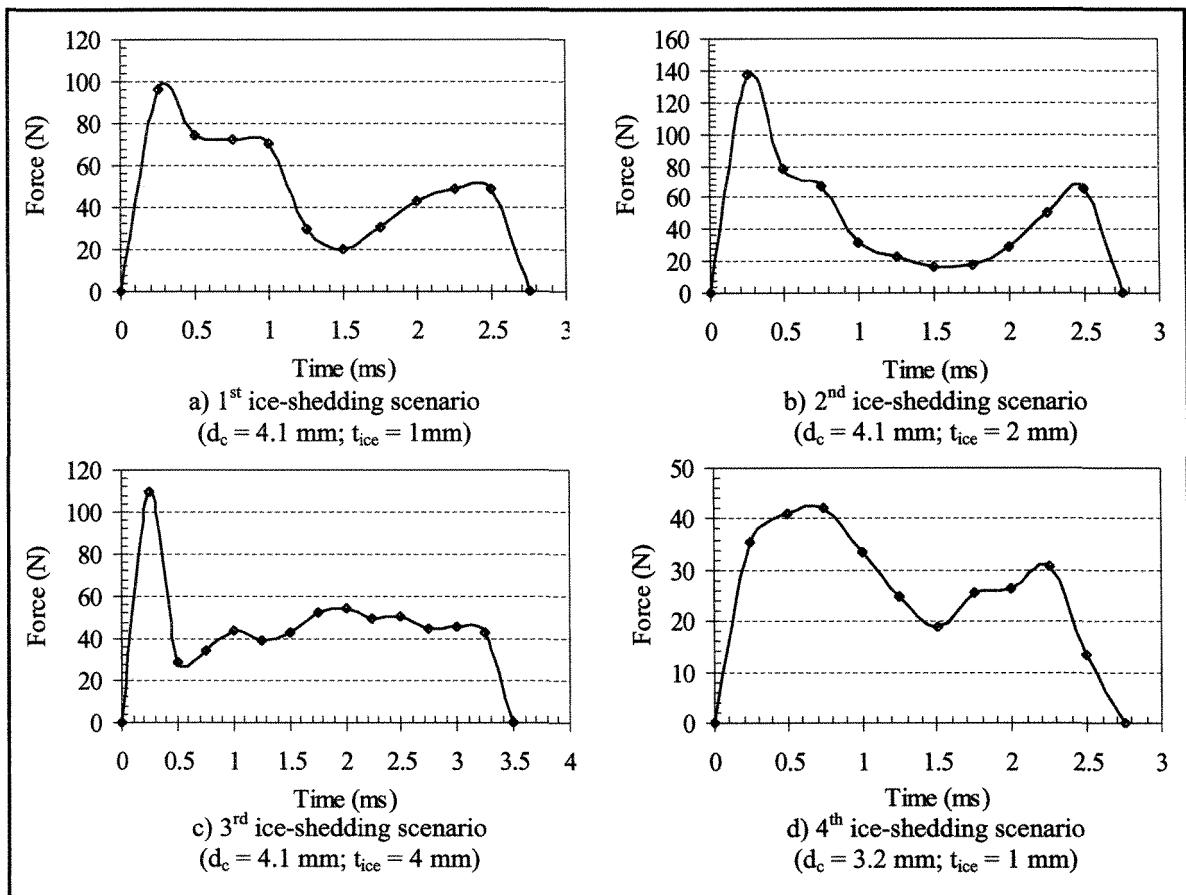
Figure 5.15 Shock load characteristics of the four ice-shedding scenarios

5.3.2 Ice-shedding scenarios

Figures 5.16 to 5.24 show comparisons between time history results of cable tension and mid-span displacement, as well as the rate of ice shedding in the span, i.e. the fraction of the ice shed in the span, obtained by the numerical model and those obtained experimentally (EXP) for the four ice-shedding scenarios studied. For each scenario, it can be noted that the maximum cable jump at the mid span is accurately computed by the numerical model. However, results of the ice-shedding scenarios with 2 and 4 mm of equivalent radial ice thickness (Figs. 5.18 and 5.20) indicate that the numerical model shows higher flexibility and computes higher cable jumps for the second and third peaks compared to the experimental model. This is probably due to the fact that the effective rate of ice shedding calculated by the numerical model and that obtained experimentally differ. Therefore, the shedding of a thicker ice accretion from the cable generates additional cable displacement in the numerical model (Fig. 5.20c) while the remaining ice accretion on the experimental model stiffens the cable and provides higher internal damping.

The rate of ice shedding obtained experimentally is different for each scenario; however, each scenario shows the same tendency of ice-shedding. Effective ice shedding occurs at the mid span, where the shock load is applied, on a length of 10 to 30 cm depending on the scenario considered, as well as at a distance of about 37 cm from the point of impact in the two directions, on a length of only about 2 cm. Depending on each scenario studied, a significant portion of the ice that remains on the cable breaks up showing extensive cracking (Fig. 5.24). This is due to the fact that the shock load applied to the cable at the mid span generates a transverse wave in the cable that quickly

transforms into a longer vibrating loop with a wave length of about 74 cm that further expands to the whole span. Effective ice shedding takes place where the transverse wave propagation is directly observed and where the long vibrating loop forces the cable to bend, i.e. where significant bending of the iced cable occurs. Elsewhere (highlighted in grey in the figures) extensive cracking of the ice deposit is observed but due to the adhesive strength of ice, ice shedding is not triggered. It should be emphasized that the adhesive strength of ice is not considered in the numerical model. Therefore, in each ice-cable composite element when the failure criterion of the ice in terms of axial and bending stress-strain relations is fulfilled at any integration point, the ice element and its mass and stiffness contributions are removed from the model, i.e. effective ice-shedding is assumed to take place. Based on this failure criterion, comparisons of numerical and experimental results of ice shedding reveal that the rate, as well as the location of the ice shedding is satisfactorily calculated by the numerical model (Table 5.2). However, it should be noted that the slight difference, observed between the values obtained by the numerical model and the assumed rate of ice shedding obtained from the experiments, is mainly due to the fact that single cracks that occur at both ends of the span during the experiments are not considered.

Analysis of the time history results of cable tension at the support indicates that the thicker the ice deposit on the cable, i.e. the higher the additional stiffness of the ice-cable composite model, the more accurate the maximum cable tension obtained by the numerical model compared to that obtained experimentally (c.f. Fig. 5.16b and Fig. 5.18b). However, examination of the results of the 3rd ice-shedding scenario (Fig. 5.20) indicates that the

equivalent radial ice thickness of 4 mm defined in the numerical model may represent a higher stiffness of the ice-cable composite model compared to that of the experimental model since the maximum cable tension calculated by the numerical model is slightly underestimated.

Ice-shedding scenario	Cable diameter (mm)	Ice thickness (mm)	R.I.S. by ADINA (%)	R.I.S. by experiments	
				Effective (%)	Assumed (%)
1	4.1	1	90	8	75
2	4.1	2	76	9	50
3	4.1	4	57	5	30
4	3.2	1	90	7	75

Table 5.2 Rate of ice shedding (R.I.S.) obtained numerically and experimentally

In order to study both experimentally and numerically the effect of cable stiffness on the effectiveness of ice removal, a test series was performed using a stainless steel cable of 3.2 mm in diameter. Test results reveal that despite the lower amplitude of the shock load (c.f. Figs. 5.15a and d) that can be obtained on a lighter cable like this with the same parameters of the shock load generator, the rate of ice-shedding does not change (Table 5.2), i.e. the effectiveness of ice removal can be assumed to improve compared to that of a more rigid cable.
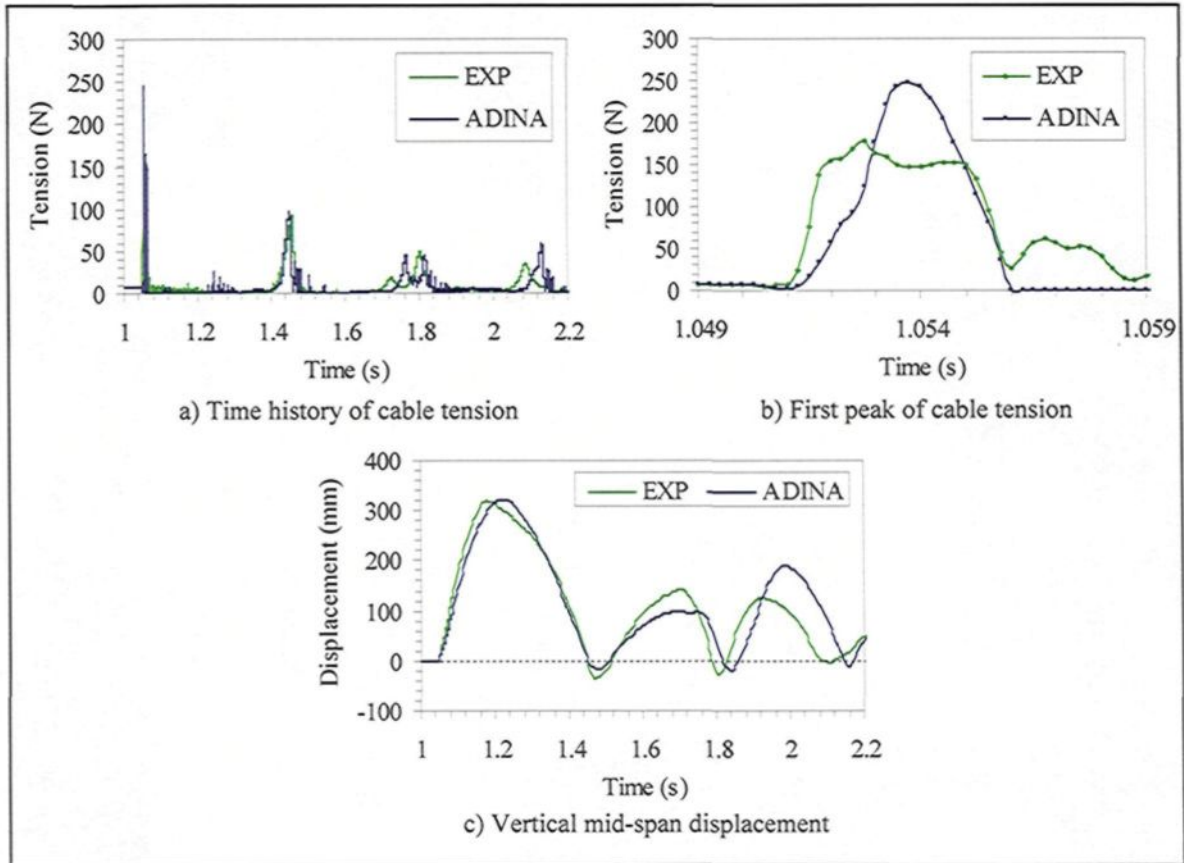
Figure 5.16 Comparison of numerical and experimental results of cable mid-span displacement and tension for the 1st ice-shedding scenario (d_c = 4.1 mm; t_{ice} = 1 mm)
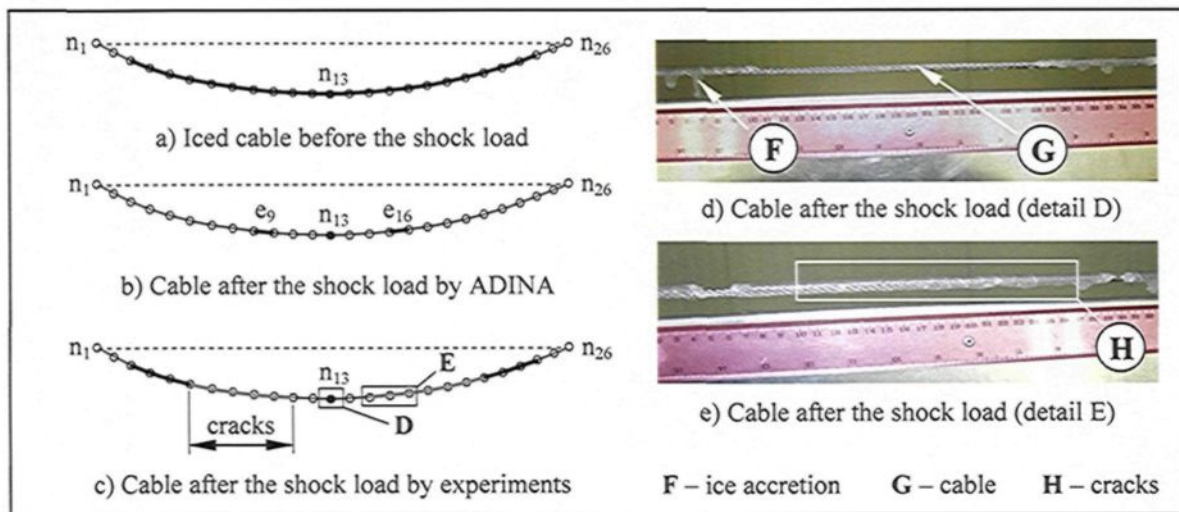
Figure 5.17 Rate of ice shedding obtained by ADINA and experiments for the 1st ice-shedding scenario
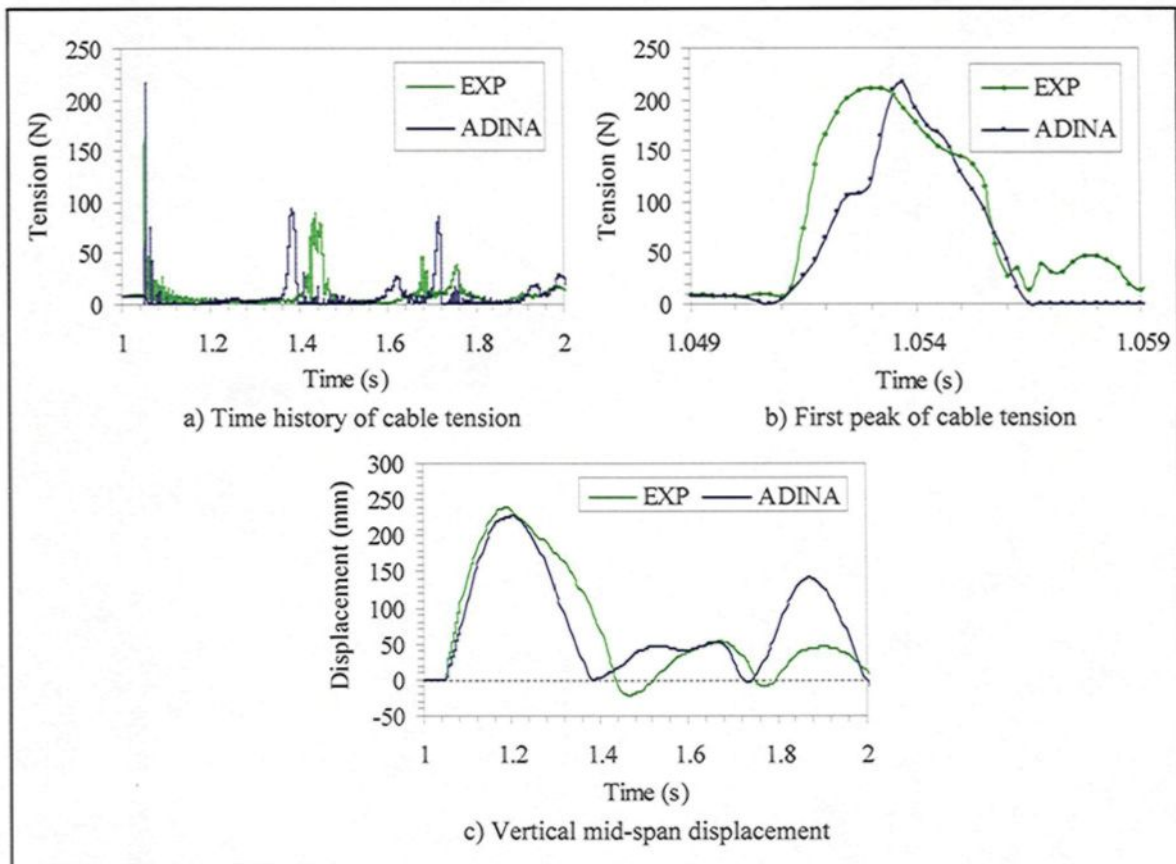
Figure 5.18 Comparison of numerical and experimental results of cable mid-span displacement and tension for the 2nd ice-shedding scenario (d_c = 4.1 mm; t_{ice} = 2 mm)
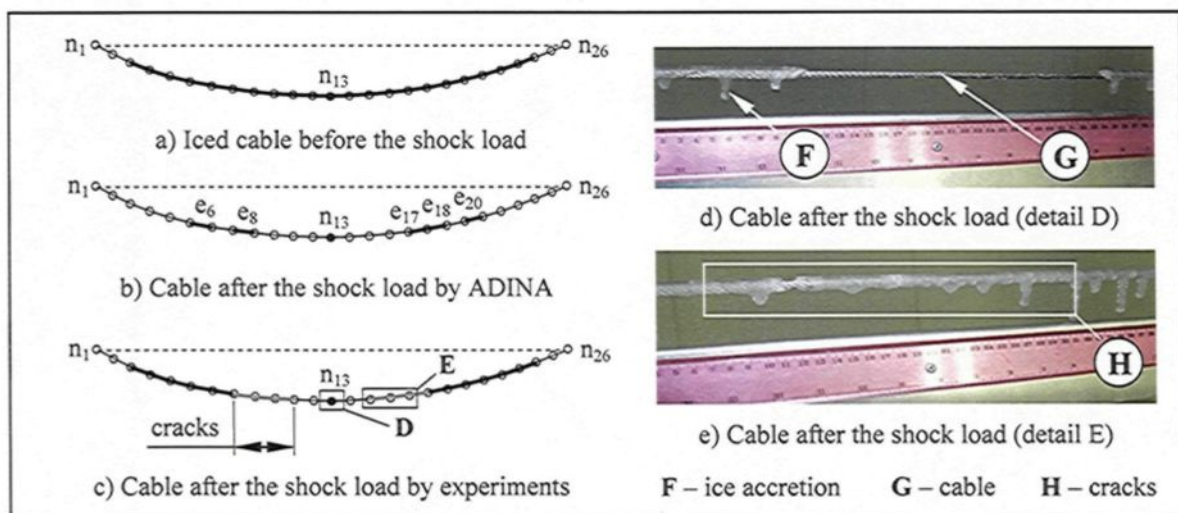
Figure 5.19 Rate of ice shedding obtained by ADINA and experiments for the 2nd ice-shedding scenario
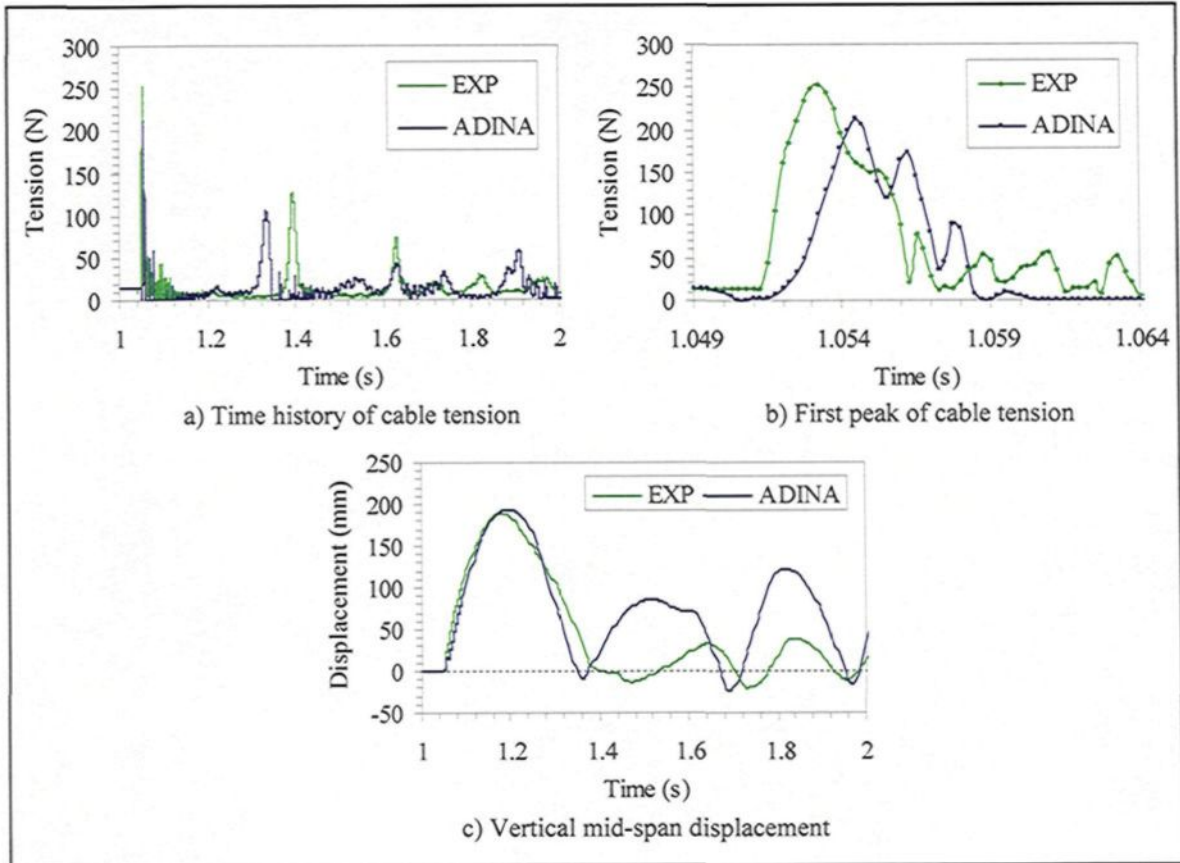
Figure 5.20 Comparison of numerical and experimental results of cable mid-span displacement and tension for the 3rd ice-shedding scenario (d_c = 4.1 mm; t_{ice} = 4 mm)
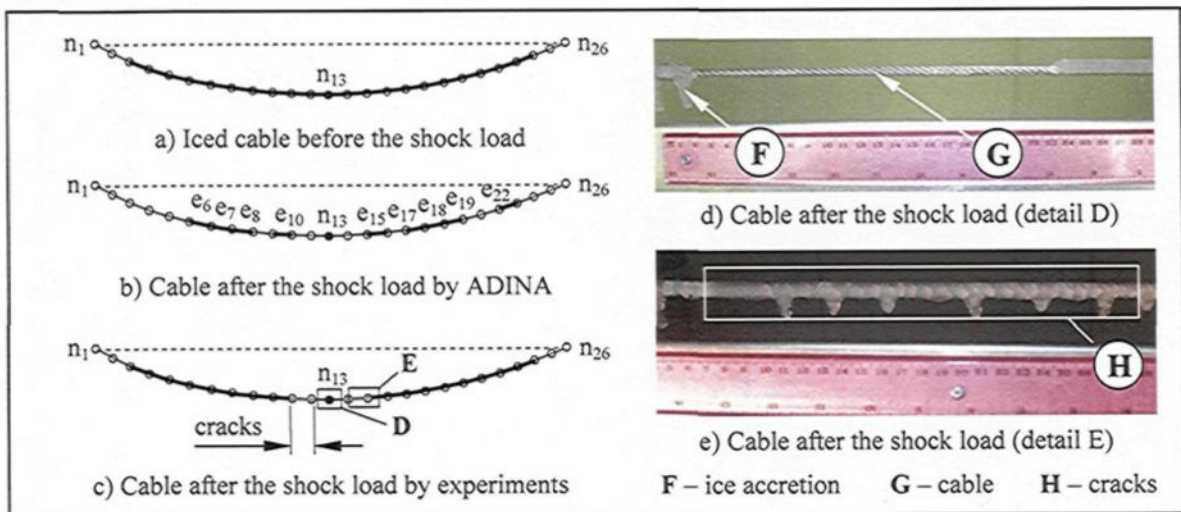
Figure 5.21 Rate of ice shedding obtained by ADINA and experiments for the 3rd ice-shedding scenario

a) Time history of cable tension

b) First peak of cable tension

c) Vertical mid-span displacement
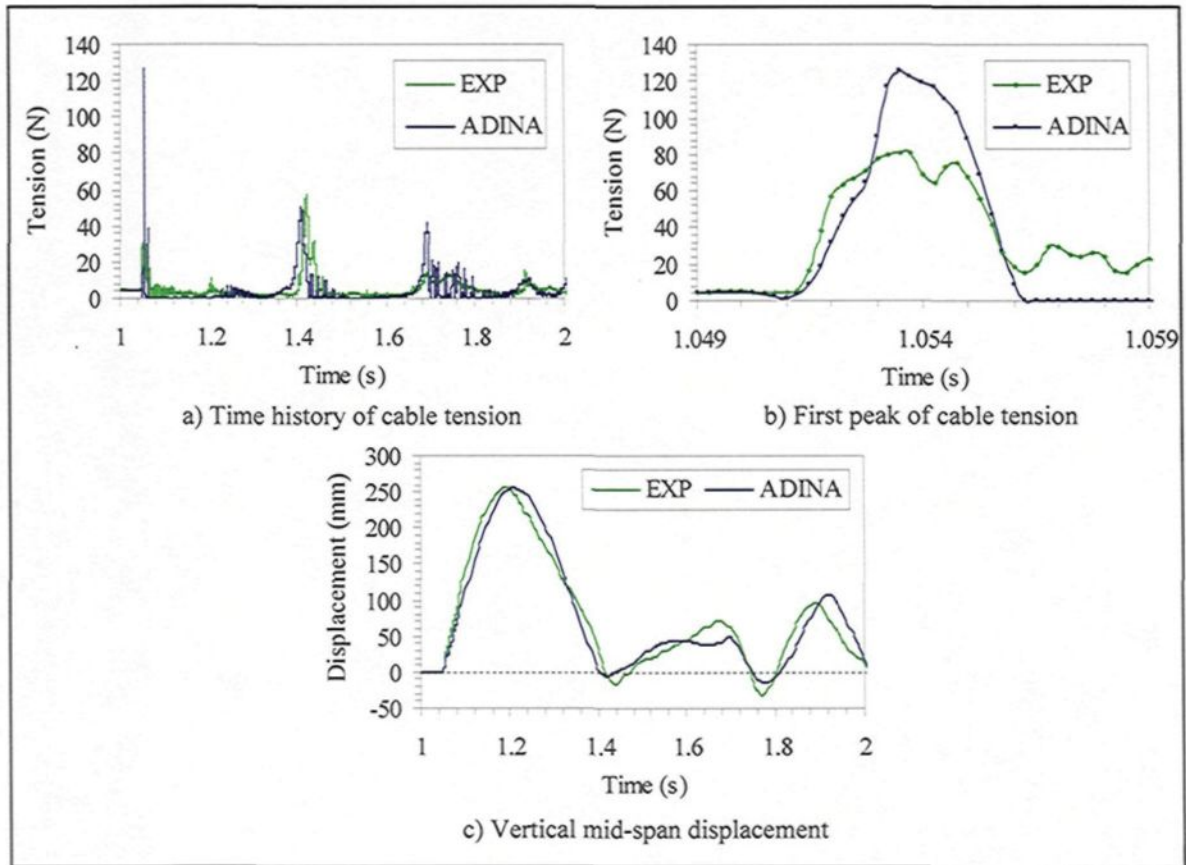
Figure 5.22 Comparison of numerical and experimental results of cable mid-span displacement and tension for the 4th ice-shedding scenario (d_c = 3.2 mm; t_{ice} = 1 mm)

a) Iced cable before the shock load

b) Cable after the shock load by ADINA

c) Cable after the shock load by experiments

d) Cable after the shock load (detail D)

e) Cable after the shock load (detail E)

F – ice accretion   G – cable   H – cracks
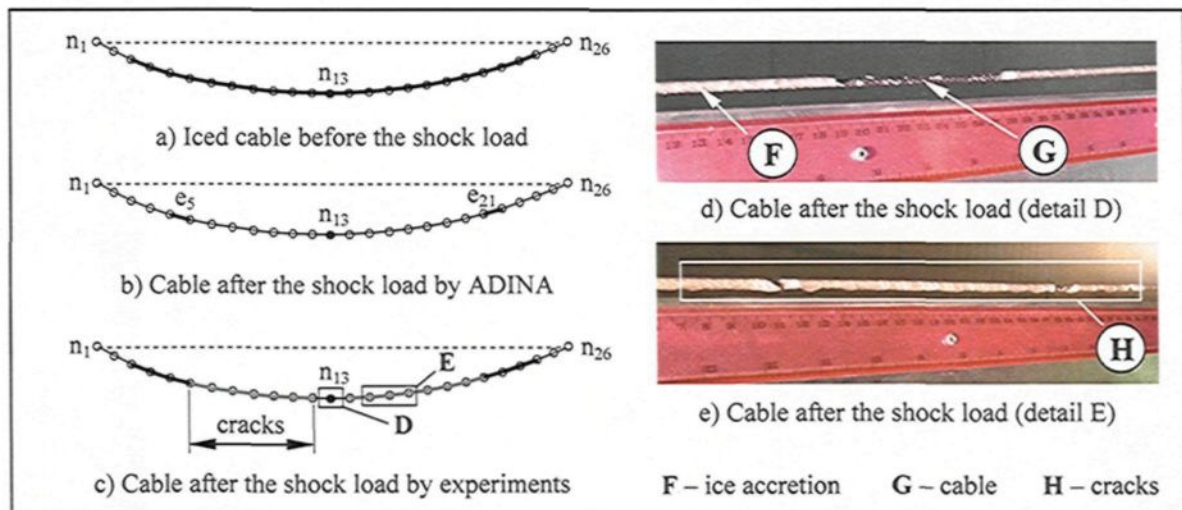
Figure 5.23 Rate of ice shedding obtained by ADINA and experiments for the 4th ice-shedding scenario
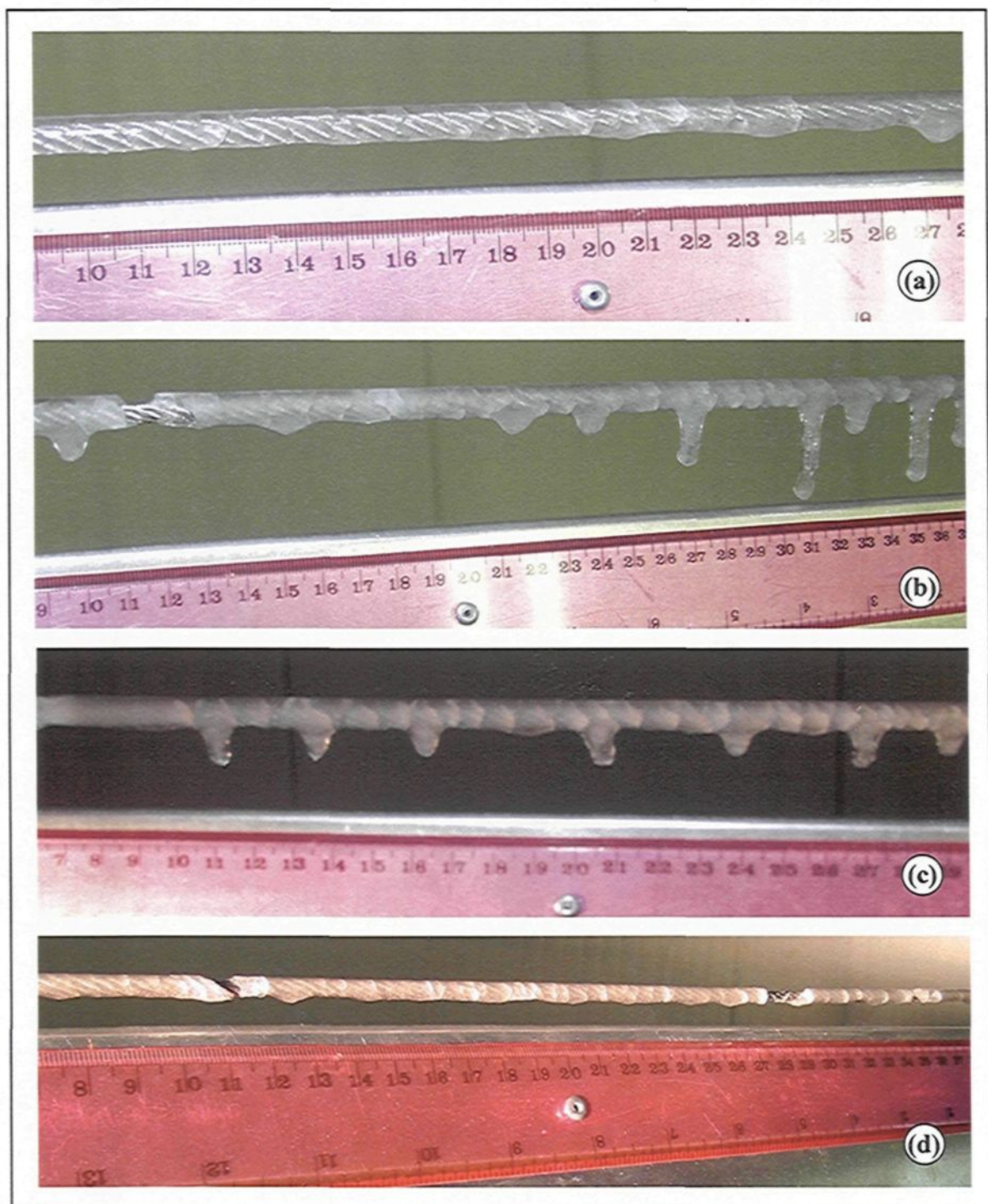
Figure 5.24 Section of the iced cable after the shock load showing the extensive cracking (detail H) for the (a) first, (b) second, (c) third and (d) forth ice-shedding scenarios studied

5.4 Conclusions

Comparisons of numerical and experimental results indicate that the numerical model accurately calculates the dynamic response of iced cables subjected to shock loads. However, it is also observed that the reduced-scale model possesses a high degree of sensitivity to the flexibility of the cable used. Nevertheless, it is believed that no such degree of sensitivity characterizes a real-scale line. Furthermore, even if the numerical model does not consider the adhesive strength of ice deposit that appears to be important in the reduced-scale model, it seems that until the transverse wave and its propagation along the span is maintained, i.e. the ice deposit is subjected to a high level of bending, the occurrence of the effective ice shedding from the cable is a reasonable assumption.

Numerical analysis of a real-scale line in Chapter 3 indicates that the shock point load applied to the cable generates a transverse wave in the cable that propagates along the span. Experimental studies performed by Hydro-Québec TransÉnergie on a real-scale test line [44] also show the same behavior of the iced cable subjected to a shock load derived from the DAC device. In this paper [44], it is stated that while the transverse wave travels along the span, ice accumulated on the cable breaks up into very small fragments. This ice-breaking action absorbs energy from the traveling wave and reduces its amplitude. The wave dies out when all the power conveyed by the wave has been absorbed by the ice. Therefore, it can be assumed that the numerical model presented can accurately model the dynamic effects of shock-load-induced ice shedding on

overhead lines when this transverse wave propagation is observed. However, experimental validation of the numerical model results on a real-scale line is paramount.

CHAPTER 6

APPLICATION OF THE NUMERICAL MODEL
TO REAL-SCALE LINES

6.1 Introduction

In this chapter, the numerical model presented in Chapter 3 and validated on a level single-span reduced-scale experimental model (Chapters 4 and 5) is applied to real-scale lines. Several ice-shedding scenarios are studied with variables including ice thickness, line parameters such as span length, cable tension and axial rigidity, and pulse-load characteristics in order to investigate how these variables affect the dynamic responses of iced cables subjected to mechanical shocks. The model is applied to a level single-span of a classical stranded steel ground wire (OHGW), an ACSR conductor and an optical ground wire (OPGW), all of them widely used on Hydro-Québec's high voltage transmission grid (Appendix C). Furthermore, a case with an extra-high strength overhead ground wire used for long-span lines (e.g. river crossing) is also studied.

6.2 Numerical modeling of ground wires

6.2.1 Introduction

In this section, the numerical model is applied to a level single-span of an overhead ground wire (Appendix C). A total of 14 ice-shedding scenarios are studied with variables

including line parameters such as the span length (100 m, 200 m and 300 m), initial cable tension and pulse-load characteristics (Fig. 6.1). The parameters of the line section with a span length of 100 m are adapted from [43, 44] as described in Chapter 3 (Table 3.1) in an attempt to compare numerical results and available real-scale experimental data [43, 44]. However, it should be noted that this can serve only as an illustration due to the lack of characterizing parameters of the real-scale test, such as the characteristics of the shock load, in particular. In addition, the available real-scale experimental results are scarce. The parameters of the other line sections (200 m and 300 m) are defined to provide the same initial sag-to-span ratio obtained for the line section with span length of 100 m. The pulse-load is applied at 3 m from the span extremity (Fig. 3.1) and is activated at time $t = 5\ s$ with the different triangular functions depicted in Figure 6.1. A time step of 0.1 ms is defined for the direct integration of the incremental equations of motion. An equivalent ice thickness of 12.7 mm is used throughout the simulations. Also, the static catenary profile and the iced static profile (initial state) are calculated in each case (Table 6.1).

6.2.2 Ice-shedding scenarios

A summary of the results of the numerical simulations is presented in Table 6.2, which lists the rate of ice shedding (RIS), i.e. the fraction of the ice shed in the span in %, the initial amplitude of the transverse wave (IWA) generated by the shock load, the maximum dynamic cable tension (MT) and the maximum cable jump at the mid span (MD). The maximum dynamic cable tension occurs at the support close to the excitation point. Zero displacement refers to the initial, fully iced cable configuration.
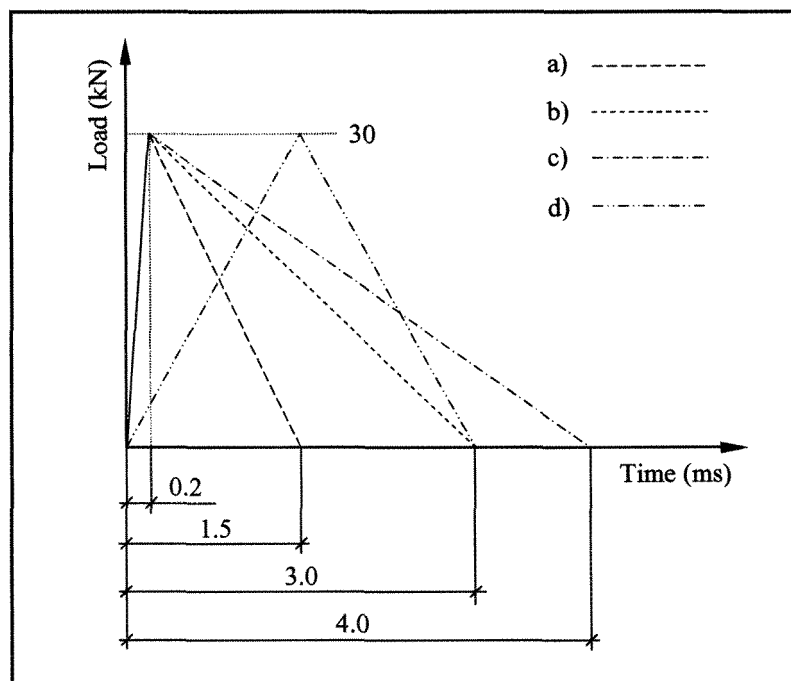
Figure 6.1 Pulse-load characteristics

Span (m)	Radial ice thickness (mm)	Bare catenary		Iced span	
		Tension (kN)	Max. sag (m)	Tension (kN)	Max. sag (m)
100	12.7 [0.912 kg/m]	12.5	0.75	16.7	1.23
200	12.7 [0.912 kg/m]	25.0	1.49	30.5	2.69
300	12.7 [0.912 kg/m]	37.5	2.24	43.8	4.22

[Mass per unit length]

Table 6.1 Static cable tensions and sags

Load case (Fig. 6.1)	100 m				200 m				300 m			
	RIS	IWA	MT	MD	RIS	IWA	MT	MD	RIS	IWA	MT	MD
a	100	0.08	76.2	0.56	85	0.07	81.9	0.66	75	0.05	86.1	0.61
b	100	0.16	98.0	0.82	100	0.13	99.1	1.19	100	0.10	105.8	1.45
c	100	0.22	104.6	0.99	100	0.17	106.7	1.22	100	0.13	110.9	1.71
d	100	0.17	105.2	0.80	100	0.13	106.4	1.23	100	0.10	121.9	1.56

RIS – rate of ice shedding (%)   IWA – initial amplitude of the transverse wave (m)
MT – maximum cable tension (kN)   MD – maximum mid-span displacement (m)

Table 6.2 Ice-shedding scenarios of the overhead ground wire

A) Effect of pulse-load characteristics

Simulation results indicate that the selection of the characteristics of the shock load is an important design issue since its energy content determines its capacity of removing the accreted ice from the ground wire. For a given maximum load, the smaller the duration of the pulse-load is (i.e. smaller energy content), the smaller the initial amplitude of the transverse wave, i.e. the percentage of ice shedding can diminish. Furthermore, in the case of identical pulse-load durations and magnitudes, i.e. identical energy content (cf. load cases *b* and *d*), the actual time history does not seem to have any effect on the effectiveness of ice removal or on the dynamic response of the iced cable. It is also interesting to note that partial ice shedding was obtained for the 200 m span with load case *a*, for instance. The transverse wave had sufficient energy to de-ice the cable until its mid span. From there, it was capable of causing only partial ice shedding. Selected time history results of a particular scenario with load case *b* were presented in Chapter 3.

B) Effect of pulse-load location along the span

In order to investigate the effect of shock load location along the span on the dynamic response, one case with a span length of 200 m and load case *a* is modeled where the pulse-load (Fig. 6.1a) is activated at the cable mid span. The rate of ice shedding (87%), the initial amplitude of the transverse wave (0.07 m) generated by the shock load, the maximum dynamic cable tension at the support (35.0 kN) and at the excitation point (59.7 kN), as well as the maximum cable jump at the mid span (0.76 m) are recorded (Fig. 6.2). These numerical results indicate that the location of the shock load along the span does not

contribute to the improvement of the rate of ice shedding. However, in this particular case, it results in a reduction of about 50% of the maximum cable tension at the support; but on the other hand, the cable mid-span displacement tends to increase by about 15% (cf. Fig. 6.2 and Fig. 6.3).
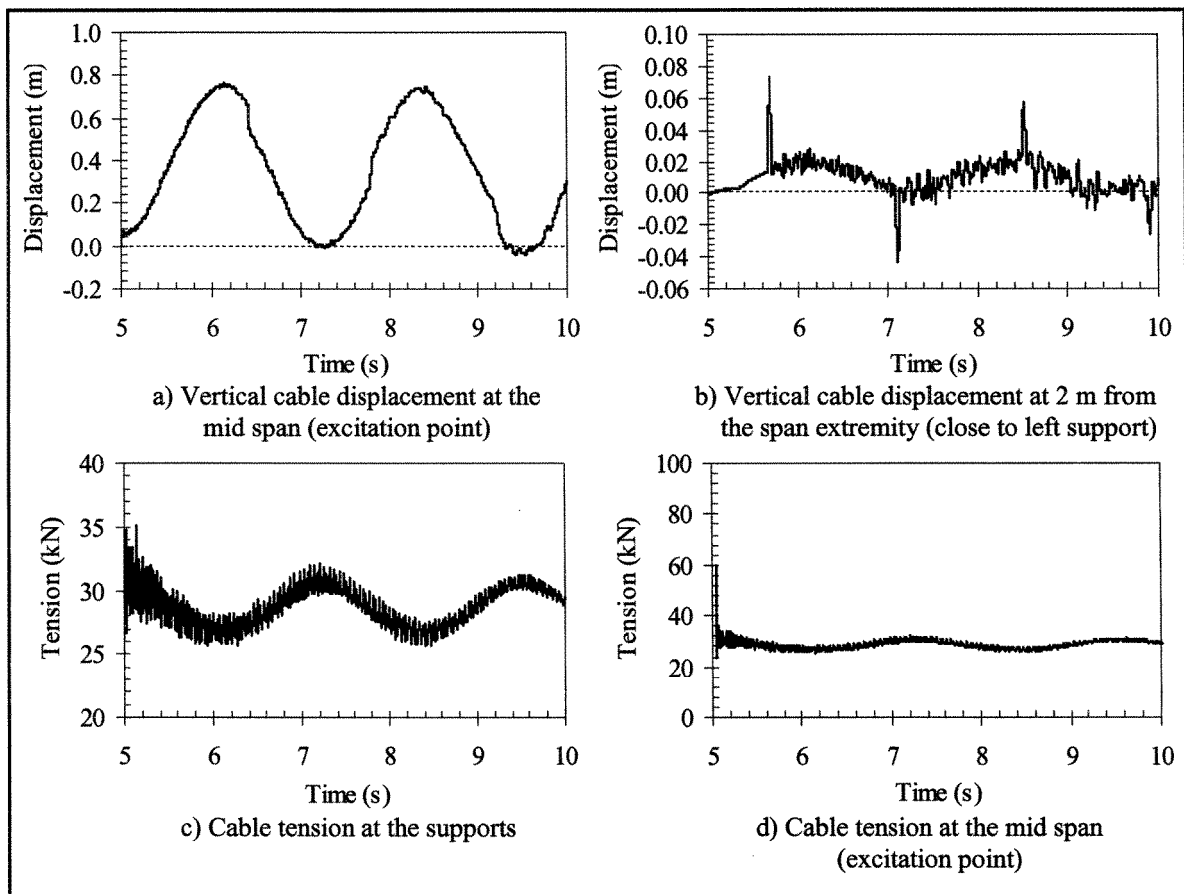
Figure 6.2 Transient dynamic response of the overhead ground wire to shock load applied at the mid span inducing ice shedding (span: 200m; load case *a*)
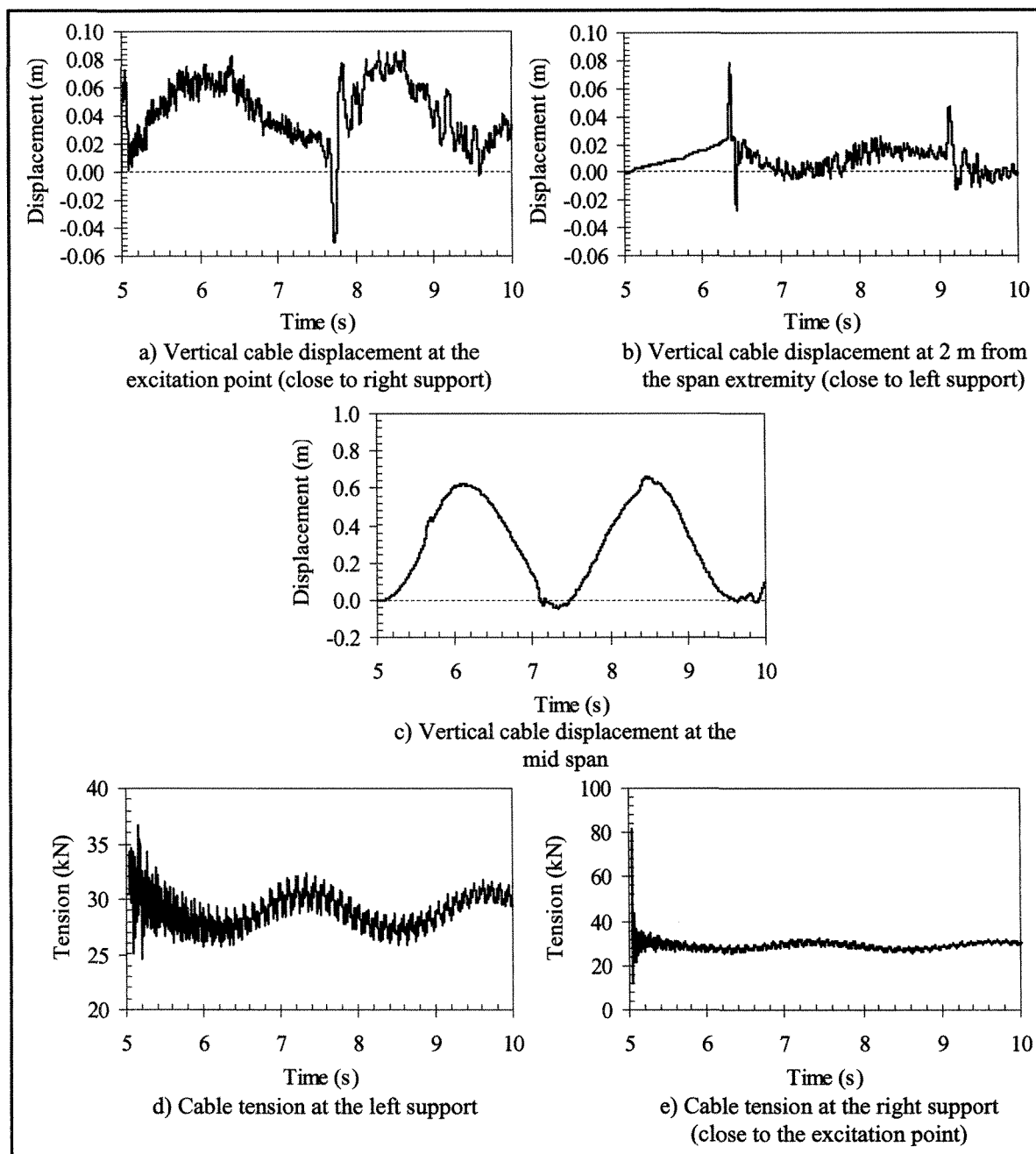
Figure 6.3 Transient dynamic response of the overhead ground wire to shock load applied
at 3 m from the span extremity inducing ice shedding (span: 200m; load case *a*)

C) Comparison of numerical results and real-scale experimental data

The initial amplitude of the transverse wave calculated by the model for the 100 m span when the pulse-load with the highest energy content (load case *c*) is applied to the cable is 0.22 m. However, in the experimental study [43], the approximate initial amplitude of the transverse wave is reported to be 0.35 m. This suggests that the force generated by the portable de-icing device [43, 44] and transmitted to the cable had higher energy content. In order to verify this assumption, a scenario with pulse-load characteristics depicted in Figure 6.4 is performed on the 100 m span. Figure 6.5 shows the time history results of the vertical displacement of the overhead ground wire at the mid span and at the excitation point. These results indicate that the initial amplitude of the transverse wave is 0.3 m, a value close to that obtained experimentally [43]. In addition, one can notice that the maximum vertical displacement of the overhead ground wire at the mid span approaches or even exceeds that of the instantaneous full-span ice shedding simulations (cf. Fig. 6.5 and Fig. 3.6).
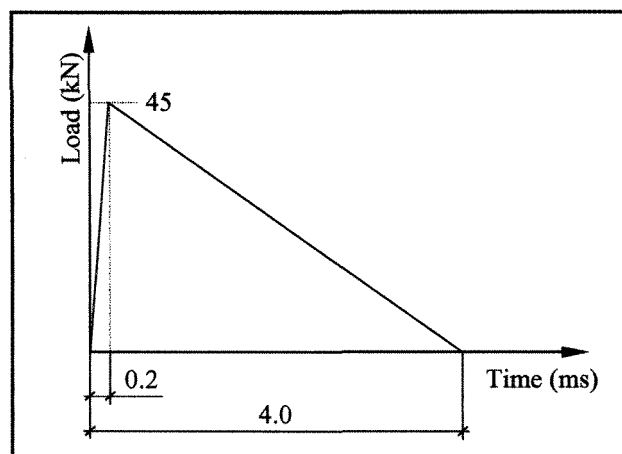
Figure 6.4 Pulse-load characteristics

a) Vertical displacement at the mid span   b) Vertical displacement at the excitation point
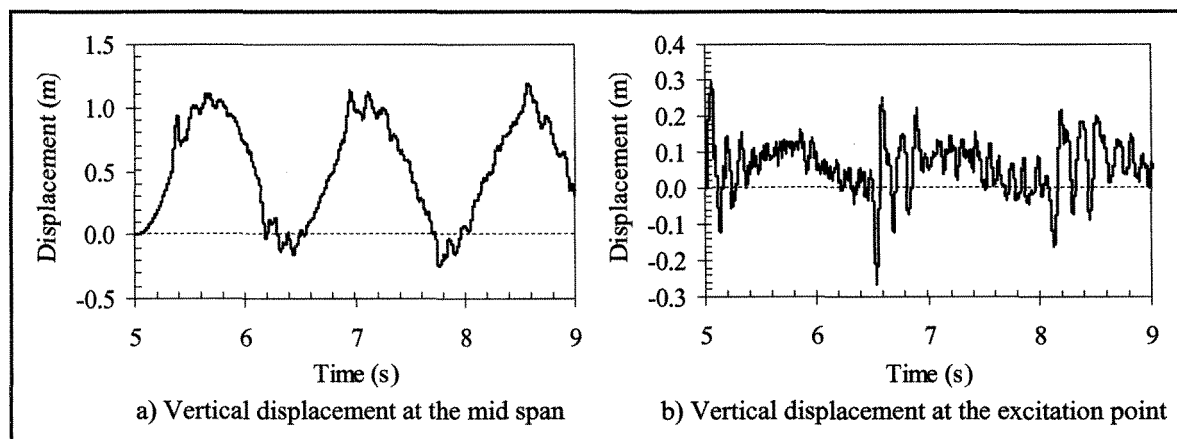
Figure 6.5 Vertical displacement of the overhead ground wire

In the experimental study [44], it was also reported that the longitudinal wave created by the DAC device propagates back and forth along the span at a speed of about 4 km/s, which is about 27 times faster than the transverse wave. This observation agrees with the dynamic analysis results where the approximate velocity calculated for the longitudinal and transverse waves is 3.6 km/s and 130 m/s, respectively. Furthermore, in the experimental study [43, 44], the power of the transverse wave as it travels along the span was measured using accelerometers. Values of 27.8, 18.3 and 12.0 kW were reported for the maximum instantaneous power conveyed by the transverse wave at ¼, ½ and ¾ of the span, respectively. The power conveyed by the wave can be expressed in terms of the cable tension, the speed of propagation of the transverse wave and the transversal velocity of the cable as described in Appendix A. For comparison purposes, values of the transversal velocity of the cable obtained from the simulation at ¼, ½ and ¾ of the span are recorded as shown in Figure 6.6. These time histories indicate the propagation of the transverse

wave, i.e. the propagation and attenuation of the power conveyed by the wave, along the span. Values of the maximum instantaneous power calculated are 81.2, 48.4 and 27.5 kW respectively at ¼, ½ and ¾ of the span. It is interesting to note that these values do not agree with those obtained experimentally [43], but the attenuations of the maximum instantaneous power conveyed by the transverse wave along the span are proportional (approximately 3:1). Therefore, it can be expected that the transversal velocity of the ground wire obtained experimentally is less than that obtained numerically. For instance, it is plausible that a shock load with longer duration but lower amplitude (i.e. same energy content) might have been applied to the cable during the experiments.
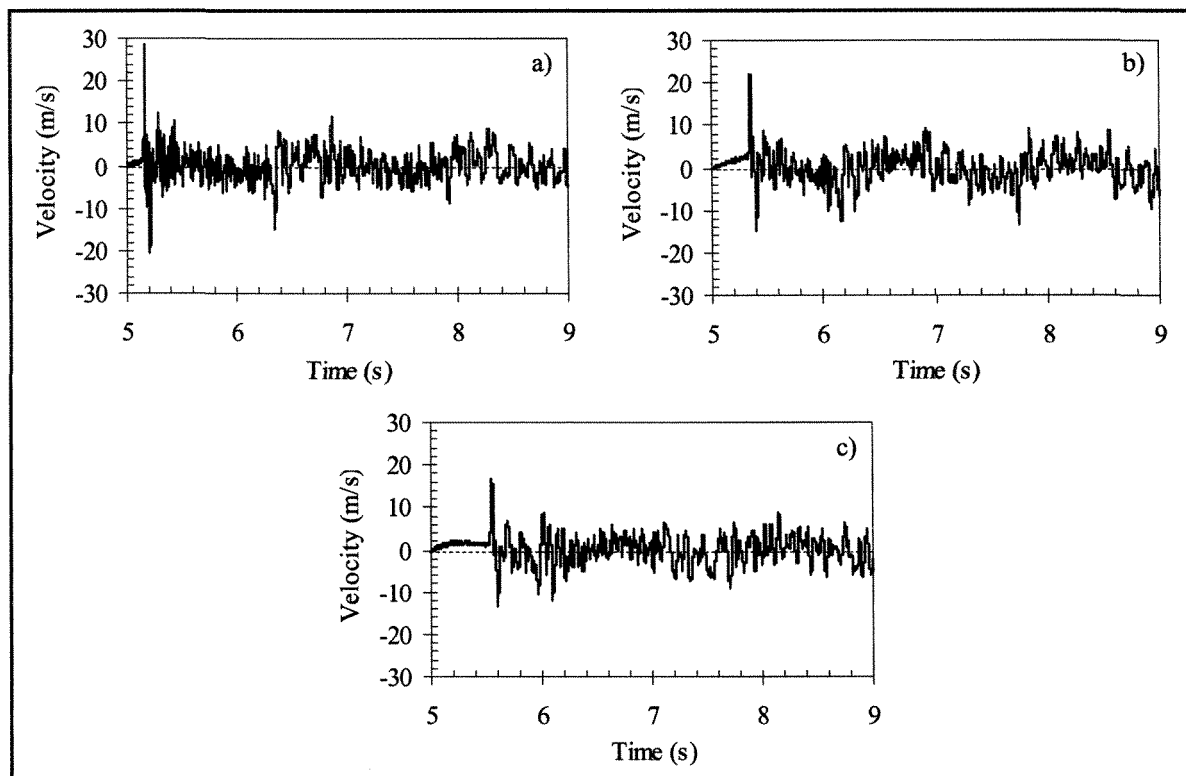
Figure 6.6 Transversal velocity of the ground wire at (a) ¼, (b) ½ and (c) ¾ of the span

6.3 Numerical modeling of conductors

6.3.1 Introduction

In this section, the numerical model proposed to study ice shedding is applied to a level single-span of an ACSR line conductor (Appendix C). A total of 27 ice-shedding scenarios are studied with variables including ice thickness, span length (100 m, 200 m and 300 m) and pulse-load characteristics. In the previous section, an equivalent ice thickness of 12.7 mm was modeled, whereas in this section, the effectiveness of ice removal in terms of the ice thickness is investigated using three values of equivalent ice thickness of 10, 25 and 38 mm. Furthermore, the different pulse-load characteristics activated at the mid span are represented by the variation of load amplitude (30 kN, 45 kN and 60 kN) while the pulse duration and its time history are kept constant (Fig. 6.7). For all cases the static catenary profile and the iced static profile are calculated (Table 6.3).
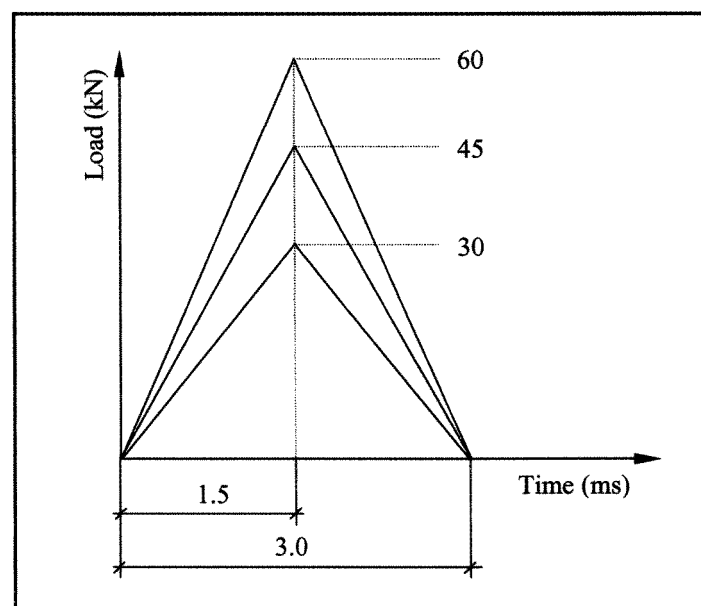
Figure 6.7 Pulse-load characteristics

6.3.2 Eigenvalue analysis

For mesh validation purposes, several natural frequencies and mode shape analyses are conducted on various iced span models with parameters summarized in Table 6.4 prior to the transient dynamic analysis. The calculated in-plane mode shapes and corresponding natural frequencies are identical in all models (Table 6.5), with the exception mentioned in Chapter 3 for symmetric modes of the increased-density truss model and Irvine's ideal catenary that are not influenced by the bending rigidity of the ice deposit.

Span (m)	Radial ice thickness (mm)	Bare catenary		Iced span	
		Tension (kN)	Max. sag (m)	Tension (kN)	Max. sag (m)
100	10 [1.07 kg/m]	3.8	5.02	6.4	5.05
	25 [3.73 kg/m]	3.8	5.02	12.9	5.12
	38 [7.07 kg/m]	3.8	5.02	20.7	5.21
200	10 [1.07 kg/m]	7.6	10.04	12.8	10.16
	25 [3.73 kg/m]	7.6	10.04	25.3	10.45
	38 [7.07 kg/m]	7.6	10.04	40.1	10.78
300	10 [1.07 kg/m]	11.4	15.05	19.1	15.33
	25 [3.73 kg/m]	11.4	15.05	37.3	15.95
	38 [7.07 kg/m]	11.4	15.05	58.5	16.65

[Mass per unit length]

Table 6.3 Static cable tensions and sags (ACSR conductor)

Line parameters		Ice parameters	
Span length (m)	300	Type	Glaze
Initial sag-to-span ratio (%)	5	Density (kg/m^3)	900
Cable axial rigidity (kN)	31,374.3	Radial ice thickness (mm)	25

Table 6.4 Parameters of the case study (ACSR conductor)

Mode	Truss Herm. - beam (Hz)	Truss Iso - beam (Hz)	Truss Pipe - beam (Hz)	Increased - density truss (Hz)	Irvine's theory (Hz)
1st symmetric	0.39	0.39	0.39	0.38	0.38
1st asymmetric	0.27	0.27	0.27	0.27	0.27
2nd symmetric	0.62	0.62	0.62	0.54	0.55
2nd asymmetric	0.55	0.55	0.55	0.55	0.55

Table 6.5 Natural frequencies of the corresponding 1st and 2nd in-plane modes obtained for different iced cable models (case study: Table 6.4)

6.3.3 Ice-shedding scenarios

A summary of the results of the numerical simulations is presented in Table 6.6, which lists the rate of ice shedding (RIS), i.e. the fraction of the ice shed in the span in %, the initial amplitude of the transverse wave (IWA) generated by the shock load, the maximum dynamic cable tension at the excitation point (MT) and at the support (MTS), as well as the maximum cable jump at the mid span (MD). Zero displacement again refers to the initial, fully iced cable configuration.

Simulation results indicate that a sudden load with amplitude of 30 kN is sufficient to fully remove thin (10 mm) accreted ice on a 300 m span. As expected, the larger the ice thickness and span length are, the larger the amplitude (i.e. larger energy content) of the shock load necessary to shed the ice. However, in this numerical study, a load of 60 kN generated additional tension in the cable at the excitation point that exceeded the rated tensile strength of the cable, which is unrealistic. Therefore, to avoid damaging the cable, it may be necessary in practice to apply successive lower amplitude shock loads at a given point along the span or at two or more points. To verify this scenario, a hypothetical

example was simulated for a 300 m span with 38 mm radial ice thickness using two synchronous shock loads with amplitude of 45 kN located at about one quarter span length from both supports. The results have confirmed that this approach may be safe and effective: the ice shedding percentage increased from 20% (with one shock load at mid span) to about 45% without overstressing the cable and/or the structure.

6.3.4 Time history analysis results

Figure 6.8 presents selected time histories of vertical cable jumps at mid span and cable tensions for the case study (Table 6.4) where 37% of the ice sheds (Figs. 6.8a, b and d) and for 90% shedding (Fig. 6.8c). The shock load applied to the cable at the mid span generates two transverse waves that propagate along the span at an approximate average speed of 90 m/s and de-ice the cable until all the power conveyed by the wave is absorbed. Besides the transverse waves, the shock load also generates longitudinal waves that propagate back and forth along the span at an approximate speed of 5 km/s. The high frequency oscillations of the cable tension (evaluated at about 8 Hz) correspond to this fundamental longitudinal (axial) vibration of the iced cable.

Span (m)	Load (kN)	Radial ice thickness															
		10 mm					25 mm					38 mm				
		RIS	IWA	MT	MTS	MD	RIS	IWA	MT	MTS	MD	RIS	IWA	MT	MTS	MD
100	30	100	0.19	86.6	66.9	0.70	74	0.07	66.4	29.2	0.47	40	0.07	56.8	41.1	0.27
	45	100	0.24	106.0	100.0	0.78	99	0.09	92.8	28.9	0.61	58	0.08	89.7	41.6	0.43
	60	100	0.27	132.5	142.3	1.29	99	0.12	130.5	32.2	0.87	77	0.09	116.3	43.2	0.56
200	30	100	0.15	88.1	28.3	0.42	47	0.07	70.4	35.8	0.52	17	0.06	67.5	57.1	0.17
	45	100	0.17	107.3	64.0	0.68	77	0.08	99.4	36.8	0.73	41	0.07	97.6	55.8	0.39
	60	100	0.20	133.7	47.3	0.93	100	0.09	134.3	39.8	0.95	50	0.08	124.5	59.5	0.77
300	30	99	0.10	76.4	28.3	0.49	37	0.06	77.7	48.9	0.57	8	0.05	81.9	76.8	0.15
	45	100	0.16	108.7	27.8	0.58	56	0.07	105.5	51.4	0.94	20	0.06	108.9	69.0	0.35
	60	100	0.24	131.4	39.9	0.83	90	0.08	138.3	51.1	1.17	30	0.07	134.9	74.0	0.58

RIS – rate of ice shedding (%); IWA – initial amplitude of the transverse wave (m); MT – maximum cable tension at the excitation point (kN) MTS – maximum cable tension at the support (kN); MD – maximum mid-span displacement (m)

Table 6.6 Ice-shedding scenarios of the overhead ACSR conductor

6.4 Numerical modeling of optical ground wires

6.4.1 Introduction

In this section, the numerical model is applied to a level single-span of an overhead optical ground wire (OPGW) used on 6000 km of Hydro-Québec's transmission network [23] (Appendix C). Only two ice-shedding scenarios are studied with parameters summarized in Table 6.7. In the first stage of numerical analysis, the pulse-load with an amplitude of 45 kN is applied to the cable at 3 m from the span extremity and activated at time $t = 5\ s$ for 10 time steps of 0.3 ms with the triangular pulse function depicted in Figure 6.7. In the second scenario, a pulse-load with an amplitude of 45 kN is applied to the cable, again, at 3 m from the span extremity and activated at time $t = 5\ s$ for 20 time steps of 0.2 ms with the triangular pulse function depicted in Figure 6.4 (i.e. a load with higher energy content). The static catenary profile and the iced static profile are calculated and summarized in Table 6.8. However, it should be noted that whether the shock load applied to the OPGW damages the optical fibers embedded in the OPGW is beyond the scope of this study.

Line parameters		Ice parameters	
Span length (m)	300	Type	Glaze
Initial sag-to-span ratio (%)	5	Density (kg/m^3)	900
Cable axial rigidity (kN)	29,435.0	Radial ice thickness (mm)	25

Table 6.7 Parameters of the case study (OPGW)

Span (m)	Radial ice thickness (mm)	Bare catenary		Iced span	
		Tension (kN)	Max. sag (m)	Tension (kN)	Max. sag (m)
300	25 [3.386 kg/m]	9.5	15.05	33.2	15.93

[Mass per unit length]

Table 6.8 Static cable tensions and sags (OPGW)

a) Vertical displacement at mid span due to shock load causing 37% ice shedding (span: 300m; ice thickness: 25mm; load: 30kN)

b) Cable tension at the support due to shock load causing 37% ice shedding (span: 300m; ice thickness: 25mm; load: 30kN)

c) Vertical displacement at mid span due to shock load causing 90% ice shedding (span: 300m; ice thickness: 25mm; load: 60kN)

d) Cable tension at mid span due to shock load causing 37% ice shedding (span: 300m; ice thickness: 25mm; load: 30kN)

Figure 6.8 Transient dynamic response of the overhead conductor to shock-load-induced ice shedding

6.4.2 Eigenvalue analysis

The in-plane mode shapes and corresponding natural frequencies obtained for the various iced span models of the case study (Table 6.7) are identical in all models with the exception mentioned in Chapter 3 (Table 6.9).

Mode	Truss Herm. - beam (Hz)	Truss Iso - beam (Hz)	Truss Pipe - beam (Hz)	Increased - density truss (Hz)	Irvine's theory (Hz)
1st symmetric	0.39	0.39	0.39	0.38	0.38
1st asymmetric	0.27	0.27	0.27	0.27	0.27
2nd symmetric	0.66	0.66	0.66	0.56	0.56
2nd asymmetric	0.55	0.55	0.55	0.55	0.55

Table 6.9 Natural frequencies of the corresponding 1st and 2nd in-plane modes obtained for different iced cable models (case study: Table 6.7)

6.4.3 Transient dynamic analysis

A summary of the results of the numerical simulations is presented in Table 6.10. The model results indicate that the shock load (Fig. 6.7) applied to the cable generates a transverse wave with amplitude of 0.11 m that propagates along the span at an approximate average speed of 85 m/s and fully de-ices the first 55 m of the cable. From there, it is capable of causing only partial ice shedding, while the shock load with the higher energy content (Fig. 6.4) is capable of triggering full-span ice shedding. Figure 6.9 shows selected time history results of cable vertical displacements and tensions for the case when full-span ice shedding is triggered. Figures 6.9a and b, which show the vertical displacement of the

iced cable both at the excitation point (close to right support) and at a point close to the left support, illustrate the transverse wave propagation. The high frequency content of the cable tensions (Figs 6.9d and e) (evaluated at about 5 Hz) indicates the propagation of the generated longitudinal wave back and forth along the span.

Span (m)	Radial ice thickness (mm)	Pulse-load Figure 6.7				Pulse-load Figure 6.4			
		RIS	IWA	MT	MD	RIS	IWA	MT	MD
300	25	56	0.11	140.0	0.40	100	0.13	145.0	0.62

RIS – rate of ice shedding (%)   IWA – initial amplitude of the transverse wave (m)
MT – maximum cable tension (kN)   MD – maximum mid-span displacement (m)

Table 6.10 Ice-shedding scenarios of the overhead optical ground wire

a) Vertical cable displacement at the excitation point (close to right support)

b) Vertical cable displacement at 2 m from the span extremity (close to left support)

c) Vertical cable displacement at the mid span

d) Cable tension at the left support

e) Cable tension at the right support (close to the excitation point)

Figure 6.9 Transient dynamic response of the overhead optical ground wire (OPGW) to shock-load-induced ice shedding

6.5 Long-span lines: river crossing

6.5.1 Introduction

Overhead line crossings of rivers and straits with spans ranging up to 2 km are often used. Such long spans are expensive to build and operate, and their construction requires special considerations. Due to wind-induced vibrations of the conductors, it is necessary either to install very large clearances or to mount insulators between the phase conductors within the span to prevent the conductors from striking against each other during strong winds. This clearance problem is even more pronounced when the large span is also subjected to atmospheric icing. Furthermore, arbitrarily tall pylons at either end of the crossing cannot be built, and a considerable clearance (headway) under the line must be provided for ship navigation if relevant. Therefore high mechanical tensions are experienced in such long spans requiring special cable constructions.

In this section, the numerical model is applied to a long-span overhead ground wire (Appendix C) used for crossing the St-Lawrence River in the Québec City region. Parameters of the line section as provided by Hydro-Québec are summarized in Table 6.11. Two ice-shedding scenarios are studied with two different pulse-load characteristics as depicted in Figure 6.10 (100 kN and 150 kN). In both scenarios, the pulse-load is applied to the cable at 3 m from the span extremity and activated at time $t = 5\ s$ for 10 time steps of 0.3 ms. The calculated static bare catenary profile and the iced static profile are summarized in Table 6.12.
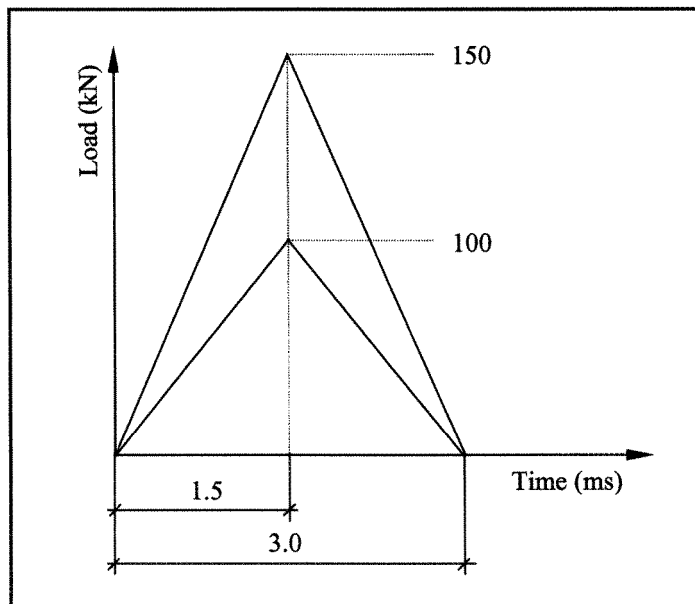
Figure 6.10 Pulse-load characteristics

Line parameters		Ice parameters	
Span length (m)	1585	Type	Glaze
Initial horizontal tension (kN)	167.16	Density (kg/m^3)	900
Cable axial rigidity (kN)	73,545.00	Radial ice thickness (mm)	10

Table 6.11 Parameters of the long-span line section

Span (m)	Radial ice thickness (mm)	Bare catenary		Iced span	
		Tension (kN)	Max. sag (m)	Tension (kN)	Max. sag (m)
1585	10 [1.091 kg/m]	167.16	73.17	207.59	76.49

[Mass per unit length]

Table 6.12 Static cable tensions and sags

6.5.2 Eigenvalue analysis

The in-plane mode shapes and corresponding natural frequencies obtained for the various iced span models of the case study (Table 6.11) are identical in all models with no exception (Table 6.13).

Mode	Truss Herm. - beam (Hz)	Truss Iso - beam (Hz)	Truss Pipe - beam (Hz)	Increased - density truss (Hz)	Irvine's theory (Hz)
1st symmetric	0.14	0.14	0.14	0.14	0.14
1st asymmetric	0.12	0.12	0.12	0.12	0.12
2nd symmetric	0.20	0.20	0.20	0.20	0.20
2nd asymmetric	0.25	0.25	0.25	0.25	0.25

Table 6.13 Natural frequencies of the corresponding 1st and 2nd in-plane modes obtained for different iced cable models (case study: Table 6.11)

6.5.3 Transient dynamic analysis

A summary of the results of the numerical simulations is presented in Table 6.14. It shows that a shock load with amplitude of 100 kN is capable of causing only partial ice shedding, while the load with amplitude of 150 kN triggers full-span shedding. Time history results of the cable vertical displacement obtained at the excitation point (Fig. 6.11a), at 10 m from the other span extremity (Fig. 6.11b) and at the mid span (Fig. 6.11c) indicate the propagation of the transverse wave at an approximate average speed of 200 m/s. The high frequency content of the time histories of cable tensions (Figs 6.11d and e) (evaluated at about 1.3 Hz) indicates the propagation of the longitudinal wave back and forth along the span at an approximate speed of 4.1 km/s.
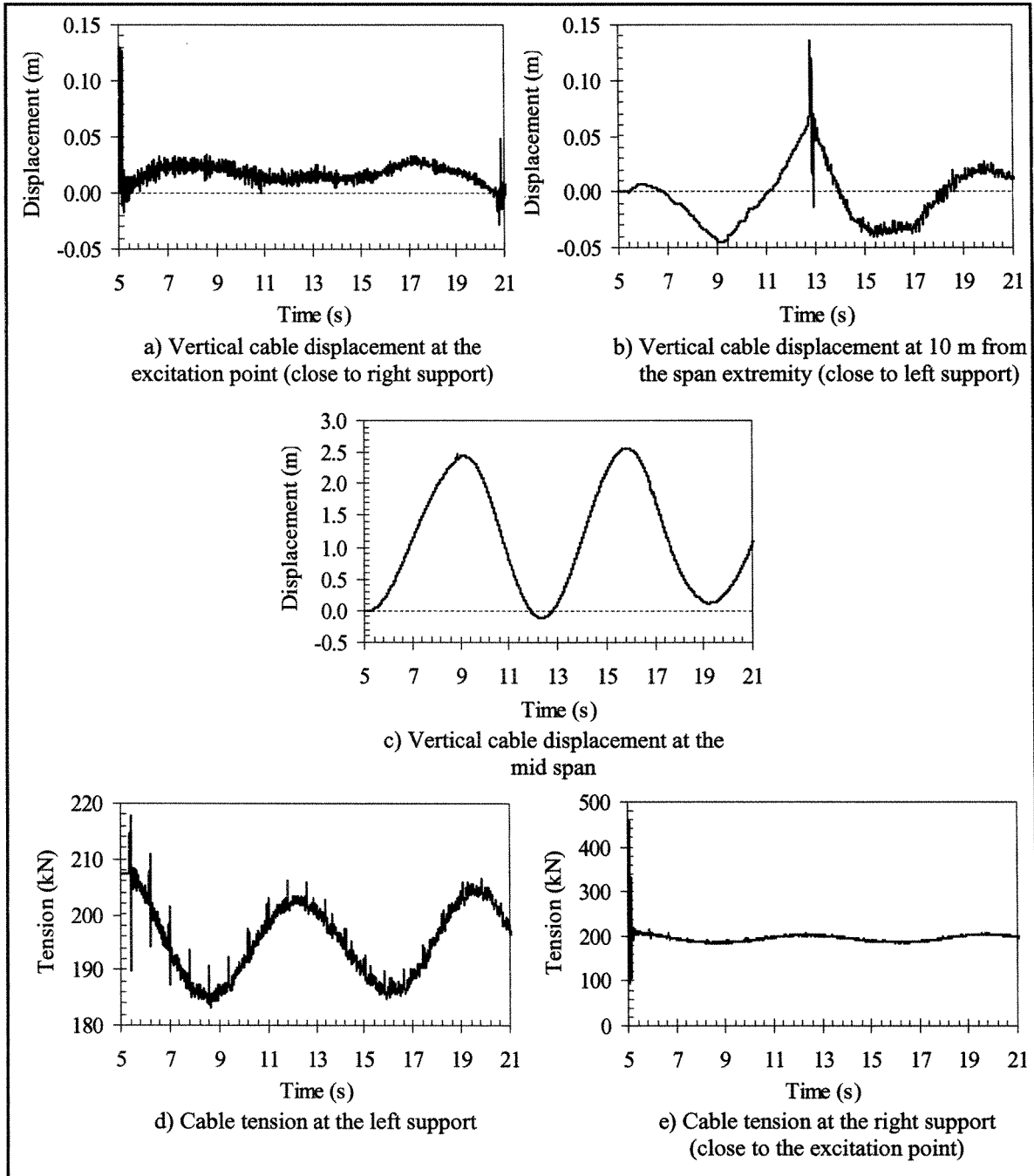
Figure 6.11 Transient dynamic response of the long-span overhead ground wire
to shock-load-induced full-span ice shedding

Span	Radial ice thickness	100 kN				150 kN			
(m)	(mm)	RIS	IWA	MT	MD	RIS	IWA	MT	MD
1585	10	62	0.08	330	0.52	100	0.13	458	2.48

RIS – rate of ice shedding (%)   IWA – initial amplitude of the transverse wave (m)
MT – maximum cable tension (kN)   MD – maximum mid-span displacement (m)

Table 6.14 Ice-shedding scenarios of the long-span overhead ground wire

6.6 Conclusions

Numerical studies have shown that it is feasible to model the effects of shock-load-induced ice shedding on single-span real-scale overhead lines. The proposed model was successfully applied to a level single-span of four cable types: a usual stranded steel ground wire, an ACSR 54/7 conductor, an optical ground wire (OPGW) and an extra-high strength ground wire used for long-span lines (e.g. river crossing). In addition, the ice-shedding scenarios studied showed that various line section geometries could also be easily investigated using the model. Simulation results indicate that the energy content of the shock load capable of removing the accreted ice from the cable is an important design issue. The larger the ice thickness and span length are, the larger the energy content of the shock load necessary to shed the ice. However, the increase of the energy content of the shock load is limited by the resistance of the cable and its supporting structure.

CHAPTER 7

COMPLEMENTARY NUMERICAL ANALYSES

7.1 Introduction

In this chapter, complementary numerical analyses of alternative modeling approaches of ice accretion, as well as the effect of different numerical methods on the dynamic response are summarized.

7.2 Alternative modeling approaches of ice accretion

7.2.1 Introduction

Two alternative modeling approaches of ice were also found adequate to represent the accreted ice on the cable in ADINA, using the 2-D plane stress iso-beam and the pipe-beam. The modeling considerations described in Chapter 3 for the 3-D iso-beam ice element are applied here for both the 2-D plane stress iso-beam and the pipe-beam ice representations. All the ice-shedding scenarios of the overhead ground wire (OHGW) and the ACSR conductor discussed in Chapter 6 are repeated using these two alternative ice modeling approaches.

7.2.2 Ice-shedding analysis with various line parameters

A summary of the results of the numerical simulations is presented in Table 7.1 and Table 7.2 where zero displacement refers to the initial fully iced configuration. These results show that for the three ice models (3-D iso-beam, 2-D plane stress iso-beam and pipe-beam) the percentage of ice shedding from the line section and the initial amplitude of the transverse wave are practically identical. The maximum cable tensions calculated by the three ice models are in good agreement despite the fact that a difference of about 10% can be observed in some results (Table 7.3 and Table 7.4). However, the time histories of these cable tensions are very similar (Fig. 7.1). On the other hand, the model with the 2-D plane stress iso-beam representation tends to underestimate the maximum cable jump at the mid span in some cases when partial ice shedding takes place. In most cases, it occurs when the cable jump at the mid span is small and therefore the calculated difference is only a few cm. However, a thorough investigation of this discrepancy was carried out as described in the next section. The mid-span displacement results obtained by the pipe-beam ice model are consistent with those obtained by the 3-D iso-beam ice model.
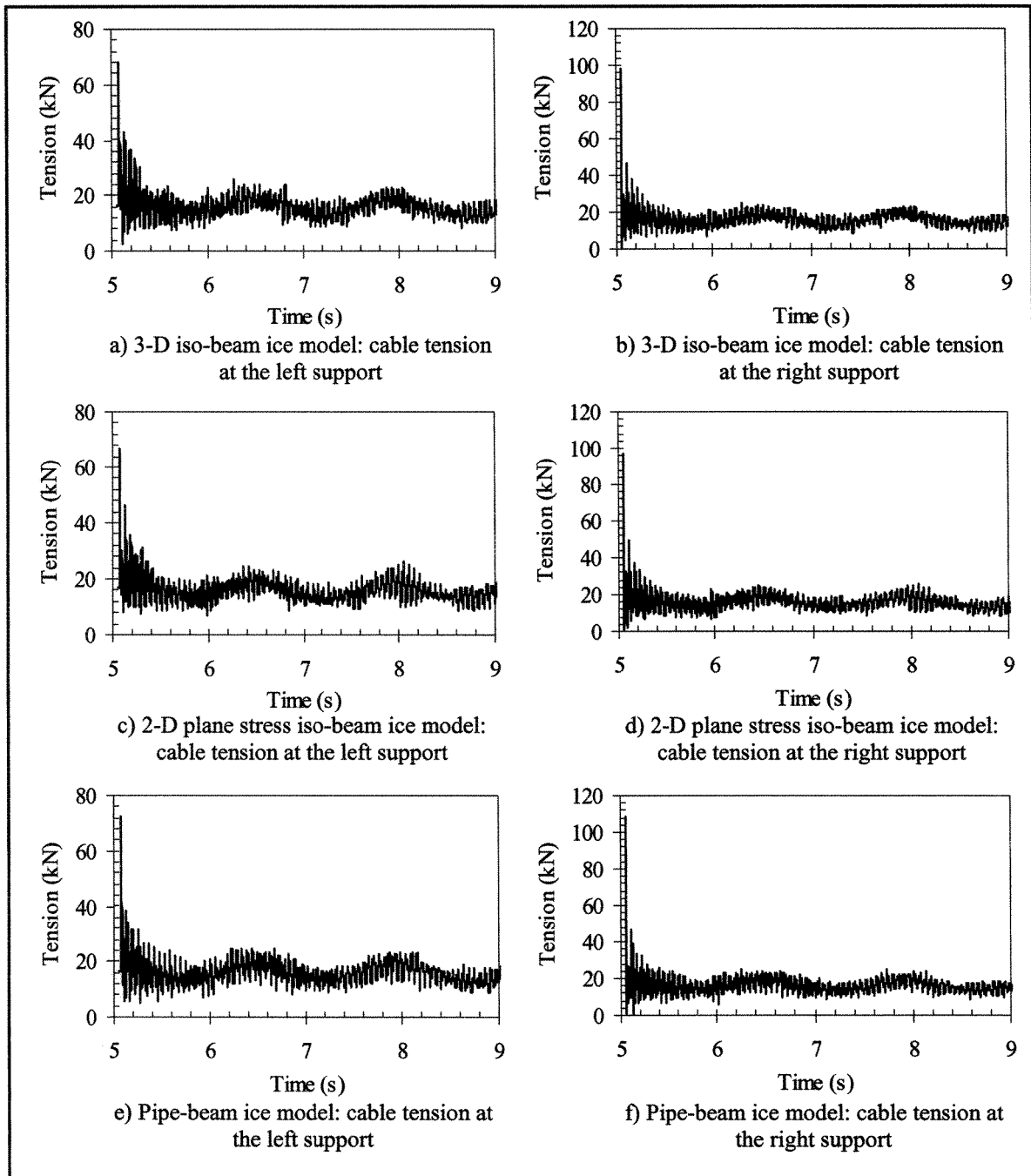
Figure 7.1 Time histories of the overhead ground wire tensions obtained with the three ice models
(Case study with load case *b*)

Ice element	Load case (Fig. 6.1)	100 m				200 m				300 m			
		RIS	IWA	MT	MD	RIS	IWA	MT	MD	RIS	IWA	MT	MD
3-D iso-beam	a	100	0.08	76.2	0.56	85	0.07	81.9	0.66	75	0.05	86.1	0.61
	b	100	0.16	98.0	0.82	100	0.13	99.1	1.19	100	0.10	105.8	1.45
	c	100	0.22	104.6	0.99	100	0.17	106.7	1.22	100	0.13	110.9	1.71
	d	100	0.17	105.2	0.80	100	0.13	106.4	1.23	100	0.10	121.9	1.56
2-D plane stress iso-beam	a	100	0.08	73.3	0.59	85	0.07	79.2	0.60	60	0.05	84.9	0.29
	b	100	0.17	97.0	0.80	100	0.13	100.9	1.19	100	0.10	107.3	1.28
	c	100	0.21	103.3	0.98	100	0.17	104.8	1.33	100	0.14	109.7	1.50
	d	100	0.17	102.1	0.80	100	0.14	102.7	1.17	100	0.10	104.2	1.34
Pipe-beam	a	100	0.08	82.8	0.44	85	0.07	80.0	0.67	75	0.05	84.3	0.70
	b	100	0.16	108.1	0.81	100	0.13	101.4	1.05	100	0.10	102.9	1.54
	c	100	0.21	114.4	0.93	100	0.17	106.0	1.17	100	0.13	107.3	1.73
	d	100	0.17	98.1	0.76	100	0.13	99.8	1.15	100	0.10	121.9	1.67

RIS – rate of ice shedding (%); IWA – initial amplitude of the transverse wave (m); MT – maximum cable tension (kN); MD – maximum mid-span displacement (m)

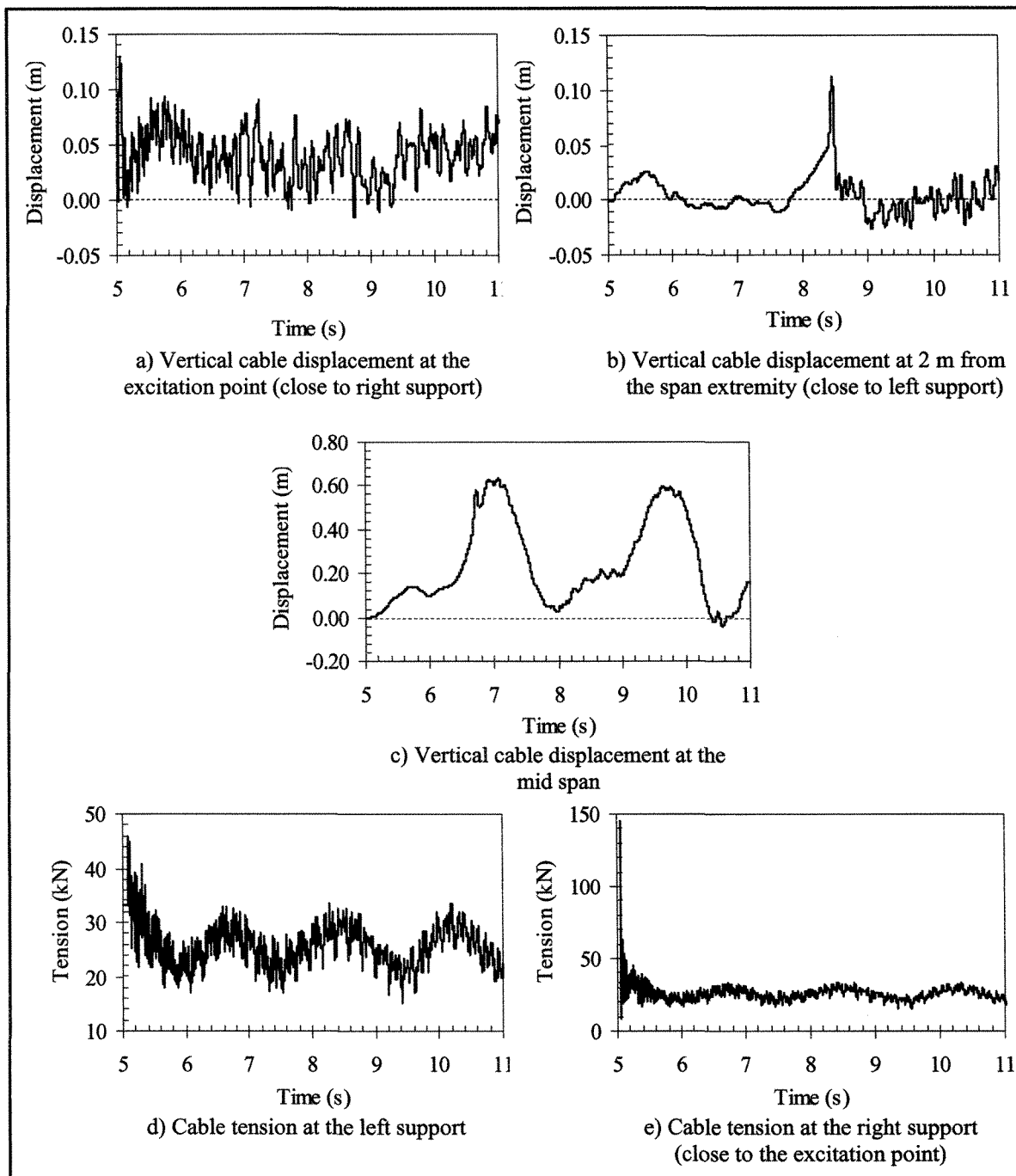**Table 7.1** Ice-shedding scenarios of the overhead ground wire (OHGW) using the
3-D iso-beam, 2-D plane stress iso-beam and the pipe-beam
modeling approaches of ice accretion

Ice element	Span (m)	Load (kN)	Radial ice thickness 10 mm					25 mm					38 mm				
			RIS	IWA	MT	MTS	MD	RIS	IWA	MT	MTS	MD	RIS	IWA	MT	MTS	MD
3-D iso-beam	100	30	100	0.19	86.6	66.9	0.70	74	0.07	66.4	29.2	0.47	40	0.07	56.8	41.1	0.27
		45	100	0.24	106.0	100.0	0.78	99	0.09	92.8	28.9	0.61	58	0.08	89.7	41.6	0.43
		60	100	0.27	132.5	142.3	1.29	99	0.12	130.5	32.2	0.87	77	0.09	116.3	43.2	0.56
	200	30	100	0.15	88.1	28.3	0.42	47	0.07	70.4	35.8	0.52	17	0.06	67.5	57.1	0.17
		45	100	0.17	107.3	64.0	0.68	77	0.08	99.4	36.8	0.73	41	0.07	97.6	55.8	0.39
		60	100	0.20	133.7	47.3	0.93	100	0.09	134.3	39.8	0.95	50	0.08	124.5	59.5	0.77
	300	30	99	0.10	76.4	28.3	0.49	37	0.06	77.7	48.9	0.57	8	0.05	81.9	76.8	0.15
		45	100	0.16	108.7	27.8	0.58	56	0.07	105.5	51.4	0.94	20	0.06	108.9	69.0	0.35
		60	100	0.24	131.4	39.9	0.83	90	0.08	138.3	51.1	1.17	30	0.07	134.9	74.0	0.58
2-D plane stress iso-beam	100	30	100	0.19	76.4	65.2	0.71	70	0.07	62.3	30.0	0.54	20	0.06	58.8	42.8	0.17
		45	100	0.24	105.9	99.5	0.87	99	0.09	93.3	27.8	0.68	60	0.07	92.4	42.8	0.41
		60	100	0.26	142.0	142.0	1.21	99	0.12	130.6	32.6	0.69	85	0.09	114.5	40.9	0.65
	200	30	100	0.15	77.8	23.3	0.49	47	0.07	73.1	36.1	0.41	15	0.05	70.0	56.8	0.22
		45	100	0.17	107.0	64.8	0.75	72	0.08	98.8	40.7	0.68	35	0.07	97.2	57.0	0.35
		60	100	0.20	133.6	59.5	0.99	100	0.09	134.3	38.2	0.90	47	0.08	122.9	57.7	0.75
	300	30	100	0.10	76.6	29.1	0.48	34	0.05	78.9	49.1	0.42	8	0.04	83.9	76.4	0.12
		45	100	0.16	108.8	29.7	0.61	52	0.07	104.8	51.9	0.87	18	0.06	107.5	72.4	0.37
		60	100	0.23	131.8	40.1	0.80	94	0.08	138.3	54.1	1.11	30	0.07	132.5	70.5	0.55

RIS – rate of ice shedding (%); IWA – initial amplitude of the transverse wave (m); MT – maximum cable tension at the excitation point (kN); MTS – maximum cable tension at the support (kN); MD – maximum mid-span displacement (m)

Table 7.2 Ice-shedding scenarios of the ACSR overhead conductor using the 3-D iso-beam and 2-D plane stress iso-beam modeling approaches of ice accretion

Ice element	Load case (Fig. 6.1)	100 m				200 m				300 m			
		RIS	IWA	MT	MD	RIS	IWA	MT	MD	RIS	IWA	MT	MD
2-D plane stress iso-beam	a	0%	0%	4%	7%	0%	0%	3%	10%	20%	8%	1%	53%
	b	0%	2%	1%	2%	0%	5%	2%	0%	0%	2%	1%	11%
	c	0%	5%	1%	0%	0%	2%	2%	9%	0%	5%	1%	12%
	d	0%	2%	3%	0%	0%	2%	4%	5%	0%	2%	15%	15%
Pipe-beam	a	0%	1%	9%	21%	0%	0%	2%	1%	0%	4%	2%	15%
	b	0%	1%	10%	1%	0%	5%	2%	12%	0%	2%	3%	6%
	c	0%	6%	9%	6%	0%	2%	1%	4%	0%	3%	3%	1%
	d	0%	2%	7%	5%	0%	1%	6%	6%	0%	0%	0%	7%

RIS – rate of ice shedding (%); IWA – initial amplitude of the transverse wave (m); MT – maximum cable tension (kN); MD – maximum mid-span displacement (m)

Table 7.3 Relative errors between simulation results of the overhead ground wire obtained by the 2-D plane stress iso-beam, the pipe-beam and the 3-D iso-beam ice models

| Ice element | Span (m) | Load (kN) | Radial ice thickness | | | | | | | | | | | | | | |
| | | | 10 mm | | | | | 25 mm | | | | | 38 mm | | | | |
			RIS	IWA	MT	MTS	MD	RIS	IWA	MT	MTS	MD	RIS	IWA	MT	MTS	MD
2-D plane stress iso-beam	100	30	0%	0%	12%	3%	1%	5%	0%	1%	3%	15%	50%	14%	4%	4%	37%
		45	0%	0%	0%	1%	12%	0%	0%	1%	4%	11%	3%	12%	3%	3%	5%
		60	0%	4%	7%	0%	6%	0%	0%	0%	1%	21%	10%	0%	2%	5%	16%
	200	30	0%	0%	12%	18%	14%	0%	0%	4%	1%	21%	12%	17%	4%	1%	29%
		45	0%	0%	0%	1%	10%	6%	0%	1%	11%	7%	15%	0%	0%	2%	10%
		60	0%	0%	0%	21%	6%	0%	0%	0%	4%	5%	6%	0%	1%	3%	3%
	300	30	1%	0%	0%	3%	2%	8%	16%	2%	0%	26%	0%	20%	2%	1%	20%
		45	0%	0%	0%	7%	5%	7%	0%	1%	1%	7%	10%	14%	1%	5%	6%
		60	0%	4%	0%	1%	4%	4%	0%	0%	6%	5%	0%	12%	2%	5%	5%

RIS – rate of ice shedding (%); IWA – initial amplitude of the transverse wave (m); MT – maximum cable tension at the excitation point (kN); MTS – maximum cable tension at the support (kN); MD – maximum mid-span displacement (m)

Table 7.4 Relative errors between simulation results of the ACSR conductor obtained by the 2-D plane stress iso-beam and the 3-D iso-beam ice models

7.3 Effect of numerical procedures and finite element formulations

7.3.1 Introduction

It is likely that the large differences in the peak values discussed in the previous section derive from numerical procedures and finite element formulations. Therefore, in order to investigate the effect of numerical procedures and element formulations, the ice-shedding scenarios of the 300 m span overhead ground wire are performed using the 2-D plane stress iso-beam and the 3-D iso-beam ice representations.

7.3.2 Newmark direct implicit integration method

In this study, the Newmark direct implicit integration method is selected to solve the incremental dynamic equilibrium equations, as discussed in Chapter 3. For the Newmark integration method to obtain optimum stability and accuracy in linear analysis, parameters α and δ can be determined. Newmark originally proposed the constant-average-acceleration method (also called trapezoidal rule), in which case δ and α are set to 0.5 and 0.25, respectively [6]. However, it is convenient to employ $\delta > 0.5$ in order to filter the high frequency mode response out of the solution. Furthermore, the solution of the nonlinear dynamic response of a finite element system using implicit time integration requires equilibrium iterations with convergence checks based on pre-defined tolerances [6]. Therefore, in this section, the effects of using different values of the numerical integration operator parameters (α, δ) and different iteration procedures on the calculated dynamic response are investigated. The convergence criterion is based on the energy,

ETOL, and displacements, DTOL, of the system with ETOL = 1.0^{-7} and DTOL = 1.0^{-5}, as

indicated in Chapter 3.

In order to carry out this analysis, the ice-shedding scenarios of the 300 m span

overhead ground wire with the pulse-load characteristics depicted in Figure 7.2 are

simulated. All line section parameters are kept the same as described in Chapter 6.
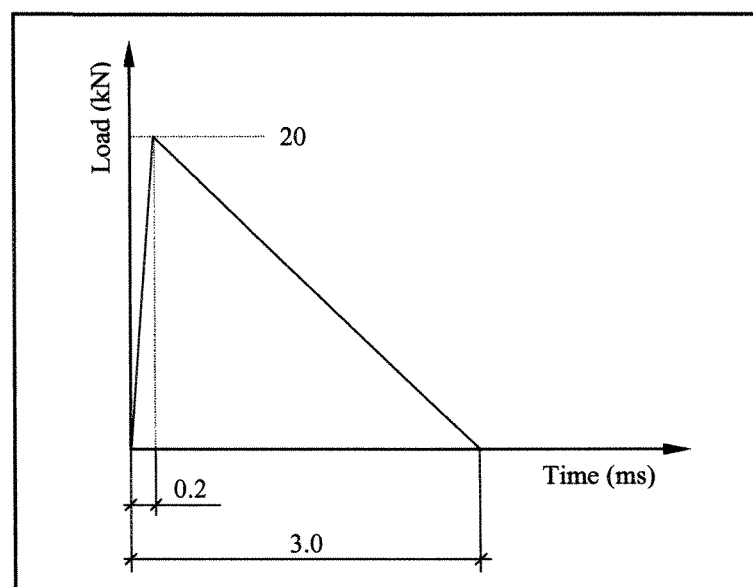
Figure 7.2 Pulse-load characteristics

A summary of the results of the numerical simulations is presented in Table 7.5 in terms of

the different numerical integration operator parameters (α, δ) and of different iteration

procedures. These results show that the Newmark direct implicit integration method with

parameters δ and α set to 0.5 and 0.25 (trapezoidal rule), respectively, and the full Newton

iteration method yield practically identical peak results for both ice models when full-span

ice shedding occurs. In addition, the effect of numerical damping is observed on the

numerical results when δ is set to 0.55. As a result of this numerical damping, the

maximum cable jump at the mid span (MD) and the rate of ice shedding (RIS) decrease.

Furthermore, the difference in the calculated cable mid-span displacement using the two

iso-beam ice models becomes important, while the cable tensions are in good agreement.

Nevertheless, the Newmark integration operator with parameters δ = 0.55 and α = 0.3

filters out the spurious high frequencies of the response due to finite element discretization

(cf. Figs. 7.3a and b). The high frequency oscillations that are still present correspond to

the fundamental longitudinal vibration of the iced cable (Fig. 7.3b)
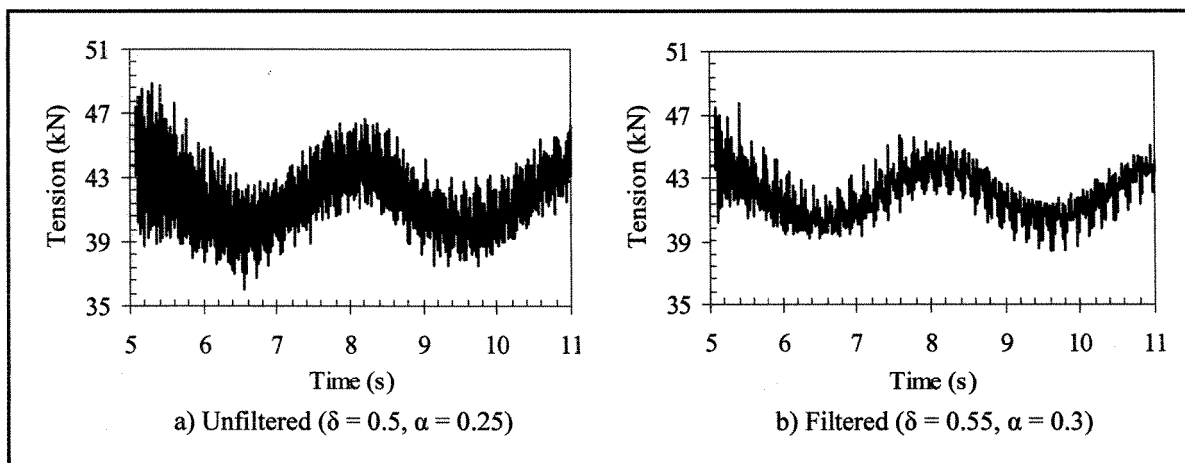
Figure 7.3 Filtered and unfiltered time histories of cable tensions at the left support

Integration parameters	Iteration method	3-D iso-beam				2-D plane stress iso-beam				Relative errors			
		RIS	IWA	MT	MD	RIS	IWA	MT	MD	RIS	IWA	MT	MD
$\delta = 0.5$ $\alpha = 0.25$	Modified Newton	100	0.071	77.8	1.23	100	0.071	77.4	1.04	0%	0%	1%	17%
	BFGS Matrix Update	100	0.069	76.9	1.28	100	0.068	77.3	1.10	0%	1%	5%	14%
	Full Newton	100	0.071	77.8	1.13	100	0.071	77.4	1.04	0%	0%	1%	8%
$\delta = 0.5$ $\alpha = 0.3$	Modified Newton	100	0.070	78.4	1.17	100	0.071	77.4	1.01	0%	1%	1%	13%
	BFGS Matrix Update	100	0.069	78.2	1.24	100	0.068	77.3	0.96	0%	1%	1%	22%
	Full Newton	100	0.069	78.4	1.18	100	0.068	77.4	1.01	0%	1%	1%	14%
$\delta = 0.5$ $\alpha = 0.35$	Modified Newton	100	0.071	78.7	1.15	98	0.071	77.2	0.96	2%	0%	2%	16%
	BFGS Matrix Update	99	0.070	76.3	1.10	99	0.068	77.1	0.93	0%	3%	1%	15%
	Full Newton	100	0.070	78.7	1.27	98	0.068	77.2	0.96	2%	3%	2%	24%
$\delta = 0.55$ $\alpha = 0.3$	Modified Newton	85	0.072	77.2	0.86	75	0.069	76.1	0.41	12%	4%	1%	52%
	BFGS Matrix Update	84	0.075	76.9	0.85	74	0.068	76.1	0.39	12%	9%	1%	54%
	Full Newton	84	0.074	77.2	0.85	75	0.068	76.1	0.39	11%	8%	1%	54%
$\delta = 0.55$ $\alpha = 0.35$	Modified Newton	83	0.078	77.4	0.87	75	0.071	76.3	0.50	10%	9%	1%	43%
	BFGS Matrix Update	85	0.067	77.6	0.91	74	0.068	76.3	0.45	13%	1%	2%	50%
	Full Newton	84	0.075	77.4	0.90	75	0.068	76.3	0.50	11%	9%	1%	44%

RIS – rate of ice shedding (%); IWA – initial amplitude of the transverse wave (m); MT – maximum cable tension (kN); MD – maximum mid-span displacement (m)

Table 7.5 Simulation results with various numerical parameters

7.3.3 Gauss integration orders

In the previous section, the Newmark direct implicit integration method with parameters δ and α set to 0.5 and 0.25, respectively, and the full Newton iteration method were found to yield practically identical peak results with the two iso-beam ice models when full-span ice shedding occurred. However, further analyses showed that the 2-D plane stress iso-beam ice model with these same integration and iteration parameters still resulted in smaller mid-span displacements than either the 3-D iso-beam or pipe-beam ice models when partial ice shedding took place. To investigate this discrepancy, several partial ice-shedding scenarios are analyzed on a 300 m long iced span section. A shock load with amplitude of 10 kN and characteristics depicted in Figure 7.2 is applied to the cable at 3 m from the span extremity in order to obtain partial ice shedding. It is found that when 2-D plane stress iso-beam elements are used, shear locking [6] of the elements occurs, which results in much smaller mid-span displacements than either the 3-D iso-beam or pipe-beam ice models.

Various procedures are proposed in the literature [6] to modify this displacement-based beam element formulation in order to arrive at efficient non-locking elements. A simple computational measure is to evaluate the stiffness matrices of these elements using reduced-order integration. In this case, it means integrating the displacement-based formulation with one-point Gauss integration along the axial direction for the two-node element. However, higher integration order may be required in the analysis of materially nonlinear response [6].

Therefore, analysis of the Gauss integration orders along the three axes (r, s and t) [6] is performed in the various models. This analysis showed that the default integration orders ($r = 1$, $s = 4$ and $t = 4$) for the 3-D iso-beam ice element yielded accurate results compared to those obtained with the pipe-beam ice representation with default values of integration order along the axial ($r = 1$), thickness ($b = 2$) and circumferential ($c = 8$) directions [2], respectively, while the 2-D plane-stress iso-beam element resulted in much smaller mid-span displacement as it was already indicated. It is noteworthy that shear locking also occurred using the 3-D iso-beam element when the integration order along the axial direction (r) was modified. Furthermore, changing the Gauss integration orders did not yield to unlocking of the 2-D plane stress iso-beam element (Table 7.6). It is therefore recommended to avoid this type of element to model the ice deposit on the cable if the objective of the analysis is to predict cable displacements accurately.

3-D iso-beam							2-D plane stress iso-beam						
Gauss int. orders			RIS	IWA	MT	MD	Gauss int. orders			RIS	IWA	MT	MD
r	s	t					r	s	t				
1	4	4	74	0.038	61.2	0.48	1	4	0	63	0.035	54.5	0.08
2	4	4	51	0.034	55.8	0.05	2	4	0	53	0.034	54.8	0.06
1	2	4	74	0.038	61.2	0.48	1	2	0	63	0.035	54.5	0.08

RIS – rate of ice shedding (%)
MT – maximum cable tension (kN)
IWA – initial amplitude of the transverse wave (m)
MD – maximum mid-span displacement (m)

Table 7.6 Simulation results with various Gauss integration orders

7.4 Conclusions

Numerical simulations have shown that it is feasible to model the accreted ice on the cable either by the 3-D iso-beam, the 2-D plane stress iso-beam or the pipe-beam elements in ADINA. The use of the 2-D plane stress iso-beam ice model reduces the computational effort considerably, which may be important when complex models are used. On the one hand, this ice model tends to result in much smaller mid-span displacements than either the 3-D iso-beam or pipe-beam ice models when partial ice shedding occurs due to the shear locking effect. On the other hand, the cable tensions calculated with the 2-D plane stress ice model are in good agreement with those obtained with either the 3-D iso-beam or pipe-beam ice models. The pipe-beam ice model yields results that are very consistent with those obtained with the 3-D iso-beam ice model.

As a result, careful analysis is required when partial ice shedding is predicted by the 2-D plane stress iso-beam ice model. Also, even if the Newmark method with parameters δ and α set to 0.5 and 0.25, respectively, yields practically identical results for the peak values when full-span ice shedding occurs, it is still recommended to set δ and α to 0.55 and 0.3, respectively, to filter out spurious high frequencies of the response due to finite element discretization.

CHAPTER 8

CONCLUSIONS AND RECOMMENDATIONS

8.1 Summary of original contributions

This research had four specific objectives and all of them have been met.

1) A numerical modeling technique capable of simulating progressive ice shedding on overhead cables subjected to shock loads was developed. This novel iced cable finite element modeling approach integrates the failure criteria of ice deposit into the model.

2) The numerical model was validated on a level single-span reduced-scale experimental model. The experiments were carried out at the CIGELE icing precipitation simulation laboratory.

3) The numerical model was successfully applied to simulations of level single-span real-scale overhead lines composed of four cable types: a classical stranded steel ground wire, an ACSR 54/7 conductor, an optical ground wire and an extra-high strength ground wire used for long-span lines.

4) Several ice-shedding scenarios were simulated with variables including ice thickness, line parameters such as span length, cable tension and axial rigidity, and pulse-load characteristics.

8.2 Conclusions on the numerical model

This study has shown that it is feasible to model the effects of ice shedding induced by a shock load on single-span overhead cables where the ice deposit is explicitly considered. The finite element model presented can serve as a basis to study various failure criteria of atmospheric glaze ice in terms of axial and bending stress-strain relations, and strain rate effects in particular. Various line section geometries can be easily investigated using the model.

The accreted ice on the cable can be represented either by the 3-D iso-beam, the 2-D plane stress iso-beam or the pipe-beam elements. However, application of the 2-D plane stress iso-beam element requires careful analysis when partial ice shedding is predicted by the model. It is also shown that the Newmark direct implicit integration method with parameters δ and α set to 0.55 and 0.3, respectively, adequately filters out the spurious high frequencies of the response due to finite element discretization.

Both the experimental and numerical analyses indicate that the most severe dynamic loads, i.e. the maximum cable tensions, occur right after the shock load is applied to the cable. However, numerical analyses of the effects of system flexibility of the reduced-scale conductor model showed that, as expected, the more flexible the structure is, the smaller the amplitude of the maximum cable tension.

8.3 Recommendations for numerical model improvements

8.3.1 Improvements in the failure criterion of glaze ice

In this study, the failure criterion defined for the glaze ice in terms of stress-strain relations and strain-rate effects, in particular, incorporates both the axial and bending strengths of ice. However, the reduced-scale experimental study has shown that the adhesive strength of glaze ice to the cable plays an important role in the de-icing mechanism. Therefore, it is recommended to improve the failure criterion of glaze ice by considering the axial, bending and adhesive strengths of ice as these values become available.

8.3.2 Modeling the structures and their foundations

In this study, to start with a simple model to demonstrate the new proposed approach, only a 2-D level single-span numerical model is proposed where the end points are fixed to rigid supports therefore neglecting the flexibility of the towers and their foundations. However, improvements of the numerical model to account for the effects of towers, foundations, interfaces and other line hardware components used to attach the cables to the towers can easily be implemented. Adding the influence of these components is expected to decrease the maximum load amplitudes at the supports and the magnitude of the displacements calculated.

8.4 Implications for the design of the DAC de-icing device

This study showed that the energy content of the shock load capable of removing the accreted ice from the cable is an important design issue. The proposed model may help to improve the design of the DAC de-icing device: it can serve to adjust the energy content of the shock load, i.e. the parameters of the de-icing device, capable of efficiently de-icing any overhead line section. Furthermore, since the model can calculate the dynamic effects of ice shedding induced by the shock load on the line components, the most adequate strategy for using the de-icing device for a particular line section can also be investigated with the model.

8.5 Recommendations for future study

8.5.1 Transmission line cascade

A transmission line cascade is the large-scale progressive collapse of the line in which many individual structures collapse one after the other like falling dominoes. Longitudinal cascades start with an initial failure in the structural elements that maintain tensions in the wires [58]. As reported by the Structures Group of the Scientific Commission appointed by the Government of Québec after the Ice Storm of 1998, many of the lines collapsed in longitudinal cascading caused by failed line components [51]. In addition, ice shedding from the conductors also contributes to the longitudinal loading of the line structures [32, 66 and 67].

The effects of the longitudinal dynamic loads on structures have been studied by taking into consideration, in most cases, a line component failure (e.g. cable rupture, failure of insulator string etc.) [5, 17, 35, 49 and 59]. Numerical studies of the longitudinal dynamic effects of ice shedding on overhead lines have also been carried out where sudden ice shedding was modeled [32, 66 and 67].

In this study, a numerical approach to model the dynamic effects of ice shedding where the rupture of the ice deposit is explicitly considered was introduced. Coupling this new modeling approach of ice shedding with the previous modeling approaches of the longitudinal dynamic loads on transmission lines subjected to icing loads may provide a powerful simulation tool for several practical industrial applications.

8.5.2 Full-scale experiments

Comparisons of the numerical and the reduced-scale experimental results indicate that the numerical model accurately calculates the dynamic response of iced cables subjected to shock loads. However, it was found that the reduced-scale model possesses a high degree of sensitivity to the flexibility of the cable used, which is believed to be unimportant in a real-scale line. Therefore, it is recommended to validate the numerical model on real-scale lines.

REFERENCES

[1]   A 931-96 (2002): Standard test method for tension testing of wire ropes and strand, 2004 Annual Book of ASTM Standards, Iron and Steel Products, 01.03: 489-493.

[2]   ADINA R&D Inc. ADINA Theory and Modeling Guide, September 2004, Watertown, MA, USA.

[3]   Alcan Cable, Canadian Product Catalogue. Bare overhead cable: Aluminum Conductor Steel Reinforced (ACSR), 2004. Available: http://www.cable.alcan.com.

[4]   Asch G. Les capteurs en instrumentation industrielle, 5e édition, Paris, France: Dunod, 1999.

[5]   Baenziger MT. Broken conductor loads on transmission line structures, Ph.D. Thesis, University of Wisconsin, Madison, 1981.

[6]   Bathe KJ. Finite element procedures, Upper Saddle River, NJ, USA: Prentice Hall, 1996.

[7]   Bernardin S. Étude et analyse du délestage de glace atmosphérique sur les câbles, M.Eng. Thesis, Université du Québec à Chicoutimi, Quebec, Canada, 1989.

[8]   CIGRE, 291, Guidelines for meteorological icing models, Statistical methods and topographical effects, Working Group B2.16, Task Force 03, April 2006.

[9]   Clough RW and Penzien J. Dynamics of Structures, New York: McGraw-Hill Inc., 1993.

[10] Costello GA. Theory of wire rope, New York: Springer-Verlag, 1990.

[11] Data Translation Inc. DT Measure Foundry, 2005, Marlboro, MA, USA.

[12] Druez J, Nguyen DD and Lavoie Y. Mechanical properties of atmospheric ice, Cold Regions Science and Technology 1986; 13: 67-74.

[13] Druez J, Louchez S and McComber P. Ice shedding from cables, Cold Regions Science and Technology 1995; 23: 377-388.

[14] E 799-03: Standard practice for determining data criteria and processing for liquid drop size analysis, 2004 Annual Book of ASTM Standards, General Methods and Instrumentation, 14.02: 268-272.

[15] E 1620-97: Standard terminology relating to liquid particles and atomization, 2004 Annual Book of ASTM Standards, General Methods and Instrumentation, 14.02: 551-557.

[16] Electric Power Research Institute. Transmission line reference book: Wind-induced conductor motion, EPRI Research Project 792, Palo Alto, CA, USA, 1979.

[17] Electric Power Research Institute. Longitudinal load and cascading failure risk assessment (CASE), Haslet, Texas, 1997.

[18] Elíasson ÁJ. Natural hazards and the Icelandic transmission grid, 7. Konferenca Slovenskih Elektroenergetikov CIGRE-CIRED, Velenja, Slovakia, June 2005; CIGRE ŠK B2-01.

[19] Eranti E and Lee GC. Cold Region Structural Engineering, New York: McGraw-Hill Inc., 1986.

[20] Eskandarian M. Ice shedding from overhead electrical lines by mechanical breaking: A ductile model for viscoplastic behavior of atmospheric ice, Ph.D. Thesis, Université du Québec à Chicoutimi, Quebec, Canada, 2005.

[21] Farzaneh M. Ice Accretion on H.V. conductors and insulators and related phenomena, Invited paper, Philosophical Transactions, The Royal Society, London, 2000; 358: 1-35.

[22] Francis D and Hengeveld H. Extreme weather and climate change, Canada: Minister of Supply and Services, 1998.

[23] Ghannoum E, Chouteau JP, Miron M, Yaacoub S and Yoshida K. Optical ground wire for Hydro-Québec's telecommunication network, IEEE/PES Winter Meeting, New York, NY, 29 January-2 February 1995.

[24] Godard S. Mesure de gouttelettes de nuage avec un film de collargol, Bulletin de l'Observatoire de Puy de Dome 1960, 41-46.

[25] Gow AJ and Ueda HT. Structure and temperature dependence of the flexural properties of laboratory freshwater ice sheets, Cold Regions Science and Technology 1989; 16: 249-269.

[26] Gurung CB, Yamaguchi H and Yukino T. Identification of large amplitude wind-induced vibration of ice-accreted transmission lines based on field observed data, Engineering Structures 2002; 24: 179-188.

[27] Havard DG and Van Dyke P. Effects of ice on the dynamics of overhead lines, Part II: Field data on conductor galloping, ice shedding, and bundle rolling, Proceedings of the 11th International Workshop on Atmospheric Icing of Structures, Montreal, Canada, 12-16 June 2005; 291-296.

[28] Hengeveld H, Whitewood B and Fergusson A. An introduction to climate change: A Canadian perspective, Canada: Minister of Public Works and Government Services, 2005.

[29] Hengeveld H. CO_2/Climate Report: 2003-2005 Science Review, Canada: Minister of Public Works and Government Services, 2006.

[30] Huschke RE. Glossary of meteorology, Boston, MA, USA: American Meteorological Society, 1959.

[31] Irvine HM. Cable structures, Cambridge, MA, USA: MIT Press, 1981.

[32] Jamaleddine A, McClure G, Rousselet J and Beauchemin R. Simulation of ice shedding on electrical transmission lines using ADINA, Computers and Structures 1993; 47 (4/5): 523-536.

[33] Kálmán T, Farzaneh M, McClure G, Kollár LE and Leblond A. Dynamic behavior of iced overhead cables subjected to mechanical shocks, Proceedings of the 6th International Symposium on Cable Dynamics, AIM, Charleston, SC, USA, 19-22 September 2005; 339-346.

[34] Kálmán T, Farzaneh M and McClure G. Numerical analysis of the dynamic effects of shock-load-induced ice shedding on overhead ground wires, Computers and Structures 2007; 85: 375-384.

[35] Kempner L. JR. Longitudinal impact loading on electrical transmission line towers: A scale model study, Ph.D. Thesis, Portland State University, 1997.

[36] Kollár LE and Farzaneh M. Modeling the dynamics of overhead cable with ice, Proceedings of the 11th International Workshop on Atmospheric Icing of Structures, Montreal, Canada, 12-16 June 2005; 309-314.

[37] Kollár LE, Farzaneh M and Karev AR. Modeling droplet size distribution near a nozzle outlet in an icing wind tunnel, Atomization and Sprays 2006; 16: 673-686.

[38] Laforte J-L, Phan CL, Nguyen DD and Félin B. Determining atmospheric parameters during ice accretion from the microstructure of natural ice samples, Proceedings of the 1st International Workshop on Atmospheric Icing of Structures, CRREL Special Report 83-17, Hanover, NH, USA, 1-3 June 1982; 175-184.

[39] Laforte J-L, Allaire M-A and Laflamme J. State-of-the-art on power line de-icing, Atmospheric Research 1998; 46: 143-158.

[40] Laforte J-L, Allaire M-A and Gagnon D. Ice shedding of 200 m-long artificially iced overhead cables at an outdoor test site, Proceedings of the 11th International Workshop on Atmospheric Icing of Structures, Montreal, Canada, 12-16 June 2005; 385-389.

[41] Landry M, Beauchemin R and Venne A. De-icing EHV overhead transmission lines by short-circuit currents, IEEE Canadian Review 2001 spring; 10-14.

[42] Lapointe M. Dynamic analysis of a power line subjected to longitudinal loads, M.Eng. Thesis, Department of Civil Engineering and Applied Mechanics, McGill University, Montreal, Canada, 2003.

[43] Leblond A, Montambault S, St-Louis M, Beauchemin R, Laforte J-L and Allaire M-A. Development of new ground wire de-icing methods, Proceedings of the 10th International Workshop on Atmospheric Icing of Structures, Brno, Czech Republic, 17-20 June 2002; 9-6.

[44] Leblond A, Lamarche B, Bouchard D, Panaroni B and Hamel M. Development of a portable de-icing device for overhead ground wires, Proceedings of the 11th International Workshop on Atmospheric Icing of Structures, Montreal, Canada, 12-16 June 2005; 399-404.

[45] Lecomte EL, Pang AW and Russell JW. Ice Storm '98, Canada: Institute for Catastrophic Loss Reduction, 1998.

[46] Loredo-Souza AM and Davenport AG. The effects of high winds on transmission lines, Journal of Wind Engineering and Industrial Aerodynamics 1998; 74-76: 987-994.

[47] Main IG. Vibrations and waves in physics, Cambridge, UK: Cambridge University Press, 1978.

[48] Matsuura M, Matsumoto H, Maeda Y and Oota Y. The study of ice shedding phenomena on transmission lines, Proceedings of the 1st International Symposium on Cable Dynamics, AIM, Liège, Belgium, 19-21 October 1995; 181-188.

[49] McClure G and Tinawi R. Mathematical modeling of the transient response of electric transmission lines due to conductor breakage, Computers and Structures 1987; 26 (1/2): 41-56.

[50] McClure G and Guevara EI. Seismic behaviour of tall guyed telecommunication towers, Spatial, Lattice and Tension Structures: Proceedings of the IASS-ASCE International Symposium, Atlanta, Georgia, USA, 24-28 April 1994; 259-268.

[51] McClure G, Johns KC, Knoll F and Pichette G. Lessons from the ice storm of 1998 improving the structural features of Hydro-Québec's power grid, Proceedings of the 10th International Workshop on Atmospheric Icing of Structures, Brno, Czech Republic, 17-20 June 2002; 9-3.

[52] McClure G and Lapointe M. Modeling the structural dynamic response of overhead transmission lines, Computers and Structures 2003; 81: 825-834.

[53] McClure G. Structural Dynamics, Class notes, Department of Civil Engineering and Applied Mechanics, McGill University, Montreal, Canada, 2004.

[54] Meirovitch L. Analytical methods in vibrations, New York: Macmillan, 1967.

[55] Momomura Y, Harukawa H, Okamura T, Hongo E and Ohkuma T. Full-scale measurements of wind-induced vibration of a transmission line system in a mountainous area, Journal of Wind Engineering and Industrial Aerodynamics 1997; 72: 241-252.

[56] Morgan VT and Swift DA. Jump height of overhead line conductors after the sudden release of ice loads, Proceedings of IEE 1964; 111 (10): 1736-1746.

[57] PCB Group, Inc. FTQ-200F-0105: PCB Piezotronics Force/Torque Sensor Catalog, USA, 2005.

[58] Peabody AB and McClure G. Linking line security with atmospheric icing levels, Proceedings of the 10th International Workshop on Atmospheric Icing of Structures, Brno, Czech Republic, 17-20 June 2002; 7-2.

[59] Peabody AB. Applying shock damping to the problem of transmission line cascades, Ph.D. Thesis, Department of Civil Engineering and Applied Mechanics, McGill University, Montreal, Canada, 2004.

[60] Péter Zs. Modeling and simulation of the ice melting process on a current-carrying conductor, Ph.D. Thesis, Université du Québec à Chicoutimi, Quebec, Canada, 2006.

[61] Petrovic JJ. Review: Mechanical properties of ice and snow, Journal of Materials Science 2003; 38: 1-6.

[62] Phillips-Fitel, Online Product Catalogue. Optical Ground Wire (OPGW), 2006. Available: http://www.phillipsfitel.com.

[63] Poots G. Ice and snow accretion on structures, Taunton, Somerset, England: Research Studies Press, 1996.

[64] Prud'Homme P, Dutil A, Laurin S, Lebeau S, Benny J and Cloutier R. Hydro-Québec TransÉnergie line conductor de-icing techniques, Proceedings of the 11th International Workshop on Atmospheric Icing of Structures, Montreal, Canada, 12-16 June 2005; 373-378.

[65] Roberge M. A study of wet snow shedding from an overhead cable, M.Eng. Thesis, Department of Civil Engineering and Applied Mechanics, McGill University, Montreal, Canada, 2006.

[66] Roshan Fekr M and McClure G. Numerical modeling of the dynamic response of ice shedding on electrical transmission lines, Atmospheric Research 1998; 46: 1-11.

[67] Roshan Fekr M. Dynamic response of overhead transmission lines to ice shedding, M.Eng. Thesis, Department of Civil Engineering and Applied Mechanics, McGill University, Montreal, Canada, 1995.

[68] Sakamoto Y. Snow accretion on overhead wires, Philosophical Transactions, The Royal Society, London, 2000; 358: 2941-2970.

[69] Scalzi JB and Podolny W. Construction and design of cable-stayed bridges, Toronto: John Wiley & Sons Inc., 1976.

[70] Schulson EM. Brittle failure of ice, Engineering Fracture Mechanics 2001; 68: 1839-1887.

[71] Sirignano WA. Fluid dynamics and transport of droplets and sprays, Cambridge, UK: Cambridge University Press, 1999.

[72] Timco GW and Frederking RMW. Comparative strength of fresh water ice, Cold Regions Science and Technology 1982; 6: 21-27.

[73] Toussaint J-M. Le galop des lignes électriques : Mesures en soufflerie et simulations, M.Eng. Thesis, Université de Liège, Belgium, 1998.

[74] Volat C, Farzaneh M and Leblond A. De-icing/anti-icing techniques for power lines: current methods and future direction, Proceedings of the 11th International Workshop on Atmospheric Icing of Structures, Montreal, Canada, 12-16 June 2005; 323-333.

[75] Yu A-T. Vibration damping of stranded cable, Experimental Stress Analysis 1952; 9: 141-158.

APPENDIX A

THEORETICAL BACKGROUND

A.1 Equation of the catenary

The shape of a suspended cable under its self-weight takes the form of a catenary. Let us consider a uniform and axially rigid (inextensible) cable hanging under its self-weight between two fixed points (*A*, *B*) at the same level where the cable is assumed to be perfectly flexible in bending and torsion (Fig. A.1). The governing differential equation of the catenary derived from the static equilibrium of the isolated cable element located at (*x*, *z*) is defined in (A.1) where *H* is the horizontal component of the cable tension and *mg* is the self-weight of the cable per unit length [31].

$$H\frac{d^2z}{dx^2} = -mg\sqrt{1+\left(\frac{dz}{dx}\right)^2} \tag{A.1}$$

The profile of the axially rigid catenary under its self-weight is obtained by solving (A.1) and is, thus, given in (A.2) where *l* is the length of the span.

$$z = \frac{H}{mg}\left\{\cosh\left(\frac{mgl}{2H}\right) - \cosh\frac{mg}{H}\left(\frac{l}{2}-x\right)\right\} \tag{A.2}$$
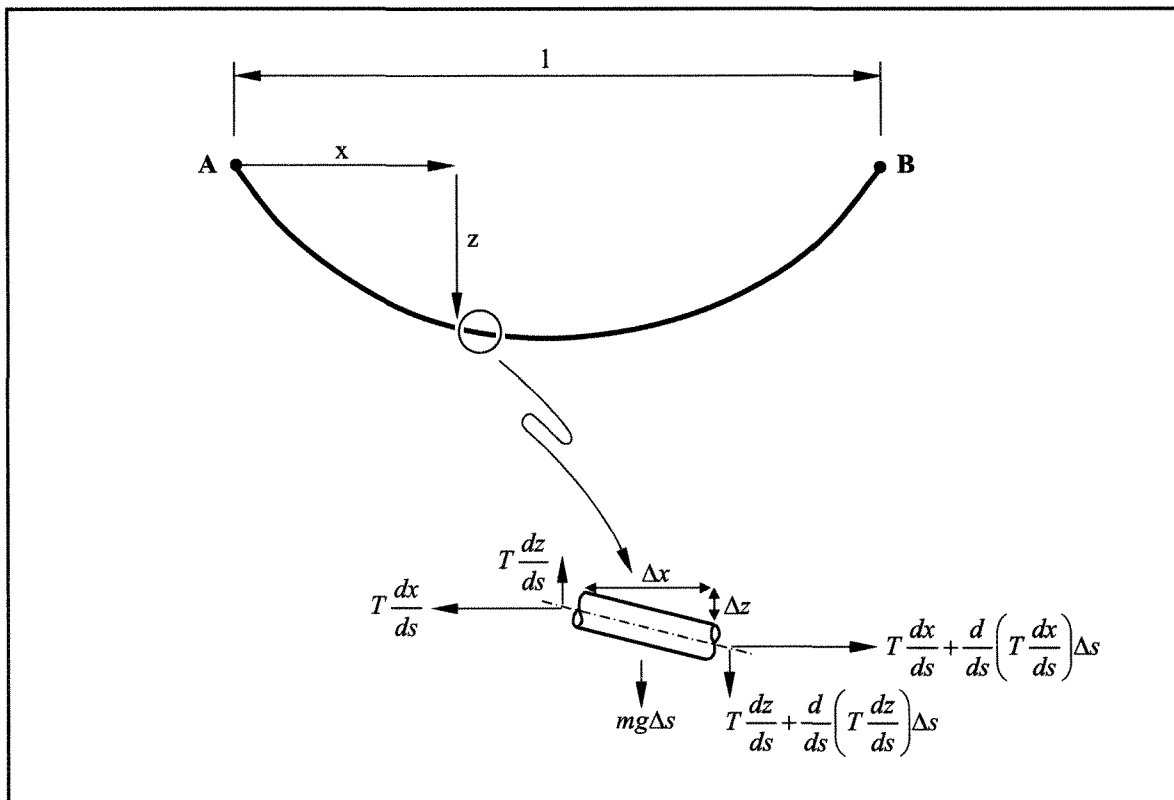
Figure A.1 Equilibrium of a cable element (adapted from [31])

The horizontal component of the cable tension (H) is found by solving (A.3) where L is the unstressed length of the cable.

$$\sinh\left(\frac{mgl}{2H}\right) = \frac{mgL}{2H} \tag{A.3}$$

However, the solution method of (A.3) tends to be cumbersome. Simplifications can be made when the sag-to-span ratio is less than 15% [31, 69], which often corresponds to the situation where cables with relatively low sag are used for overhead transmission lines. The horizontal component of the cable tension can then be approximated with a reasonably

small percentage of error by using the parabolic equation given in (A.4) where d is the sag

at the mid span [31, 69].

$$H = \frac{mgl^2}{8d} \qquad\qquad (A.4)$$

A.2 Transverse and longitudinal waves in transmission line cables

A.2.1 Introduction

Both the numerical and the experimental [44] analyses of a real-scale line indicate that

the shock load applied to the cable generates both transverse and longitudinal waves in the

cable that propagate along the span. The longitudinal (axial) waves travel much faster than

the transverse waves do and they may also reach the span extremities with enough energy

to be reflected back in the span. Axial waves may propagate back and forth with slowly

decreasing amplitude until all the power conveyed by the wave has been absorbed.

Nevertheless, to our best knowledge, the longitudinal wave does not seem to significantly

contribute to the de-icing while the transverse wave has an important role [44]. Overhead

transmission line cables are assumed to possess negligible bending stiffness and

consequently the forces restoring their global equilibrium profile derive entirely from the

axial tension and therefore they can be considered as taut strings.

A.2.2 Transverse waves

Equation (A.5) describes the speed of a transverse wave (c_T) traveling in a taut string

where T is the tension and m is the mass per unit length of the string [47].

$$c_T = \sqrt{\frac{T}{m}} \tag{A.5}$$

The characteristic impedance of the string (Z_T) to the transverse wave is given in (A.6) [47].

$$Z_T = \sqrt{T \cdot m} \tag{A.6}$$

When the end of the string is attached to a support whose impedance (Z_S) is not equal to the characteristic impedance of the string, i.e. the string is incorrectly terminated, reflection of the traveling wave with reverse amplitude occurs, which is expressed by the reflection coefficient (R) as given in (A.7) [47].

$$R = \frac{Z_T - Z_S}{Z_T + Z_S} \tag{A.7}$$

If the end of the string is rigidly fixed, the reflected waves have equal amplitudes. However, if the string is terminated with an impedance equal to its own characteristic impedance, i.e. the string is correctly terminated ($Z_S = Z_T$), there should be no reflected wave ($R = 0$). The characteristic impedance of the string has the same units as viscous damping, kg/s.

The energy distribution pattern along the string follows the wave propagation and the instantaneous power conveyed by the wave is expressed by (A.8) where v is the transverse velocity of the cable [47].

$$P = \frac{T}{c_T} v^2 \tag{A.8}$$

Real waves that propagate in solids are affected by damping that leads to the attenuation of the traveling wave that loses its energy as it propagates through the medium.

The natural frequencies (ω_n) of a uniform taut string with a constant mass per unit length (m) subjected to a constant tension (T) and fixed at both ends are given by (A.9) in rad/s where L is the length of the string, n is the wave number or harmonic and c is the wave velocity [54]. The frequency ω_1 is called the fundamental frequency.

$$\omega_n = 2n\pi \frac{c}{2L} \qquad (n = 1, 2, 3, ...) \qquad (A.9)$$

Substitution of (A.5) into (A.9) yields to the natural frequencies of the transverse wave given in (A.10) [54].

$$\omega_{Tn} = n\pi\sqrt{\frac{T}{mL^2}} \qquad (n = 1, 2, 3, ...) \qquad (A.10)$$

A.2.2 Longitudinal waves

Equation (A.11) describes the speed of the longitudinal (axial) traveling waves on a string made from a linear elastic material in which both the density (ρ) and Young's modulus (E) are known [47].

$$c_L = \sqrt{\frac{E}{\rho}} \qquad (A.11)$$

The velocity of longitudinal waves on transmission line cables is typically several km/s, which is much higher than most transverse wave speeds.

The characteristic impedance of the string (Z_L) to the longitudinal wave is given in (A.12) where A is the cross-sectional area of the string [47].

$$Z_L = A\sqrt{\frac{E}{\rho}} \tag{A.12}$$

Substitution of (A.11) into (A.9) yields the natural frequencies of the longitudinal wave (ω_L) given in (A.13) in rad/s [54].

$$\omega_{Ln} = n\pi\sqrt{\frac{EA}{mL^2}} \qquad (n = 1, 2, 3, ...) \tag{A.13}$$

A.3 Natural frequencies and mode shapes of suspended cables

A.3.1 Introduction

Natural frequencies and mode shapes of suspended cables can be categorized as out-of-plane, in-plane asymmetric and in-plane symmetric modes. The in-plane modes occur in the plane where the sag of the cable is defined while the out-of-plane or swinging modes are perpendicular to this plane. Asymmetric in-plane modes consist of asymmetric vertical components and symmetric longitudinal components, while symmetric in-plane modes consist of symmetric vertical components and asymmetric longitudinal components. It is noteworthy that the in-plane asymmetric modes induce no overall additional tension in the cable while the symmetric in-plane modes do. In this section, analytical expressions adapted from [31] are presented to calculate the natural frequencies of level flat-sag suspended cables using the parabolic approximation to define the suspended cable profile.

A.3.2 Asymmetric in-plane modes

Equation (A.14) describes the natural frequencies (ω_n) of the in-plane asymmetric modes where H is the horizontal component of the cable tension, m is the mass per unit length of the cable and l is the span length.

$$\omega_n = 2n\pi\sqrt{\frac{H}{m \cdot l^2}} \qquad (n = 1, 2, 3, \ldots) \tag{A.14}$$

A.3.3 Symmetric in-plane modes

The natural frequencies of the symmetric in-plane modes are calculated using the non-zero roots in υ of the transcendental equation given in (A.15) where λ^2, defined in (A.16), is a parameter that quantifies the relative importance of geometric slack effects (numerator) and elastic cable extension (denominator).

$$\tan\frac{\upsilon}{2} = \frac{\upsilon}{2} - \frac{4}{\lambda^2}\left(\frac{\upsilon}{2}\right)^3 \tag{A.15}$$

$$\lambda^2 = \frac{l \cdot (mgl/H)^2}{HL_e/EA} \tag{A.16}$$

L_e is called the effective cable length and is expressed as given in (A.17) where d is the sag.

$$L_e = l\left(1 + 8\left(\frac{d}{l}\right)^2\right) \tag{A.17}$$

The in-plane symmetric natural frequencies (ω_n) are given by (A.18).

$$\omega_n = \frac{\upsilon}{l}\sqrt{\frac{H}{m}}$$

(A.18)

A.3.4 Out-of-plane modes

The natural frequencies (ω_n) of the out-of-plane modes are given in (A.19).

$$\omega_n = n\pi\sqrt{\frac{H}{m \cdot l^2}} \qquad (n = 1, 2, 3, ...)$$

(A.19)

APPENDIX B

EXPERIMENTAL TEST PARAMETERS

B.1 Parameters involved in icing

Atmospheric icing may take place at ambient air temperatures between -10 and 0°C, or sometimes, at lower temperatures under particular conditions. The occurrence, severity, and type of atmospheric icing depend largely on temperature, wind speed, total water content of the air, and water droplet dimensions. The types of atmospheric ice accretions that are significant for our purpose are heavy adherent wet snow, hard rime, large deposits of lightweight rime ice and dense glaze ice [20]. The latter is the focus of this study. Therefore, the objective is to produce an artificial glaze deposit on the stainless steel cable span installed in the CIGELE icing precipitation simulation laboratory.

Glaze ice forms when the supercooled water droplet freezing time is long enough for a film of water to cover the accreting surface and the temperature of the ice surface is 0°C. Glaze is usually associated with large values of the liquid water content of the air and droplet sizes as found in freezing rain incidents [63].

One of the major factors that influences atmospheric icing phenomena and characterizes the spray in the icing precipitation laboratory is the droplet size in the aerosol cloud, which is usually described by the median volume diameter (MVD) or another

representative diameter, and the droplet size distribution (DSD) provided by the air atomizing nozzles. The droplet size distribution is dependent on the nozzle type and varies significantly from one type to another. Factors such as liquid properties, nozzle capacity, spraying pressure and spray angle can also affect the droplet size [71]. Flow rate has a direct relation to droplet size, i.e. an increase in flow rate increases the droplet size and vice versa, while pressure and spray angle have an inverse relationship effect on droplet size, i.e. an increase in pressure and spray angle reduces the droplet size and vice versa. Liquid properties such as viscosity and surface tension increase the amount of energy required to atomize the spray. An increase in any of these properties typically increases the droplet size.

In our laboratory conditions, uniform glaze accretion with a density of 850-900 kg/m^3 was found to occur on the stainless steel cable installed with the experimental parameters shown in Table B.1. However, it should be noted that the study of the freezing mechanism of the supercooled droplets is beyond the scope of this study.

Parameters of the spraying system:	
Nozzle air pressure	1.0 bar (15 psi)
Nozzle water pressure	4.8 bar (70 psi)
Nozzle water flow rate per nozzle	0.28 l/min
Nozzle water temperature	1°C
Other controlled parameters:	
Refrigerated room temperature	-10°C
Wind speed	3.5 m/s (± 0.2 m/s)
Speed of the gear motor	17 rpm

Table B.1 Experimental parameters

The droplet size distribution (DSD) is observed by using the collargol slide impact method [24] and the median volume diameter (MVD) is calculated from the DSD data. For sampling the DSD, a special tool called "cylindrical droplet impact sampler" is used [37]. This tool consists of a horizontal cylinder covered with an aluminum pipe which slides under the impetus of a spring. A small slide, 38 x 19 mm, is placed inside the horizontal cylinder. The aluminum pipe has a rectangular opening for exposing the slide to impinging spray droplets. Exposure time is regulated by adjusting the force of the spring. The DSD data observation can be considered as spatial according to [14]. The representative diameter of droplets (1000 traces) is measured using a Scienscope™ microscope (model: SZZ PK1).

The MVD measured at the position of the stainless steel cable is 158 μm at nozzle water and air pressure of 4.8 and 1 bar, respectively and at a wind speed of 3.5 m/s. Droplet diameters ranged from 5 μm to 285 μm. Figures B.1a and b show the size distribution and the cumulative distribution functions obtained at the specific air and water pressure based on the measurement of 1000 traces.
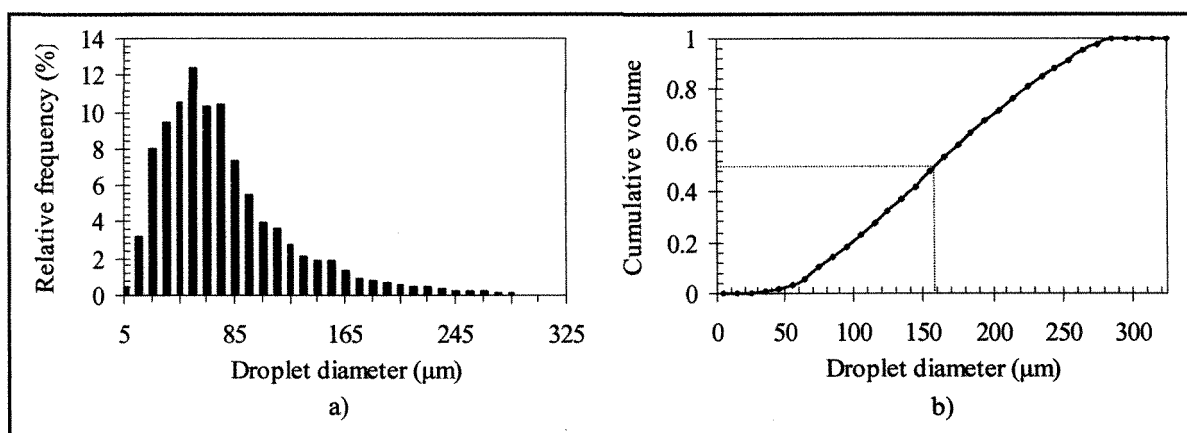
Figure B.1 (a) Size frequency distribution and (b) cumulative distribution functions

Another factor that influences atmospheric icing phenomena is the liquid water content of the air (LWC) that can also be expressed by the precipitation rate [63]. Changes in the LWC may also influence the DSD and vice versa, therefore they must be examined simultaneously [37]. The precipitation rate is measured using a pluviometer constructed in the laboratory. It is equipped with a horizontal and vertical collecting opening, each having a surface area of 101.34 cm^2. The pluviometer is placed into the air/water spray flow where the stainless steel cable is installed and kept in place during 5 min. The horizontal and vertical precipitation rates measured are 44.4 and 55.0 mm/h, respectively. The precipitation rate perpendicular to the exposed surface and the angle of impact are calculated from the horizontal and vertical values, and they are 70.7 mm/h and 39°, respectively.

Wind speed is measured using an anemometer manufactured by Omega (model: HHF710). It has an air flow measuring range of 0.2 to 40 m/s and a resolution of 0.01 m/s.

B.2 Parameters of the shock load generator

The speed of the shock load generator – a piston rod – is measured using a high speed digital camera at different air pressures. Figure B.2 shows the relationship between the inlet air pressure and the piston speed obtained. An air pressure not greater than 6 bars is used throughout the experimental study for practical safety reasons regarding the pneumatic cylinder and the ICP® force sensor installed at the top of the piston rod.
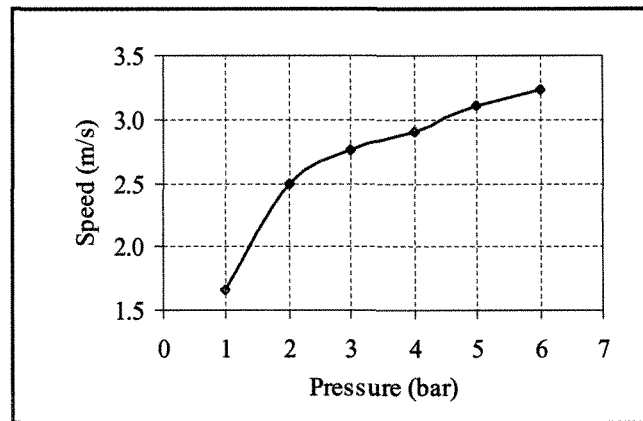
Figure B.2 Speed of the shock load generator (piston rod)

B.3 Damping of the level single-span reduced-scale conductor model

Damping of the level single-span reduced-scale conductor model consists of the internal damping of the cable and more importantly the damping caused by frictional forces in the ball bearings of the sleeves installed at both ends of the span (Fig. 4.5). The damping in the ball bearings is considered to be small, and of frictional type. The damping ratio (ζ) is determined in free vibration from the time history of cable mid-span displacement using the logarithmic decrement [9, 53]:

$$R_n = \ln\left(\frac{u(t)}{u(t + nT_D)}\right) \tag{B.1}$$

where $u(t)$ and $u(t + nT_D)$ are the amplitudes of the damped system in free vibration at two instances, n is an integer and T_D is the natural period of the fundamental free vibration mode. One way to characterize the amount of damping is to find the number of cycles to ½

amplitude, i.e. the number of cycles necessary to decrease the amplitude $u(t)$ by 50% ($n_{1/2}$).

Hence, the damping ratio is defined as [53]

$$\xi = \frac{0.11}{n_{1/2}}$$ (B.2)

Time history plots of the cable mid-span vertical displacement in free vibration are obtained by suddenly releasing the cable from a certain height at the mid span while its vertical displacement at the mid span is being recorded. This procedure was repeated several times in order to ensure the repeatability of results. Figure B.3 shows an example of time history results obtained. These results indicate that the natural period of the free vibration, T_D, is 0.3 s and the number of cycles necessary to decrease the amplitude by 50%, $n_{1/2}$, is 2-4 (u_3-u_1; u_6-u_2; u_8-u_4). Thus, the damping ratio of the system is about 3-5%.
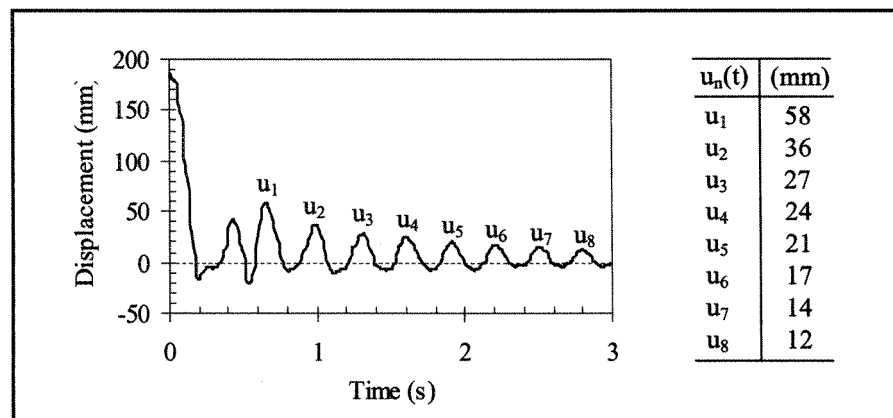
Figure B.3 Time history of cable vertical mid-span
displacement in free vibration

B.4 Characteristic material properties of the wire rope

B.4.1 Introduction

Numerical results of the reduced-scale experimental model reveal that the linear Hookean material law (Fig. 5.1) is inadequate to calculate the maximum cable tension at the support. Therefore, to get a more realistic material model, standard tensile tests in accordance with ASTM A 931-96 (2002) [1] are performed on the RR-W-410D stainless steel wire rope (Appendix C) used for the experimental study, using a 250 kN MTS 810 Material Testing System installed in the CIGELE material testing laboratory. The objective of testing the wire rope is to determine its characterizing material law and to provide a stress-strain curve that serves as input in the numerical model.

A wire rope is composed of many individual wires which are formed and fabricated to move or operate at close tolerances to one another. The various components of a wire rope are shown in Figure B.4, where the rope is constructed by laying several strands around a core. The core may be either fiber, or an Independent Wire Rope Core (IWRC), which is actually a smaller wire rope within the strands of the outer wire rope. The strands are constructed by helically wrapped wires around a center wire. The wires are predominantly constructed from high-carbon steel, but they may also be formed from various metals such as iron, stainless steel, monel or bronze. The major portion of the load acting on a rope is carried by the strands while the core provides proper support for the strands under bending and axial loading conditions. When a wire rope bends, each of its many wires slides and adjusts to accommodate the differences in length between the inside and outside of the bend. The sharper the bend is, the greater the movement. Wire ropes are identified by

classifications based upon the number of strands and the nominal number of wires in each strand (e.g. 7x19) [10].
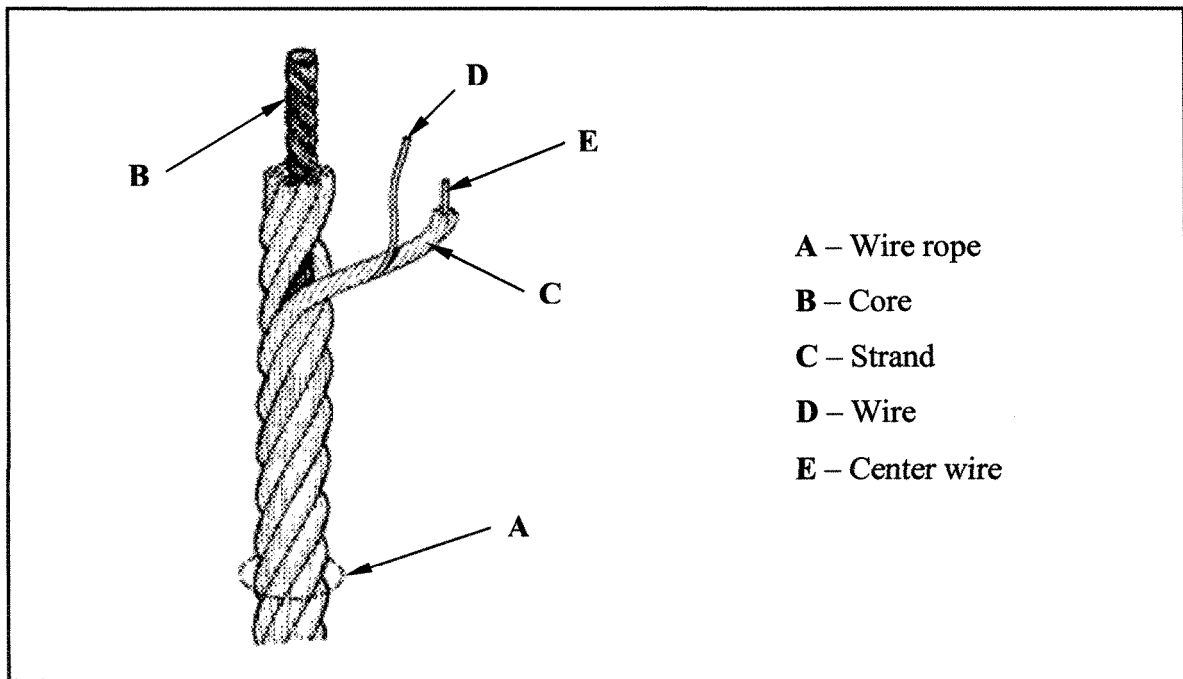
Figure B.4 Wire rope (adapted from [10])

The 810 Material Testing System used in this work is manufactured by MTS Systems Corporation and comprises a load unit assembly (model: 318.25) force rated to 250 kN, a hydraulic power unit (model: 505.07) and a digital controller (model: Flex Test SE) that employs the MTS Model 793 testing software. The load unit assembly is equipped with two snubbing type wire tension grips manufactured by Material Testing Technology (model: ASTM.A0370.61) in accordance with ASTM A370. One of the grips is installed to the crosshead of the load unit while the other one is mounted to a force transducer rated at

25 kN (model: 661.20E-01). Wire extension is measured by the integrated displacement transducer that serves as position measurement and control.

B.4.2 Description of a tensile test

Seven specimens of the RR-W-410D stainless steel wire rope of 4.1 mm in diameter and of 3.1 m in length are tested in accordance with ASTM A 931-96 (2002) [1]. The specimen length of 3.1 m is found to provide proper gripping. This length allows the specimen to turn around the snubbing wheels three times providing a gauge length of 1 m. The rope diameter is measured with a caliper by following the ASTM standard instructions as shown in Figure B.5. The cross-sectional area of the wire rope (13.2 mm^2) is defined by its diameter and considered a constant during the test as if it was a material of uniform cross section. The rate of loading is 20 mm/min. Each sample is pre-stretched before starting the measurement in order to provide proper gripping. A pre-stretching force of 200 N is found to be adequate. However, one case with practically no pre-stretching force is also studied in order to show the high flexibility of the wire rope under the prevailing loads of the experimental study of the reduced-scale model. Nevertheless, it should be noted that this measurement serves only as a demonstration since its accuracy for low values of loading is uncertain, due to possibilities of improper gripping.
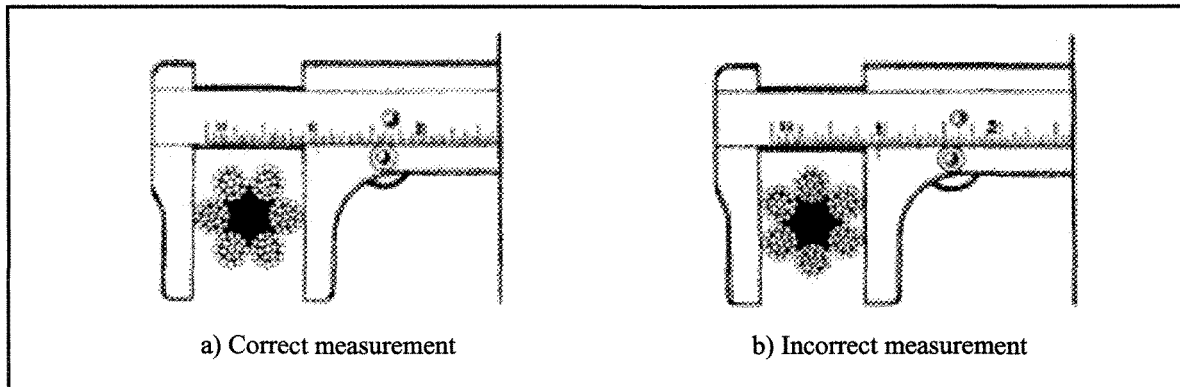
Figure B.5 Measurement of wire rope diameter (adapted from [1])

Additional tests are also run on a strand of the RR-W-410D stainless steel wire rope of 4.1 mm in diameter in order to determine the modulus of elasticity of the wire material. The actual diameter of the strand made of 19 wires is measured with a micrometer caliper and is 1.04 mm. Test instructions described above are followed for this test series too. The gauge length is set to 1 m (±5%) and the rate of loading is 5 mm/min.

B.4.3 Results and discussions

Results of the tensile tests reveal that the breaking strength of the wire rope, i.e. the ultimate load at which a tensile failure occurs, is 14 kN (±2%). However, individual wire failure starts to occur at 10.7 kN (±2%), which is defined by the manufacturer as the nominal strength of the cable. A typical stress-strain curve of a stainless steel wire rope tested shown in Figure B.6 indicates that the modulus of elasticity of the cable, i.e. the slope of the elastic portion of the stress-strain curve is 80 GPa (±2%). Furthermore, it is also seen that the cable material law shows high degrees of nonlinearity in the region of the

prevailing loads of the reduced-scale experimental model, especially when practically no pre-stretching force is applied (Fig. B.6b).

a) With pre-stretching force (200 N)

b) Without pre-stretching force
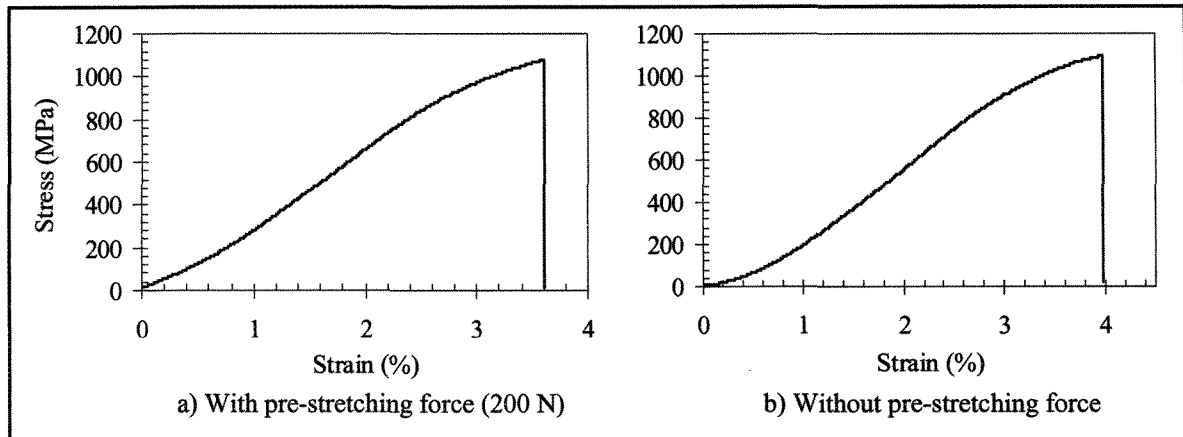
Figure B.6 Stress-strain curve of the wire rope

Results of the tensile tests performed on a single strand reveal that the breaking strength of a strand is 2.25 kN ($\pm 2\%$). A typical stress-strain curve of such a strand shown in Figure B.7 indicates that the modulus of elasticity of the wire material is 200 GPa ($\pm 2\%$).
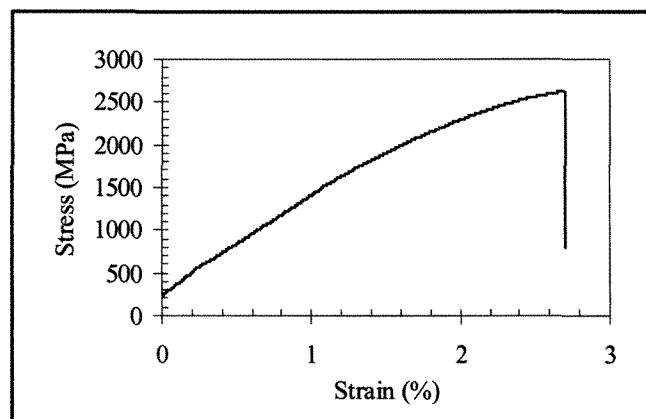
Figure B.7 Stress-strain curve of a strand

APPENDIX C

CABLE PARAMETERS

C.1 Conductor

Conductor parameters (source: Alcan Cable [3])		
Name		CONDOR
Type		ACSR 54/7
Number of aluminum strands		54
Diameter of aluminum strands	mm	3.08
Cross-sectional area of aluminum strands	mm^2	402.84
Number of steel strands		7
Diameter of steel strands	mm	3.08
Overall diameter	mm	27.762
Total cross-sectional area	mm^2	455.03
Modulus of elasticity	GPa	68.95
Mass per unit length	kg/m	1.5239
Rated tensile strength	kN	125.44

Table C.1 Condor ACSR (Aluminum Conductor Steel Reinforced) conductor

C.2 Ground wire

Ground wire parameters (source: Hydro-Québec)		
Name		½ inch galvanized
Type		steel strand
Number of steel strands		7
Diameter of steel strands	mm	4.191
Overall diameter	mm	12.7
Total cross-sectional area	mm^2	96.5
Modulus of elasticity	GPa	172.4
Mass per unit length	kg/m	0.759
Rated tensile strength	kN	113.6

Table C.2 Galvanized steel strand

C.3 Optical ground wire (OPGW)

Optical ground wire parameters (source: Phillips-Fitel [62])		
Name		Phillips-Fitel
Type		PFISTAR™
Number of aluminum-clad steel (ACS) wires		8
Diameter of ACS wires	mm	4.1
Cross-sectional area of ACS wires	mm^2	105
Number of aluminum alloy wires		14
Diameter of aluminum alloy wires	mm	4.1
Aluminum tube diameter	mm	6.5
Number of spacer grooves		5
Total fiber capacity		40
Overall diameter	mm	22.9
Total cross-sectional area	mm^2	290
Modulus of elasticity	GPa	101.5
Mass per unit length	kg/m	1.284
Rated tensile strength	kN	174

Table C.3 Optical ground wire

C.4 Extra-high strength ground wire
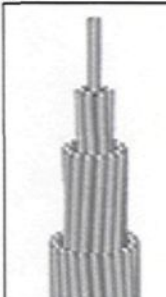
High strength ground wire parameters (source: Hydro-Québec)		
Name		galvanized steel strand
Code		CDG29DP
Number of steel strands		37
Diameter of steel strands	mm	4.1
Overall diameter	mm	28.6
Total cross-sectional area	mm^2	490.3
Modulus of elasticity	GPa	150
Mass per unit length	kg/m	3.959
Rated tensile strength	kN	693.7

Table C.4 Extra-high strength ground wire

C.5 Stainless steel cable

Stainless steel cable parameters		
Name		Stainless steel wire rope
Type		RR-W-410D 301/302
Cable No. 1		
Overall diameter	mm	4.1
Total cross-sectional area	mm^2	13.2
Mass per unit length	g/m	70
Number of strands		7
Diameter of strands	mm	1.04
Number of wires in a strand		19
Rated tensile strength	kN	10.7
Cable No. 2		
Overall diameter	mm	3.2
Total cross-sectional area	mm^2	8
Mass per unit length	g/m	43
Number of strands		7
Diameter of strands	mm	0.67
Number of wires in a strand		19
Rated tensile strength	kN	7.8

Table C.5 Stainless steel cable

APPENDIX D

FORTRAN CODES

D.1 Static cable profile

D.1.1 Introduction

In this section, program codes written in FORTRAN to calculate the static profile of a level single-span axially rigid catenary under its self-weight are introduced. The program applies the analytical expressions for the catenary profile of suspended cables adapted from [31] and presented in Appendix A. It reads the input parameters from pre-defined text files (input files) and also writes the calculated results into text files (output files) that can be used as inputs to ADINA in order to facilitate the definition of the numerical model. Parameters of the line section such as the span length, the sag-to-span ratio or the initial horizontal cable tension and the cable parameters are defined in the input files. The program also provides options for the selection of the coordinate system in which the cable is defined. It calculates the coordinates of the cable profile and the initial tensile strain of the cable elements, in particular.

D.1.2 Input files

- DATA_GEOM

Number of element	(DIV)	[-]
Span length	(L)	[m]
Sag-to-span ratio	(SR)	[%]
Acceleration of gravity	(G)	[m/s^2]
In-plane coordinate system	(1) x-z; (2) x-y; (3) y-z	

- DATA_CABLE

Cross-sectional area of aluminum strands	(A1)	[mm^2]
Total conductor cross-sectional area	(A)	[mm^2]
Overall diameter	(D)	[mm]
Stranding-number of aluminum	(N1)	[-]
Diameter of aluminum strands	(D1)	[mm]
Stranding-number of steel	(N2)	[-]
Diameter of steel strands	(D2)	[mm]
Mass of the cable per unit length	(M)	[kg/m]
Rated tensile strength	(TS1)	[kN] ... if calculated from the 'k' factor (available for ACSR conductors) set to zero
EI$_{min}$	(EIM)	[Nm^2]
'k' factor	(K)	[-] ... only for ACSR conductor
Initial horizontal tension	(H1)	[kN] ... if unknown set to zero

- YOUNGS_MODULUS

Aluminum stranded (all types)	(EA)	[GPa]
Steel core strand for ACSR and ACSR/SD	(ES)	[GPa]
Alumoweld-solid	(EAW_SO)	[GPa]
Alumoweld-stranded	(EAW_ST)	[GPa]
Galvanized steel strand	(EGS)	[GPa]

D.1.3 Output files

- SUMMARY

It comprises both the input and the output parameters.

- POINT_COORDINATES

It comprises the calculated static cable profile that serves to define the element node coordinates in ADINA.

- ELEMENT_NODES

It comprises the cable element numbers to define the element nodes in ADINA.

- ELEMENT_DATA

It comprises the required parameters of the cable (truss) element to ADINA.

D.1.4 Program codes

```
PROGRAM CATENARY_SAME_ELEVATION_LEVEL
USE NUMERICAL_LIBRARIES

! This program computes the profile of an axially rigid suspended cable under its self-weight
! where the end of the supports are at the same level, i.e. the difference of
! elevation between end supports is zero. It uses the catenary equations adapted from
! Irvine HM. Cable Structures, Cambridge, MA, USA: MIT Press, 1981.

! Declaration
PARAMETER NUM=2000
INTEGER I,DIV,NOD,TAB,N1,N2,CO
INTEGER TABLE(NUM,NUM),MAT(NUM)
REAL L,SR,G,A1,A,D,D1,D2,M,TS1,TS,EIM,K,H1,DX,W,H,IM,E,I1,I2,EA,ES,ST,STR,DE
REAL X(NUM),Y(NUM),Z(NUM),X1(NUM),Y1(NUM),Z1(NUM),SA(NUM),GW(NUM)
REAL BT(NUM),DT(NUM),IS(NUM),S(NUM),T(NUM)
CHARACTER CT

!Parameters
OPEN (UNIT=10,FILE='DATA_GEOM.TXT',STATUS='OLD')
OPEN (UNIT=20,FILE='DATA_CABLE.TXT',STATUS='OLD')
OPEN (UNIT=50,FILE='YOUNGS_MODULUS.TXT',STATUS='OLD')
```

```
!Calculated results
OPEN (UNIT=30,FILE='POINT_COORDINATES.TXT',STATUS='OLD')
OPEN (UNIT=40,FILE='ELEMENT_NODES.TXT',STATUS='OLD')
OPEN (UNIT=60,FILE='ELEMENT_DATA.TXT',STATUS='OLD')
OPEN (UNIT=100,FILE='SUMMARY.TXT',STATUS='OLD')

! Number of division (elements)
READ (10,*) DIV
! Geometrical parameters
READ (10,*) L                ! Span length
READ (10,*) SR               ! Sag-to-span ratio
READ (10,*) G                ! Acceleration of gravity
READ (10,*) CO               ! In-plane coordinate system: (1) x-z; (2) x-y; (3) y-z
! Cable parameters
PRINT '("Type the conductor type")'
READ (*,*) CT

READ (20,*) A1               ! Cross-sectional area of Aluminum strands
READ (20,*) A                ! Total conductor cross-sectional area
READ (20,*) D                ! Overall diameter
READ (20,*) N1               ! Stranding-number of Aluminium
READ (20,*) D1               ! Diameter of Aluminium Strands
READ (20,*) N2               ! Stranding-number of Steel
READ (20,*) D2               ! Diameter of Steel Strands
READ (20,*) M                ! Mass of the cable per unit length
READ (20,*) TS1              ! Rated tensile strength
READ (20,*) EIM              ! EI_min
READ (20,*) K                ! 'k' factor
READ (20,*) H1               ! Initial horizontal tension

! Young's modulus
READ (50,*) EA               ! Aluminum
READ (50,*) ES               ! Steel
READ (50,*) EAW_SO           ! Alumoweld-solid
READ (50,*) EAW_ST           ! Alumoweld-stranded
READ (50,*) EGS              ! Galvanized steel strand

! Cable material selector
E=EGS

WRITE (100,*) '----------------'
WRITE (100,*) 'CATENARY PROFILE'
WRITE (100,*) '----------------'

! Initial horizontal tension/strain
CALL INITIAL_TENSION(W,M,G,L,H,H1,SR,ST,STR,E,A)
! Cable properties
CALL CABLE_PROPERTIES(CT,D,A,A1,N1,D1,N2,D2,M,TS1,TS,K,EIM,H1,H,PI,IM,E,STR,W,DE,
EA,ES)
! Geometrical parameters of the construction
CALL CONST_GEOM(DIV,L,SR,H1,W)
```

```
! Point/node coordinates & Element nodes
CALL NODE_COORDINATES(I,NOD,DIV,TAB,TABLE,W,L,H,X,Y,Z,X1,Y1,Z1,A,STR,SA,GW,BT,
DT,IS,CO)
! Length of a portion of the cable
CALL LENGTH(I,NOD,W,L,H,X1,S)
! Tension in the cable at nodes
CALL TENSION(I,NOD,W,L,H,X1,T)


END PROGRAM CATENARY_SAME_ELEVATION_LEVEL


!-------------------------------------------------------------------------
!    *** INITIAL HORIZONTAL TENSION/STRAIN ***
!
!         It computes the initial horizontal tension from
!  the sag-to-span ratio by using the parabolic approximation
!-------------------------------------------------------------------------


SUBROUTINE INITIAL_TENSION(W,M,G,L,H,H1,SR,ST,STR,E,A)

        REAL W,M,G,L,H,H1,SR,ST,STR,E,A

        W=M*G
        ! Initial Horizontal Tension (Parabolic theory)
        IF (H1.NE.0) THEN
                H1=H1*1000              ! Unit change from kN to N
                H=H1
        ELSE
                H=(W*L)/(8*SR/100)

        ENDIF

        ST=H/A                  ! Initial stress [MPa]
        STR=ST/(E*1E3)          ! Initial strain [-]; E is the Young's modulus of selected material [GPa]

END SUBROUTINE INITIAL_TENSION


!-----------------------------------------------------------------
!          *** CABLE PROPERTIES ***
!
!    It computes the necessary cable parameters
!-----------------------------------------------------------------


SUBROUTINE CABLE_PROPERTIES(CT,D,A,A1,N1,D1,N2,D2,M,TS1,TS,K,EIM,H1,H,PI,IM,E,STR,
W,DE,EA,ES)

        PARAMETER NUM=2000
        INTEGER N1,N2
        REAL D,A,A1,D1,D2,M,TS1,TS,K,EIM,H1,H,IM,E,STR,W,DE,EA,ES
        CHARACTER CT
```

```
WRITE (100,*)
WRITE (100,*) '*** CABLE PROPERTIES ***'
WRITE (100,*)

WRITE (100,'(A50,2X,A10)') 'Cable type is: ',CT
WRITE (100,*)
WRITE (100,'(A50,2X,F9.4,2X,A2)') 'Overall diameter:',D,'mm'
WRITE (100,'(A50,2X,F9.4,2X,A4)') 'Total conductor cross-sectional area:',A,'mm^2'
WRITE (100,'(A50,2X,F9.4,2X,A4)') 'Cross-sectional area of Aluminum strands:',A1,'mm^2'
WRITE (100,'(A50,2X,I4)') 'Stranding-number of Aluminium:',N1
WRITE (100,'(A50,2X,F9.4,2X,A2)') 'Diameter of Aluminum Strands:',D1,'mm'
WRITE (100,'(A50,2X,I4)') 'Stranding-number of Steel:',N2
WRITE (100,'(A50,2X,F9.4,2X,A2)') 'Diameter of Steel Strands:',D2,'mm'
WRITE (100,'(A50,2X,F9.4,2X,A4)') 'Mass of the cable per unit length:',M,'kg/m'
WRITE (100,'(A50,2X,F9.4,2X,A3)') 'Weight of the cable per unit length:',W,'N/m'

! Density of the cable
DE=M/(A*1E-6)

WRITE (100,'(A50,2X,F9.4,2X,A6)') 'Density of the cable:',DE,'kg/m^3'
WRITE (100,*)

! Rated tensile strength (from 'k' factor)
IF (TS1.NE.0) THEN
        TS=TS1
ELSE
        TS=((D/K)**2)/M
ENDIF

IF (TS1.NE.0) THEN
        WRITE (100,'(A50,2X,F9.4,2X,A2)') 'Rated tensile strength:',TS,'kN'
ELSE
        WRITE (100,'(A50,2X,F9.4,2X,A2,2X,A20)') 'Rated tensile strength:',TS,'kN','(Calculated
        from k)'
ENDIF

WRITE (100,'(A50,2X,F9.4)') 'k factor:',K
WRITE (100,'(A50,2X,F9.4,2X,A4)') 'EI_min:',EIM,'Nm^2'
WRITE (100,*)

! Modulus of elasticity
WRITE (100,'(A50,2X,F9.4,2X,A3)') 'Young's modulus of the cable composit:',E,'GPa'
        IF (E.EQ.EA) THEN
                WRITE (100,'(A111)') '(Reference material is the aluminum, E=EA)'
        ELSE IF (E.EQ.ES) THEN
                WRITE (100,'(A107)') '(Reference material is the steel, E=ES)'
        ELSE
                WRITE (100,'(A113)') '(For reference material see the program, E=?)'
        ENDIF
```

! Displaying of the initial horizontal tension (H)
IF (H1.NE.0) **THEN**   ! If the initial horizontal tension (H1) is given in DATA_CABLE.TXT
         WRITE (100,'(A50,2X,F9.4,2X,A2)') 'Initial horizontal tension:',H/1000,'kN'
ELSE
         WRITE (100,'(A50,2X,F9.4,2X,A2,2X,A35)') 'Initial horizontal tension:',H/1000,'kN',
         '(Calculated from Parabolic Theory)'
ENDIF

WRITE (100,'(A50,2X,ES12.3)') 'Initial horizontal strain:',STR

END SUBROUTINE CABLE_PROPERTIES


```
!-----------------------------------------------------------------
!     *** NODE COORDINATES & ELEMENT NODES ***
!
!     It computes the coordinates of the element nodes
!                 and defines the elements
!-----------------------------------------------------------------
```

SUBROUTINE NODE_COORDINATES(I,NOD,DIV,TAB,TABLE,W,L,H,X,Y,Z,X1,Y1,Z1,A,STR,SA,
GW,BT,DT,IS,CO)

         PARAMETER NUM=2000
         INTEGER I,NOD,DIV,TAB,CO
         INTEGER TABLE(NUM,NUM),MAT(NUM)
         REAL W,L,H,A,STR
         REAL X(NUM),Y(NUM),Z(NUM),X1(NUM),Y1(NUM),Z1(NUM),SA(NUM),GW(NUM),
         BT(NUM),DT(NUM),IS(NUM)

         ! Point/Node coordinates
         WRITE (30,'(A6,TR3,4(A6,7X))') 'Node #','X1','X2','X3','System'

         WRITE (100,*)
         WRITE (100,*) '*** POINT/NODE COORDINATES ***'
         WRITE (100,*)
         WRITE (100,'(A6,TR3,4(A6,7X))') 'Node #','X1','X2','X3','System'

         DX=L/DIV
         NOD=DIV+1

         DO I=1,NOD

                 X1(I)=(I-1)*DX
                 Y1(I)=0
                 Z1(I)=(H/W)*(**COSH**((W/H)*(L/2))-**COSH**((W/H)*(L/2-X1(I))))

                 ! Coordinate system selector
                 IF (CO.EQ.1) **THEN**
                         X(I)=X1(I)
                         Y(I)=Y1(I)
```

```
                    Z(I)=Z1(I)
      ELSE IF (CO.EQ.2) THEN
                    X(I)=X1(I)
                    Y(I)=Z1(I)
                    Z(I)=Y1(I)
      ELSE IF (CO.EQ.3) THEN
                    X(I)=Y1(I)
                    Y(I)=X1(I)
                    Z(I)=Z1(I)
      ELSE
                    WRITE(*,*) 'ERROR IN THE COORDINATE SYSTEM.... CHECK THE
                    VALUE OF CO IN DATA_GEOM.TXT'
      ENDIF

      WRITE (30,'(I4,TR3,3(F10.3,3X))') I,X(I),Y(I),-Z(I)
      WRITE (100,'(I4,TR3,3(F10.3,3X))') I,X(I),Y(I),-Z(I)


END DO

! Element nodes (Two-node truss element)
WRITE (40,'(5(A9,3X))') 'Element #','Node 1','Node 2','Node 3','Node 4'

WRITE (100,*)
WRITE (100,*) '*** ELEMENT NODES ***'
WRITE (100,*)
WRITE (100,'(5(A9,3X))') 'Element #','Node 1','Node 2','Node 3','Node 4'

TAB=1
DO I=1,DIV
      TABLE(I,1)=TAB
      TABLE(I,2)=TAB+1
      TAB=TAB+1

      WRITE (40,"(3(I4,11X))") I,TABLE(I,1),TABLE(I,2)
      WRITE (100,"(3(I4,11X))") I,TABLE(I,1),TABLE(I,2)


END DO

! Element Data
WRITE (60,'(7(A15,3X))') 'Truss Element #','Material','Section Area','Gaph Width','Birth Time',
'Death Time','Initial Strain'

WRITE (100,*)
WRITE (100,*) '*** ELEMENT DATA ***'
WRITE (100,*)
WRITE (100,'(7(A15,3X))') 'Truss Element #','Material','Section Area','Gaph Width','Birth Time',
'Death Time','Initial Strain'

DO I=1,DIV
      MAT(I)=1
      SA(I)=A/1E6
      GW(I)=0
```

```
            BT(I)=0
            DT(I)=0
            IS(I)=STR

            WRITE (60,'(8X,2(I4,13X),ES10.3,8X,3(F9.1,8X),ES10.3)') I,MAT(I),SA(I),GW(I),
            BT(I),DT(I),IS(I)
            WRITE (100,'(8X,2(I4,13X),ES10.3,8X,3(F9.1,8X),ES10.3)') I,MAT(I),SA(I),GW(I),
            BT(I),DT(I),IS(I)

        END DO

    END SUBROUTINE NODE_COORDINATES


    !--------------------------------------------------------------------
    !     *** LENGTH OF A PORTION OF THE CABLE ***
    !
    !        It computes the length of a portion of the cable
    !--------------------------------------------------------------------

    SUBROUTINE LENGTH(I,NOD,W,L,H,X1,S)

            PARAMETER NUM=2000
            INTEGER I,NOD
            REAL W,L,H
            REAL X1(NUM),S(NUM)

            WRITE (100,*)
            WRITE (100,*) '*** LENGTH OF A PORTION OF THE CABLE ***'
            WRITE (100,*)
            WRITE (100,'(A6,TR3,2(A7,7X))') 'Node #','SPAN','CABLE L'


            DO I=1,NOD

                S(I)=(H/W)*(SINH((W/H)*(L/2))-SINH((W/H)*(L/2-X1(I))))

                WRITE (100,'(I4,TR3,3(F10.3,3X))') I,X1(I),S(I)

            END DO

    END SUBROUTINE LENGTH


    !------------------------------------------------------------------
    !     *** GEOMETRY OF CONSTRUCTION ***
    !
    !        It displays the geometrical parameters of
    !                the construction
    !------------------------------------------------------------------

    SUBROUTINE CONST_GEOM(DIV,L,SR,H1,W)
```

```fortran
      INTEGER DIV
      REAL L,SR,H1,W

      WRITE (100,*)
      WRITE (100,*) '*** GEOMETRICAL PARAMETERS OF THE CONSTRUCTION ***'
      WRITE (100,*)

      WRITE (100,'(A50,2X,I4)') 'Number of element:',DIV
      WRITE (100,'(A50,2X,F9.4,2X,A1)') 'Span length:',L,'m'

      IF (H1.NE.0) THEN        ! If the initial horizontal tension (H1) is given in DATA_CABLE.TXT
            SR=((W*L)/(8*H1))*100
      ENDIF

      WRITE (100,'(A50,2X,F9.4,2X,A1)') 'Sag-to-span ratio:',SR,'%'

END SUBROUTINE CONST_GEOM



!----------------------------------------------------------
!                *** TENSION ***
!
! It computes the tension at the nodes in the cable
!----------------------------------------------------------

SUBROUTINE TENSION(I,NOD,W,L,H,X1,T)

      PARAMETER NUM=2000
      INTEGER I,NOD
      REAL W,L,H
      REAL X1(NUM),T(NUM)

      WRITE (100,*)
      WRITE (100,*) '*** TENSION IN THE CABLE AT NODES ***'
      WRITE (100,*)
      WRITE (100,'(A6,TR3,A12)') 'Node #','TENSION (kN)'

      DO I=1,NOD

            T(I)=H*COSH((W/H)*(L/2-X1(I)))

            WRITE (100,'(I4,TR3,F10.3)') I,T(I)/1000

      END DO

END SUBROUTINE TENSION
```

D.2 Natural frequencies of suspended cables

D.2.1 Introduction

In this section, program codes written in FORTRAN to calculate the natural frequencies of a level single-span suspended cable are introduced. The program applies the analytical expressions for the natural frequencies of suspended cables adapted from [31] and presented in Appendix A. It also reads the input parameters from pre-defined text files (input files) and writes the calculated results into text files (output files). Parameters of the line section are defined in the input files.

D.2.2 Input files

- DATA_GEOM

Span length	(L)	[m]
Sag-to-span ratio	(SR)	[%]
Acceleration of gravity	(G)	$[m/s^2]$

- DATA_CABLE

Number of frequencies/mode shapes	(N)	[-]
Mass of the cable per unit length	(M)	[kg/m]
Initial horizontal tension	(H1)	[kN] ... if unknown set to zero
Total conductor cross-sectional area	(A)	$[mm^2]$
Young's modulus of the cable	(EM)	[GPa]

D.2.3 Output files

- SUMMARY

It comprises both the input and the output parameters.

- OUT_OF_PLANE_FREQUENCY

It comprises the calculated natural frequencies of the out-of-plane modes.

- IN_PLANE_ASYMMETRIC_FREQUENCY

It comprises the calculated natural frequencies of the in-plane asymmetric modes.

- IN_PLANE_SYMMETRIC_FREQUENCY

It comprises the calculated natural frequencies of the in-plane symmetric modes.

- NONDIMENSIONAL_OM

It comprises the calculated dimensionless natural frequencies of symmetric modes.

D.2.4 Program codes

```
PROGRAM FREQUENCY_IRVINE_CABLE
USE NUMERICAL_LIBRARIES

! This program computes the natural frequencies of the free vibration of catenary cables.
! Irvine HM. Cable Structures, Cambridge, MA, USA: MIT Press, 1981: 90-99.

! Declaration
PARAMETER NUM=1000,PI=3.141592654
INTEGER I,J,N
REAL W,M,G,L,H,H1,SR,LA2,EM,A,LE,ERROR
REAL OM(NUM),OMB(NUM),OMB0(NUM),OMBF(NUM),OMBM(NUM),OMB1(NUM),
ER0(NUM),ERL(NUM),ERM(NUM)

! Parameters
OPEN (UNIT=10,FILE='DATA_CABLE.TXT',STATUS='OLD')
OPEN (UNIT=20,FILE='DATA_GEOM.TXT',STATUS='OLD')

! Calculated results
OPEN (UNIT=30,FILE='OUT_OF_PLANE_FREQUENCY.TXT',STATUS='OLD')
OPEN (UNIT=40,FILE='IN_PLANE_ASYMMETRIC_FREQUENCY.TXT',STATUS='OLD')
OPEN (UNIT=50,FILE='IN_PLANE_SYMMETRIC_FREQUENCY.TXT',STATUS='OLD')
```

```
OPEN (UNIT=60,FILE='NONDIMENSIONAL_OM.TXT',STATUS='OLD')
OPEN (UNIT=100,FILE='SUMMARY.TXT',STATUS='OLD')

! Frequency analysis input
READ (10,*) N                              ! Number of frequencies/mode shapes
! Conductor parameters
READ (10,*) M                              ! Mass of the cable per unit length
READ (10,*) H1                             ! Initial horizontal tension
READ (10,*) A                              ! Total conductor cross-sectional area
READ (10,*) EM                             ! Young's modulus of the cable
! Geometrical parameters
READ (20,*) L                              ! Span length
READ (20,*) SR                             ! Sag-to-span ratio
READ (20,*) G                              ! Acceleration of gravity

W=M*G                                      ! Weight of the cable per unit length
EM=EM*1E9
A=A*1E-6

! Initial horizontal tension (H)
CALL INITIAL_TENSION(W,M,G,L,H,H1,SR)

LE=L*(1+(1/8)*(W*L/H)**2)
LA2=(W*L/H)**2*(L/(H*LE/(EM*A)))

WRITE (60,'(A16,2X,F9.4)') 'Lambda square = ',LA2
WRITE (60, *)
WRITE (100,*) '----------------------------------------------------'
WRITE (100,*) 'Frequency analysis of catenary cable free vibration'
WRITE (100,*) '----------------------------------------------------'
WRITE (100,*)
WRITE (100,*) '*** CABLE PROPERTIES ***'
WRITE (100,*)
WRITE (100,'(A50,2X,F9.4,2X,A4)') 'Total conductor cross-sectional area:',A*1E6,'mm^2'
WRITE (100,'(A50,2X,F9.4,2X,A4)') 'Mass of the cable per unit length:',M,'kg/m'
WRITE (100,'(A50,2X,F9.4,2X,A3)') 'Weight of the cable per unit length:',W,'N/m'
WRITE (100,'(A50,2X,F9.4,2X,A3)') 'Elastic modulus of the cable:',EM*1E-9,'GPa'
WRITE (100,*)
WRITE (100,*) '*** GEOMETRICAL PARAMETERS OF THE CONSTRUCTION ***'
WRITE (100,*)
WRITE (100,'(A50,2X,F9.4,2X,A1)') 'Span length:',L,'m'

        IF (H1.NE.0) THEN      ! If the initial horizontal tension (H1) is given in DATA_CABLE.TXT
            SR=((W*L)/(8*H1))*100
                WRITE (100,'(A50,2X,F9.4,2X,A2,2X,A35)') 'Initial horizontal tension:',H/1000,'kN',
                '(Calculated from Parabolic Theory)'
        ELSE
                WRITE (100,'(A50,2X,F9.4,2X,A2)') 'Initial horizontal tension:',H/1000,'kN'
        ENDIF

WRITE (100,'(A50,2X,F9.4,2X,A1)') 'Sag-to-span ratio:',SR,'%'
WRITE (100,*)
```

```
CALL FREQUENCY(I,J,N,L,H,M,LA2,EM,OM,OMB,OMB0,OMBF,OMBM,OMB1,ER0,ERL,ERM,
ERROR)

END PROGRAM FREQUENCY_IRVINE_CABLE


!----------------------------------------------------------------------
!       *** INITIAL HORIZONTAL TENSION ***
!
!       It computes the initial horizontal tension from
! the sag-to-span ratio by using the parabolic approximation
!----------------------------------------------------------------------

SUBROUTINE INITIAL_TENSION(W,M,G,L,H,H1,SR)

        REAL W,M,G,L,H,H1,SR

        ! Initial horizontal tension (Parabolic theory)
        IF (H1.NE.0) THEN      ! If the initial horizontal tension (H1) is given in DATA_CABLE.TXT
                H1=H1*1000     ! Unit change from kN to N
                H=H1
        ELSE
                H=(W*L)/(8*SR/100)
        ENDIF

END SUBROUTINE INITIAL_TENSION


!-----------------------------------------------------------
!       *** NATURAL FREQUENCY ***
!
! It computes the natural frequency of cable free
!          vibration using Irvine's theory
!-----------------------------------------------------------

SUBROUTINE FREQUENCY(I,J,N,L,H,M,LA2,EM,OM,OMB,OMB0,OMBF,OMBM,OMB1,ER0,ERL,
ERM,ERROR)

        PARAMETER NUM=1000,PI=3.141592654
        INTEGER I,J,N
        REAL L,H,M,LA2,EM,ERROR
        REAL OM(NUM),OMB(NUM),OMB0(NUM),OMBF(NUM),OMBM(NUM),OMB1(NUM),
        ER0(NUM),ERL(NUM),ERM(NUM)

        ! Out-of-plane
        WRITE (100,*) 'Natural frequencies of the OUT-OF-PLANE motion'
        WRITE (30,'(A4,2X,A30)') 'Mode','Out-of-plane'
        WRITE (100,*)

        DO J=1,N
                OM(J)=(J*PI/L)*SQRT(H/M)
```

```fortran
          WRITE (100,'(A10,2X,I3,10X,F9.4,2X,A5)') 'Mode',J,OM(J),'rad/s'
          WRITE (30,'(I3,15X,F9.4)') J,OM(J)
END DO

! In-plane / asymmetric
WRITE (100,*)
WRITE (100,*) 'Natural frequencies of the ASYMMETRIC IN-PLANE motion'
WRITE (40,'(A4,2X,A30)') 'Mode','Asymmetric in-plane'
WRITE (100,*)

DO J=1,N
          OM(J)=(2*J*PI/L)*SQRT(H/M)
          WRITE (100,'(A10,2X,I3,10X,F9.4,2X,A5)') 'Mode',J,OM(J),'rad/s'
          WRITE (40,'(I3,15X,F9.4)') J,OM(J)
END DO

! In-plane / symmetric
WRITE (100,*)
WRITE (100,*) 'Natural frequencies of the SYMMETRIC IN-PLANE motion'
WRITE (50,'(A4,2X,A30)') 'Mode','Symmetric in-plane'
WRITE (60,'(40X,A4,2X,A35)') 'Mode','Nondimensional Frequency/Pi'
WRITE (100,*)

DO J=1,N
          ! Halving intervals
          ERROR=0.0001                              ! Accuracy in halving intervals
          OMB0(J)=PI/2+(J-1)*PI
          OMBF(J)=2.9999*PI/2+(J-1)*PI
          OMBM(J)=(OMB0(J)+OMBF(J))/2
          ER0(J)=TAN(OMB0(J))-(OMB0(J)-(4/LA2)*OMB0(J)**3)
          ERL(J)=TAN(OMBF(J))-(OMBF(J)-(4/LA2)*OMBF(J)**3)

          IF (ABS(ER0(J)).LT.ERROR) THEN
                  OMBM(J)=OMB0(J)
          ENDIF

          IF (ABS(ERL(J)).LT.ERROR) THEN
                  OMBM(J)=OMBF(J)
          ENDIF

          DO I=1,1000
                  ER0(J)=TAN(OMB0(J))-(OMB0(J)-(4/LA2)*OMB0(J)**3)
                  ERL(J)=TAN(OMBF(J))-(OMBF(J)-(4/LA2)*OMBF(J)**3)
                  ERM(J)=TAN(OMBM(J))-(OMBM(J)-(4/LA2)*OMBM(J)**3)
                  IF (ABS(ERM(J)).LT.ERROR) OMB1(J)=OMBM(J)
                  IF ((ERM(J).LT.0).AND.(ER0(J).LT.0)) OMB0(J)=OMBM(J)
                  IF ((ERM(J).GT.0).AND.(ERL(J).GT.0)) OMBF(J)=OMBM(J)

                  OMBM(J)=(OMB0(J)+OMBF(J))/2
          END DO

          OMB(J)=OMB1(J)*2
```

```fortran
      WRITE (60,'(40X,I3,15X,F9.4)') J,OMB(J)/PI
      OM(J)=OMB(J)*SQRT(H/M)/L

      WRITE (100,'(A10,2X,I3,10X,F9.4,2X,A5)') 'Mode',J,OM(J),'rad/s'
      WRITE (50,'(I3,15X,F9.4)') J,OM(J)
      END DO

      END SUBROUTINE FREQUENCY
```

Université du Québec à Chicoutimi

Appendix E

Reduced-scale conductor model assembly

CIGELE-MDI-101

No.	Qty.	Description	Model	Comments
15	1	Interfaces	N2 3M11	B
	1	Mounting stud	2A	Aluminum
13	2	Sleeve		ke
	2	Upper arm (female)		
		Ball bearing	4RS	N I
9		Support arm (male)		
8		Load cell	LC 50	UTEK
7	2	Rigid frame		
6		Scale	RR-W-4 0D	
5		Air cylinder	A	P ke
4	1	Lifting stage		
3		Jack		
2	1	Rigid base		

A
9.0 (9)

B
1

C

-DO
S

1

2

3

4

3/8   2   1   3/8   1/8

3

1/4

Closed in operation

Opened in operation

2

3/8   1/2   1/8   1/8

1

CYL

9

1/4

EXH   IN

8   1/8

7   1/2   6   5

INLET

3/8   3/8

No.	Qty.	Description	Model
9.	1	Inline poppet valve	N3554904553
8.	1	Ball control valve	1/2 INCH
7.	1	Filter-regulator unit	07E36B13AC
6.	1	Air tank	HT-95118 (24L)
5.	1	Gauge	
4.	1	Air control valve	B511ACB53C
3.	3	Ball control valve	1/4 INCH
2.	1	Quick exhaust valve	0R37B
1.	1	Air cylinder	2.0CH2AU4FS34AC12.0

Université du Québec à Chicoutimi

Appendix F

Shock load generator schematic

Tamás Kálmán	SIZE	FSCM NO.	DWG NO. CIGELE-MDI-201	REV
Mars 2007	SCALE		SHEET 1 OF 1	

Instrumentation schematic — Appendix G

LCF450 (LV) CSG110 (LV) CSG110 (RV) LCF450 (RV)
LCF450 (LH) CSG110 (LH) CSG110 (RH) LCF450 (RH)

10VDC   RF   V+   V−   SHIELD
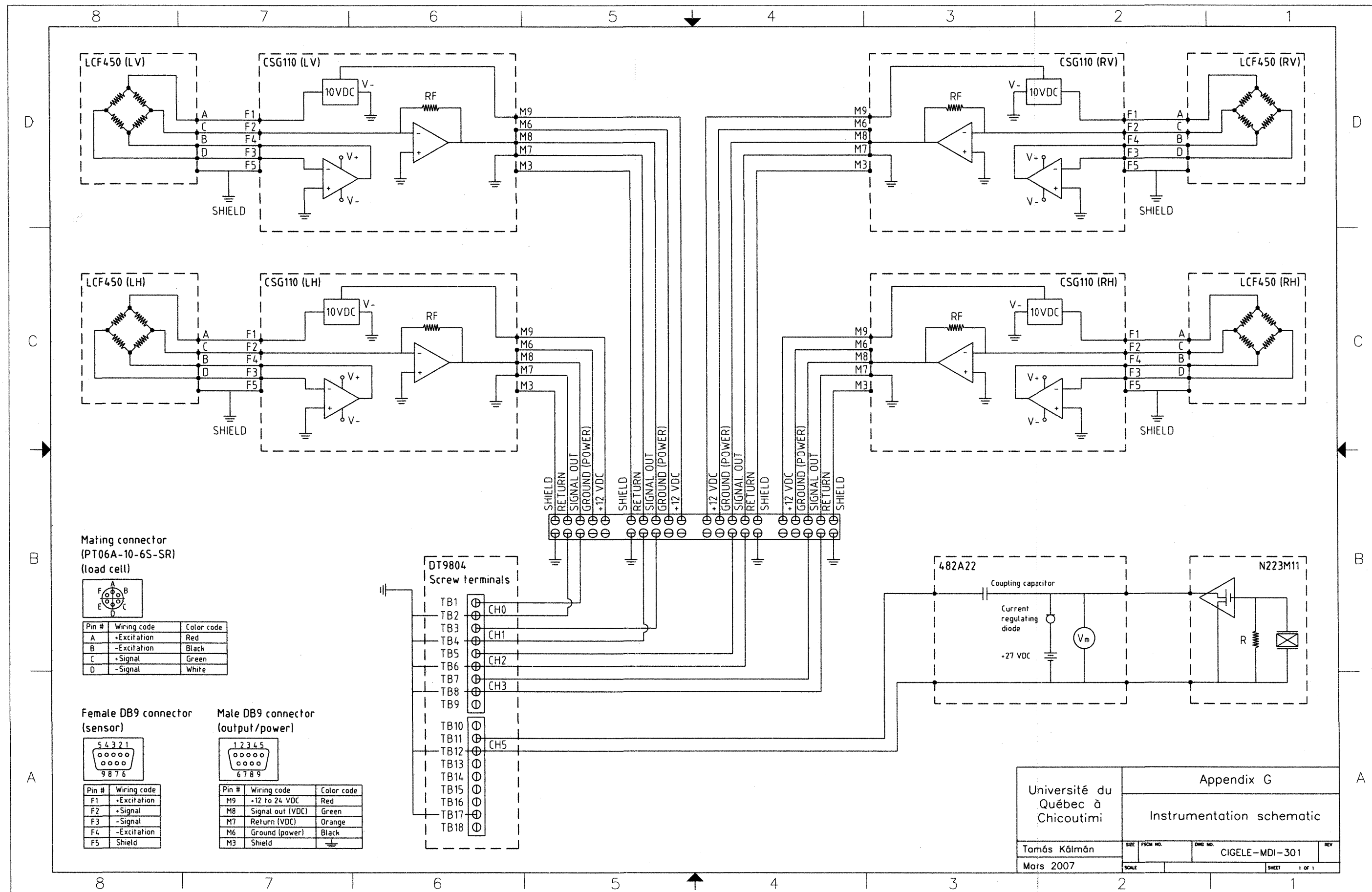
Mating connector
(PT06A-10-6S-SR)
(load cell)

Pin #	Wiring code	Color code
A	+Excitation	Red
B	−Excitation	Black
C	+Signal	Green
D	−Signal	White

Female DB9 connector
(sensor)

Pin #	Wiring code
F1	+Excitation
F2	+Signal
F3	−Signal
F4	−Excitation
F5	Shield

Male DB9 connector
(output/power)

Pin #	Wiring code	Color code
M9	+12 to 24 VDC	Red
M8	Signal out (VDC)	Green
M7	Return (VDC)	Orange
M6	Ground (power)	Black
M3	Shield	

DT9804
Screw terminals
TB1 CH0
TB2
TB3 CH1
TB4
TB5 CH2
TB6
TB7 CH3
TB8
TB9
TB10
TB11 CH5
TB12
TB13
TB14
TB15
TB16
TB17
TB18

SHIELD / RETURN / SIGNAL OUT / GROUND (POWER) / +12 VDC

482A22   Coupling capacitor   Current regulating diode   +27 VDC   Vm

N223M11   R

Université du
Québec à
Chicoutimi

Appendix G

Instrumentation schematic

Tamás Kálmán
Mars 2007

DWG NO. CIGELE-MDI-301
SHEET 1 OF 1